Development of a controlled Vacuum Ultraviolet Light Source for the Characterization and Testing of Silicon Photomultipliers for nEXO

Tsvetelin Totev

Department of Physics

McGill University, Montreal

A thesis submitted to McGill University in partial fulfillment of the requirements of the degree of

Master of Physics

Abstract

The nEXO experiment is a 5 tonne enriched liquid xenon time projection chamber that aims to detect the yet to be observed neutrinoless double beta decay ($0\nu\beta\beta$) in order to confirm the Majorana nature of neutrinos. The observation of this decay would be proof of physics beyond the Standard Model as it would violate lepton number conservation and could also provide insight into the observed matter-antimatter asymmetry in our universe. nEXO will be using silicon photomultipliers (SiPM) to detect the xenon scintillation signal resulting from decays in its volume. As part of the effort for SiPM testing and characterization this thesis elaborates on the development and first results of a controlled 172 nm electroluminescent (EL) xenon-gas light source whose aim is to produce pulses as intense and as short as possible to test and characterize SiPMs. Two anode geometries are investigated: a gold-plated copper anode and a thin stainless steel anode. Production of EL pulses has been achieved using the gold-plated anode at 1450 Torr for biases between 2-4 kV. The light signal is measured using a PMT and the maximum amplitude is 0.88$\pm$0.06 mV with a minimum pulse width of 0.51$\pm$0.01 μs at 4 kV. For the steel needle the evolution of the pulse height was measured, fitted and plotted as a function of bias and gas pressure and the maximum amplitude was found to occur at 600 Torr and 2.3 kV anode bias.

Abrégé

Le détecteur nEXO est une chambre de projection temporelle contenant 5 tonnes de xénon liquide enrichi visant à observer pour la première fois la double désintégration bêta sans émission de neutrinos ($0\nu\beta\beta$) pour confirmer la nature Majorana des neutrinos. L'observation de cette désintégration représente un exemple de physique hors du Modèle Standard de la Physique des Particules et peut aussi aider a résoudre le mystère concernant l'asymétrie matière-antimatière dans nôtre univers. nEXO utilisera des photomultiplicateurs au silicium (SiPM) pour détecter la scintillation du xénon lors des désintégrations dans son volume. En tant que partie de l'effort pour les essais et la caractérisation de SiPM cette thèse présente les récents développements et les premiers résultats d'une source lumineuse électroluminescente contrôlée qui utilise du xénon gazeux. Cette source a pour but de produire des photons de longueur d'onde $\lambda = 172$ nm en impulsions aussi intenses et courtes que possible afin de tester et caractériser des SiPM. Pour cela, deux géométries d'anodes sont investiguées : une anode en cuivre plaquée or ainsi qu'une mince aiguille d'acier inoxydable. Des impulsions électroluminescentes ont été produites avec l'anode plaquée or avec le xénon gazeux à une pression de 1450 Torr pour de tensions sur l'anode entre 2-4 kV. Le signal lumineux est mesuré avec un tube photomultiplicateur et l'amplitude maximale de 0.88±0.06 mV ainsi que la durée d'impulsion minimum de 0.51±0.01 μs sont réalisées à 4 kV. Les données prises avec l'aiguille d'acier ont pour but de suivre l'évolution de l'amplitude en fonction de la pression gazeuse et de la tension à l'anode. Pour chaque pression et tension, des ajustements de courbes ont été faits et les résultats indiquent que l'amplitude maximale est atteinte à un pression de 600 Torr et une tension de 2.3 kV.

Contribution of Authors

All chapters in this thesis have been written by the author. Additionally, all data presented in Chapter 4 was recorded by me. The code to analyze the data was written in Python by me (with the exception of the charge data fitting function, written by Thanh Nguyen).

The assembly of the gas handling system, ELS chamber and the machining of the gold-plated anode presented in Chapters 2 and 3 were performed by Thanh Nguyen, Soud Kharusi, and Thomas Brunner; the initial designs for the chamber and gas handling system were done by Omar Chammaa and Christopher Morison. The light-tight box and the stainless steel anode were made by the author, who also modified the xenon gas handling system to ensure compatibility with the light-tight box.

Thomas McElroy, Sebastian Eppelt, and Haojie Ni developed the GUI, data acquisition and analysis code in C++ for the digitizer discussed in Chapter 3. The author modified a copy of the analysis code to adapt it to the needs of the ELS and make the data it produces Python-friendly.

Thanh Nguyen wrote the original code to interface with the pressure gauges and the oscilloscope, described in Chapter 3, as well as to fit the charge data. The interfacing code was improved by the author through the addition of functionalities developed by Jack Sankey. The charge fitting routines were also rewritten by me.

Acknowledgements

I first and foremost wish to thank Dr. Thomas Brunner for supervising my Master's degree, giving me the opportunity to work on this project and teaching me so many things. Without his continued guidance during my degree, help both in the lab with hardware and electronics and out of the lab with theoretical insights, and remarkable patience this work would not have been possible.

I also am very grateful to Dr. Thomas McElroy and Dr. Christopher Chambers. The former, for always sharing his deep knowledge and insight on light and scintillation related physics as well as for his guidance when it came to data analysis and the latter for teaching me a lot about optics and focusing techniques.

I cannot forget to mention all the past undergraduate students who have worked on this project in the past years and would especially like to thank Soud Kharusi for his help on bringing me up to speed with the project when I started working on it.

Finally, to my parents, infinite gratitude for all the support.

Table of Contents

List of Figures

List of Tables

1 Introduction

1.1 Majorana Neutrinos and Neutrinoless Double Beta Decay

Neutrinos are the most abundant known massive particles in the universe, and despite being discovered more than 60 years ago by Reines and Cowan [1], they continue to puzzle physicists until today. Neutrinos are the only neutral and massless fermions in the Standard Model of Particle Physics (SM) [2]. However, the observation of neutrinos oscillating between different favor eigen-states as they travel requires that they have mass which poses an issue to the SM [3–5]. Attributing only a Dirac mass to neutrinos under the assumption that they acquire their mass through the Higgs coupling, as is the case for all other fermions, leads to a few issues for which no solutions are currently present. Namely requiring the existence of yet-unobserved and non-interacting right-handed neutrinos according to the Lagrangian describing the neutrino mass, as well as failing to provide an explanation for the sub-eV neutrino mass scale [6, 7]. One solution to the theoretical issues arising from massive neutrinos is to introduce them as Majorana fermions. This not only eliminates the need for observable right-handed neutrinos but also allows the formulation of the so-called seesaw mechanism, capable of explaining the low neutrino mass scales [8–10]. The possibility that neutrinos are Majorana particles has several very interesting implications that will be discussed below, beyond them being the first fermions to have non-distinct particle anti-particle pairs.

One of the important implications of Majorana neutrinos is that they open a new decay channel, so-called neutrinoless double beta decay ($0\nu\beta\beta$), for isotopes that typically decay through 2 neutrino double beta decay ($2\nu\beta\beta$). First proposed by Maria Goeppert-Mayer in 1935, $2\nu\beta\beta$ is a mechanism through which isotopes with even numbers of protons and neutrons can decay to a lower energy state daughter [11]. This is shown in Figure 1 for ^{136}Xe where a single beta decay would result in a ^{136}Cs daughter at higher energy and is therefore energetically forbidden. Despite there being a few dozen nuclides that could

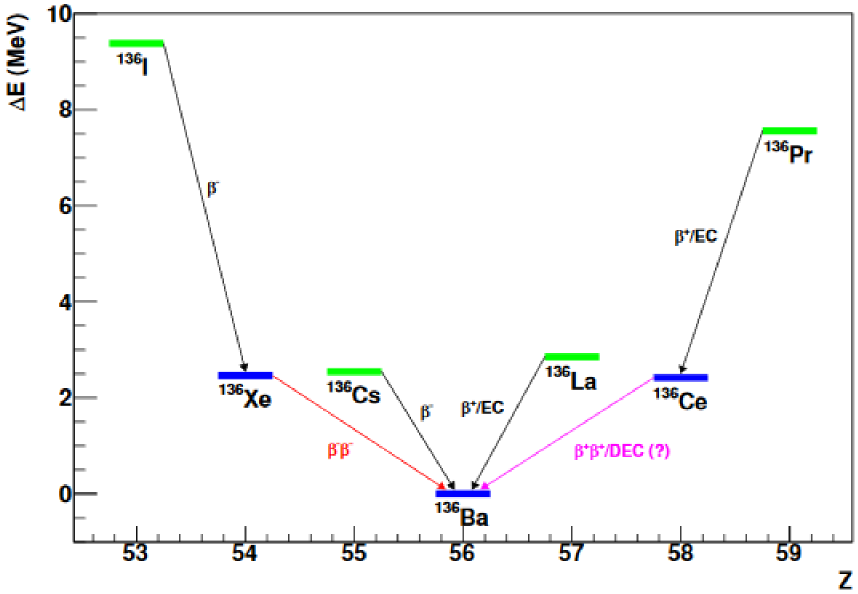

Figure 1: Energy Levels of A=136 isobars. Given ^{136}Xe cannot reach a lower energy state through a single beta decay, it must undergo double beta decay to ^{136}Ba. ^{136}Ce can theoretically decay to the same daughter isotop through double electron capture or double β^+ decay but this has not yet been experimentally observed. Figure from [12].

theoretically undergo $2\nu\beta\beta$ only 14 have been experimentally observed (see [13–16]) and the shortest half lives of the double beta decays in these isotopes are on the order of 10^{18} years [6], much larger than the age of the universe ($\sim 1.4 \times 10^{10}$ years). If neutrinos were Dirac particles, $2\nu\beta\beta$ would be the only possible decay mode, with no exciting physics associated. However, Majorana neutrinos turn these events into prime territory to search for entirely new physics beyond the Standard Model. If neutrinos are their own anti-particles, neutrinoless double beta decays ($0\nu\beta\beta$) is a possible decay mode, as illustrated in Figure 2. However, no $0\nu\beta\beta$ decay has been observed to date in any isotope and the lower limits on their half lives are on the order of 10^{26} years [17, 18]. A number of experiments across the world are trying to detect $0\nu\beta\beta$ decays in various isotopes, and the strategies employed by most of them generally have one thing in common: the use of

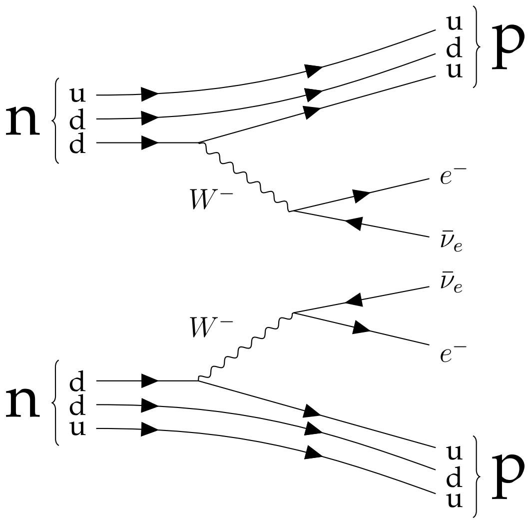

Figure 2: On the left: Feynman diagram of a regular double beta decay in which two neutrons decay into two protons and release 2 $e^-\bar{\nu}_e$ pairs. On the right: A neutrinoless double beta decay where only 2 e^- are present in the final state.

a large mass of active isotope that can undergo $2\nu\beta\beta$ and maximize the exposure of the experiment. If $0\nu\beta\beta$ exists, the number of detected $0\nu\beta\beta$ events scales with

$$N_{0\nu\beta\beta} = \ln(2) \times \frac{\alpha \times m \times N_A}{M} \times \epsilon_{det} \times \frac{t_{live}}{T_{1/2}}, \tag{1}$$

which gives the expected number of $0\nu\beta\beta$ decays that will be observed by a detector using mass m of material with isotopic abundance fraction α. M and N_A are the molar mass of the decaying isotope and Avogadro's number, respectively, ϵ_{det} is the detector's efficiency to observe $0\nu\beta\beta$ decays and $t_{live}/T_{1/2}$ is the ratio between the detector "live-time" (the time during which data has been taken) and the neutrinoless double beta decay's half-life as shown in equation 2. It is clear that increasing the active mass of the relevant isotope increases the possibility to observe the desired event. Additionally, by measuring (or placing limits) on the $0\nu\beta\beta$ decay half-life, it is possible to determine (or place limits on) the neutrino's effective Majorana mass which is proportional to the decay rate:

$$\Gamma^{0\nu} = \frac{1}{T_{1/2}} = G^{0\nu} \times |g_A^2 \times M_{GT}^{0\nu} - g_V^2 \times M_F^{0\nu} + g_A^2 \times M_A^{0\nu}|^2 \times \frac{\langle m_{\beta\beta}\rangle^2}{m_e^2}. \tag{2}$$

Where $M^{0\nu}_{GT}, M^{0\nu}_{F}$ and $M^{0\nu}_{A}$ terms represent the Gamow-Teller, Fermi and tensor nuclear matrix elements, calculated with methods overviewed e.g. in [19]. g_A and g_V are the axial and vector coupling constants for the weak interaction and $G^{0\nu}$ is a leptonic phase space factor which varies between isotopes [20]. It is important to note that equation 2 is only valid in the context of the light Majorana neutrino exchange model used to describe $0\nu\beta\beta$. However, if a different mechanism is responsible for $0\nu\beta\beta$, it is possible that $\langle m_{\beta\beta}\rangle$ can never be determined despite an observation of the decay; refer to [21] for more details.

The results from neutrino oscillation measurements give information about the differences of the squared masses, but do not allow conclusions about the absolute mass scale or mass ordering. Furthermore, only having the differences of the squared masses results in two possible mass hierarchies for the three neutrino states: the normal and inverted hierarchies. The discovery potential of next-generation experiments to observe $0\nu\beta\beta$ in the case neutrinos are Majorana particles, assuming that the light Majorana neutrino exchange model and the calculations for the nuclear matrix elements are correct, differs depending on the mass hierarchy. In the case of an inverted hierarchy, the discovery probability is 100% given the previous assumptions; the normal hierarchy discovery probablity is closer to 70% [21]. A schematic representation of the mass hierarchies is given in Figure 3a, where $|\Delta m^2_{atm}| \simeq 2.5 \times 10^{-3}$ eV^2 and $\Delta m^2_{sol} \simeq 7.6 \times 10^{-5}$ eV^2 [22]. $|\Delta m^2_{atm}|$ is the mass splitting term determined by atmospheric neutrino experiments such as IceCube and ANTARES [23,24] or the nuclear reactor antineutrino experiment Daya Bay [25]; such experiments can only measure its absolute value. On the other hand, Δm^2_{sol} is determined by solar neutrino experiments like Super Kamiokande, SNO, and the Homestake experiment [26–28]. The mass hierarchy can also be visualized in Figure 3b, along with the current limits on $\langle m_{\beta\beta}\rangle$ by the GERDA experiment [18]. Current limits placed by neutrino oscillation experiments are too high to be able to differentiate between between the inverted and normal hierarchies but future experiments will aim to reach sensitivities on the order of 20 meV or lower for the Majorana neutrino mass.

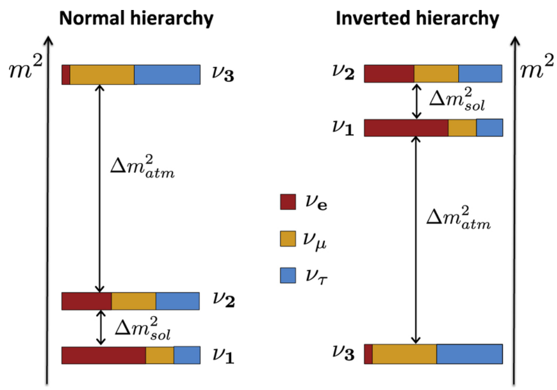

(a) Neutrino mass hierarchy scale with relative contributions from each flavour.

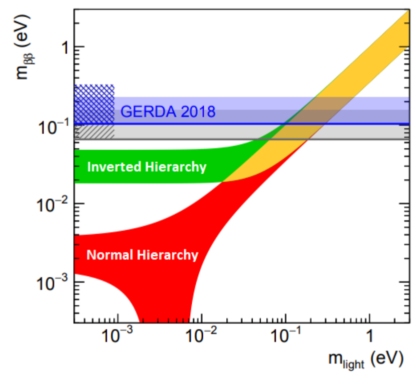

(b) Mass hierarchy regions as functions of $\langle m_{\beta\beta}\rangle$ and the lightest neutrino mass.

Figure 3: On the left: Depiction of the normal and inverted mass hierarchies with the squared mass differences separating each mass state (ν_1, ν_2, ν_3) along with the contributions of each flavor state (ν_e, ν_μ, ν_τ) to the mass states [29]. On the right: Parameter space allowed by oscillation experiments for normal and inverted mass hierarchy regions plotted for the lightest neutrino mass versus the effective Majorana neutrino mass. The straight lines represent the $\langle m_{\beta\beta}\rangle$ limits probed by GERDA [18].

Successful observation of a neutrinoless double beta decay would not only confirm the Majorana nature of the neutrino and thus hint at an entirely new process for ν mass generation not involving the Higgs but would also be the first observation of a process that directly violates lepton number conservation, a key conservation law in the Standard Model of Particle Physics. Given $0\nu\beta\beta$ decays are leptogenetic processes producing purely matter, their existence can shine light on the matter-antimatter asymmetry of the universe [30]. These are among the motivations that have spurred the development of many detectors to search for the existence of neutrinoless double beta decay in various isotopes. One of these experiments, EXO-200 [31], notable for first observing $2\nu\beta\beta$ in ^{136}Xe with a half-life of 2.11×10^{21} yr will be overviewed below along with its successor, the tonne-scale nEXO experiment e.g. [32, 33].

1.2 The EXO-200 Experiment

The EXO-200 detector is a 175 kg liquid xenon (LXe) time projection chamber (TPC) that aimed to observe neutrinoless double beta decay in ^{136}Xe. EXO-200 took data from 2011 to the end of 2018, and did not only observe 2ν double beta decay in the aforementioned isotope for the first time, but also placed one of the most competitive limits on the half-life of $0\nu\beta\beta$ in ^{136}Xe (3.5×10^{25} yr) [34]. The EXO-200 experiment was located at the Waste Isolation Pilot Plant in New Mexico, at a depth of roughly 1600 m.w.e (meters water equivalent) [35]. The EXO-200 detector, shown in Figure 4a below, consists of two TPCs with a shared cathode. The latter is held at high negative voltage of around -8 kV

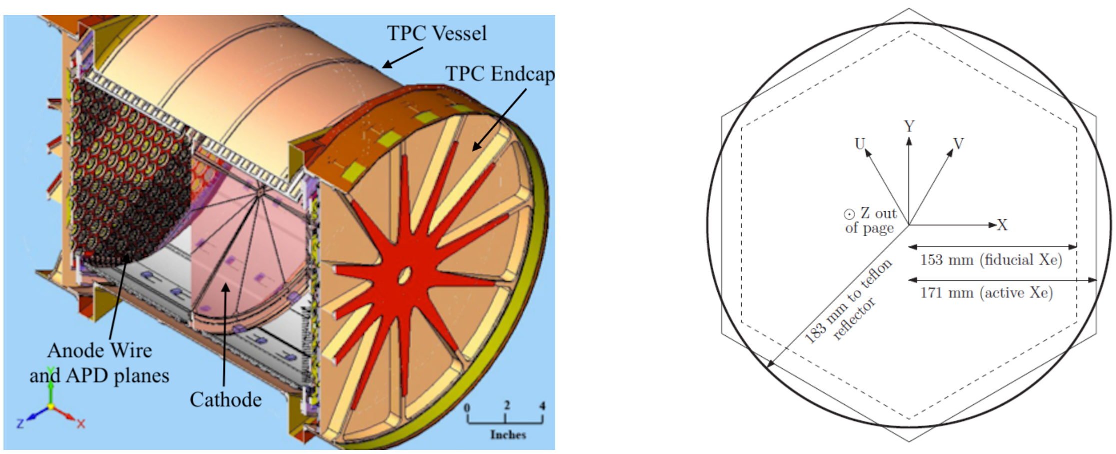

(a) EXO-200 TPC

(b) Charge collection wire schematic

Figure 4: On the left: Cross section of the EXO-200 TPC. It is made of 1.3 mm thick ultra-pure copper and located inside an outer copper cryostat filled with HFE-7000: an ultra-clean refrigerant fluid which also provides shielding. Not shown are 25 cm of lead shielding, an active muon veto system, and the assembly is located inside a class 1000 clean room [33, 36]. On the right: Arrangement of charge collecting wires in EXO-200. V wires are biased to be electron transparent and measure an induced charge signal, U wires are held at virtual ground and collect the electrons. This double wire plane configuration allows for determination of events' radial positions [37].

and creates the field that drifts the ionization electrons from interactions inside the TPC to the charge collection wires on either end of the vessel [32]. These charge collection wires, are arranged in 2 planes whose wires are termed "V" and "U" wires. The angle between U and V wires is 60°, and both wire planes have 95.8% optical transparency [36]. This geometry, depicted in Figure 4b, allows the X-Y position of events to be determined. The scintillation light emitted by the xenon during decays or background interactions is measured using Large-Area Avalanche Photodiodes (LAAPDs) located on each end cap of the TPC behind the charge collecting wires. Using the light signal as trigger, and knowing that the electron drift velocity in liquid xenon is around $1.705^{+0.014}_{-0.010}$ mm/μs at 380 V/cm fields it is possible to determine the lateral position of an event within the TPC [38]. Hence, EXO-200 can fully reconstruct the position of interactions inside the LXe volume in addition to event energy.

Unfortunately, good event reconstruction alone does not guarantee detection of a $0\nu\beta\beta$ decay even if it does occur. In a $2\nu\beta\beta$ decay, the energy is carried away by electrons and neutrinos; since neutrinos essentially do not interact, only the light and ionization charge produced by the electrons in the xenon is useable to reproduce the energy deposited. Therefore, what EXO-200 actually measures is the amount of kinetic energy carried by the electrons. In a regular $2\nu\beta\beta$ decay the electrons only carry part of the total energy, resulting in a continuous spectrum, but in $0\nu\beta\beta$, since there are no neutrinos in the final state, the electrons carry the energy corresponding to the Q value of the decay. In this case, the sign of a $0\nu\beta\beta$ decay is essentially a sharp peak at exactly the Q value of the $\beta\beta$ decay, $Q_{\beta\beta} = 2458$keV for ^{136}Xe [39]. The measurement of this signal is therefore extremely reliant on a detector with good energy resolution, see eq. 1; γ's with energies close to the $Q_{\beta\beta}$ value can mimic a $0\nu\beta\beta$ signature and the $2\nu\beta\beta$ electron kinetic energy spectrum's continuous tail needs to be separated from $0\nu\beta\beta$ signals that would be located right at the end of said tail as shown in Figure 5. The distributions for $0\nu\beta\beta$ decays signals are normalized to 10^{-2} and 10^{-6}, conceptually representing what happens to the overlap with the $2\nu\beta\beta$ tail as the number of observed $0\nu\beta\beta$ events becomes smaller. The EXO-200 collaboration was the first to demonstrate that it is possible to boost the energy

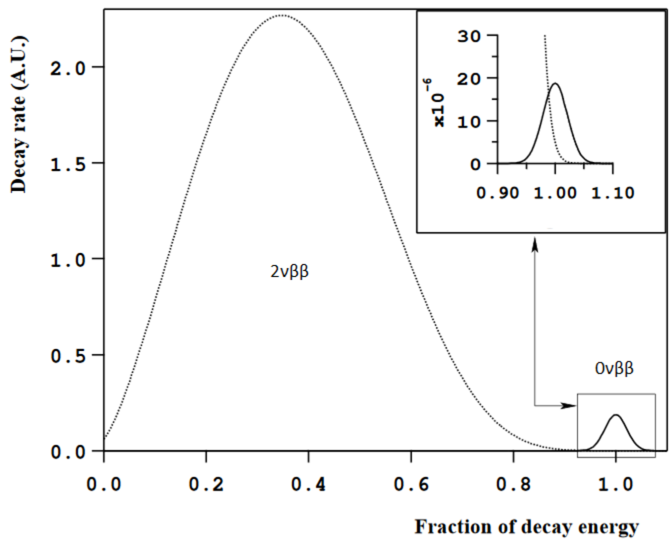

Figure 5: Summed electron kinetic energy spectrum normalized to 1 (dotted curve) for $2\nu\beta\beta$ decays. The secondary smaller peak corresponds to $0\nu\beta\beta$ decays normalized to 10^{-2}, in the inset this peak is normalized to 10^{-6}. The signal corresponding to $0\nu\beta\beta$ decays is a distribution rather than a delta function because energy collection is governed by Poisson statistics, where the number of detected photons for a $0\nu\beta\beta$ is distributed around the Q value [41].

resolution of LXe detectors by making use of the fact that energy conservation dictates an anti-correlation between the amount of light and charge produced in interactions, see [40]. By using a linear combination of the two signals, a final resolution of σ_E/E =1.15±0.02 % was achieved [34].

When trying to observe an ultra rare decay, background radiation shielding is a must, hence locations deep underground are essential to limit the impact of cosmogenic backgrounds. Additionally, the materials used to fabricate the TPC must be as radiopure as possible and backgrounds from radioactive elements in the walls must be considered in the analysis; background contributions ultimately limit a detector's sensitivity [35]. A xenon recirculation and purification system ensures the liquid retains its high purity, a necessity to avoid deterioration not only in the light signal but even more so in the charge signal. This system reduces backgrounds from other radioactive materials in the xenon and increases electron lifetime by eliminating electronegative impurities. Being a single phase xenon TPC capable of full positional event reconstruction, EXO-200 has great background rejection capabilities. It can reject β's and α's arising from the copper surfaces by restricting a fiducial volume, effectively ignoring events that are outside a specific volume. Alpha decays in the inner xenon volume away from the walls can be rejected considering the ratio of light to charge produced. Indeed, they generally produce dense charge clouds in which a lot of electron-ion recombination occurs, resulting in little charge collected and dominating scintillation light. Backgrounds due to γ's that create "multi-site" (MS) events from multiple Compton scatters can be eliminated by making use of position reconstruction. "Single-site" γ backgrounds (where all the charge is deposited in a volume 3 mm across [37]) near $Q_{\beta\beta}$ can be differentiated from $2\nu\beta\beta$ due to their tendency to deposit energy on more than one neighboring charge collection channel as well as the longer rise times of their charge signal (see [42]).

Despite not succeeding in the observation of $0\nu\beta\beta$, EXO-200 demonstrated the viability of large liquid xenon TPCs to search for rare events and made advances in different detector techniques such as energy resolution improvements and background rejection capabilities, laying the foundations for tonne-scale $0\nu\beta\beta$ LXe experiments such as EXO-200's successor nEXO, which will be described below.

1.3 The nEXO Experiment

nEXO is a future 5 tonne liquid xenon (90% enriched to ^{136}Xe) TPC aiming to observe $0\nu\beta\beta$ decay in ^{136}Xe [33]. The significant increase in the mass of xenon increases the sensitivity to $0\nu\beta\beta$. Since existence and half-life of $0\nu\beta\beta$ are unknown; the strategy for various experiments is to build detectors with incrementally larger target mass. The nEXO TPC is a single volume TPC with cathode and anode on opposite end caps, with a cylindrical LXe drift volume of 125 cm length and 115 cm in diameter [33]. Given the larger drift length of the nEXO TPC, electron lifetimes longer than 10 ms are required; this places more stringent requirements on the purity of the xenon. The anticipated location for nEXO is the SNOLAB cryopit, located at a depth of 2 km underground with 6000 m.w.e to protect from cosmogenic backgrounds. The nEXO detector concept shown in Figure 6 features the LXe TPC in the center of two cryostats, one filled with HFE-7000 refrigerant and the other held at vacuum to minimize heat transfer. This whole assembly is located in the outer detector, a 13 m by 13 m water tank instrumented with PMTs that acts not only as a γ shield but can also tag incoming muons that emit Cherenkov radiation in the water [33].

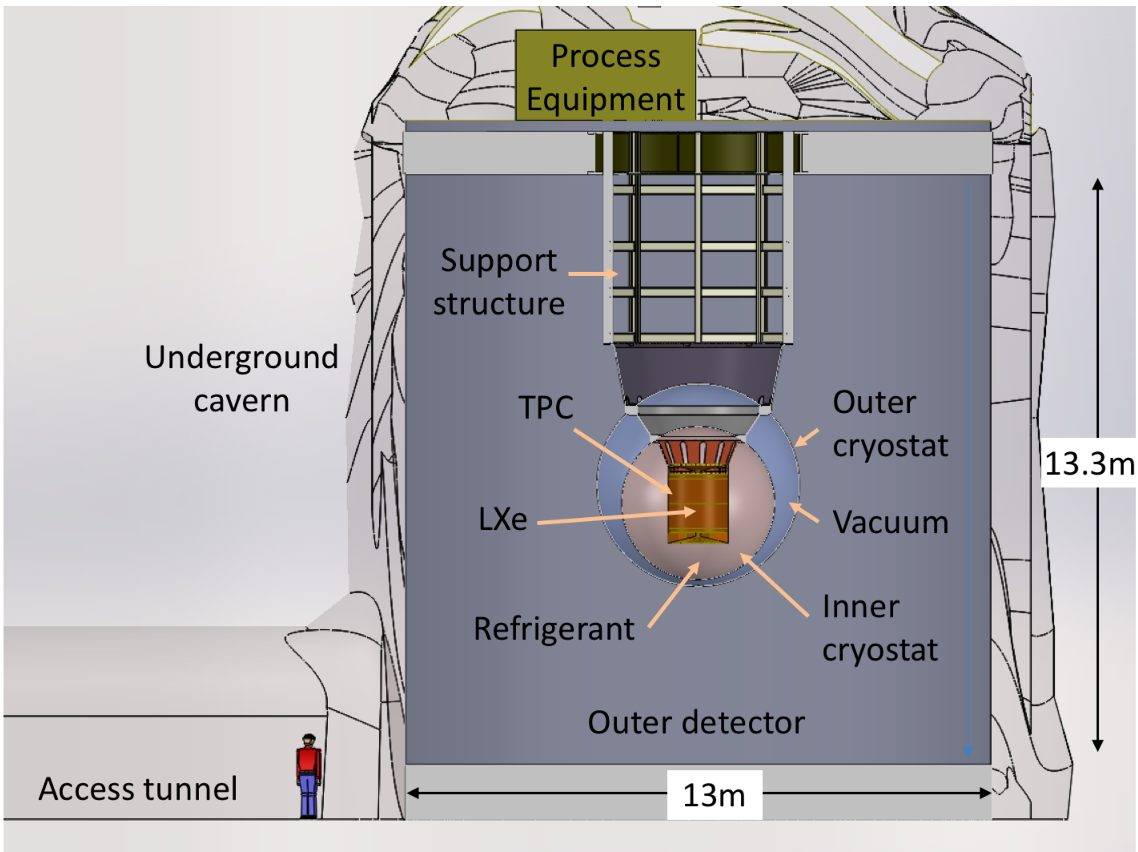

Figure 6: Conceptual design of the nEXO detector, located in an underground cavern. Shown are the LXe TPC surrounded by two layers of cryostats; the HFE-7000 filled cryostat provides the cooling power to keep the xenon liquid and double as a γ ray shield. Meanwhile the vacuum cryostat provides thermal insulation. There is an additional outer detector which consists of a large water tank used to reduce cosmogenic, γ and muon backgrounds [33].

In nEXO the ionized charge produced by events will be drifted to the top of the TPC under the influence of an electric field produced by a thin cathode located at the bottom of the vessel [33]. The current design aims for a maximum cathode bias of -50 kV, which would result in a drift field of 400 V/cm, similar to that of EXO-200 [42]. The field in the TPC is shaped by resistors attached to 58 field shaping rings (FSRs) spaced uniformly between anode and cathode. Charge collection tiles held at virtual ground made of square dielectric pads are used to collect the electrons [43]. An inside view of the field shaping rings and anode structure is presented in Figure 7. The copper FSRs are held together by sapphire rods, and the light collection is done by Silicon Photomultipliers (SiPMs) of around 1 cm^2 area each arranged in arrays called staves located behind the FSRs.

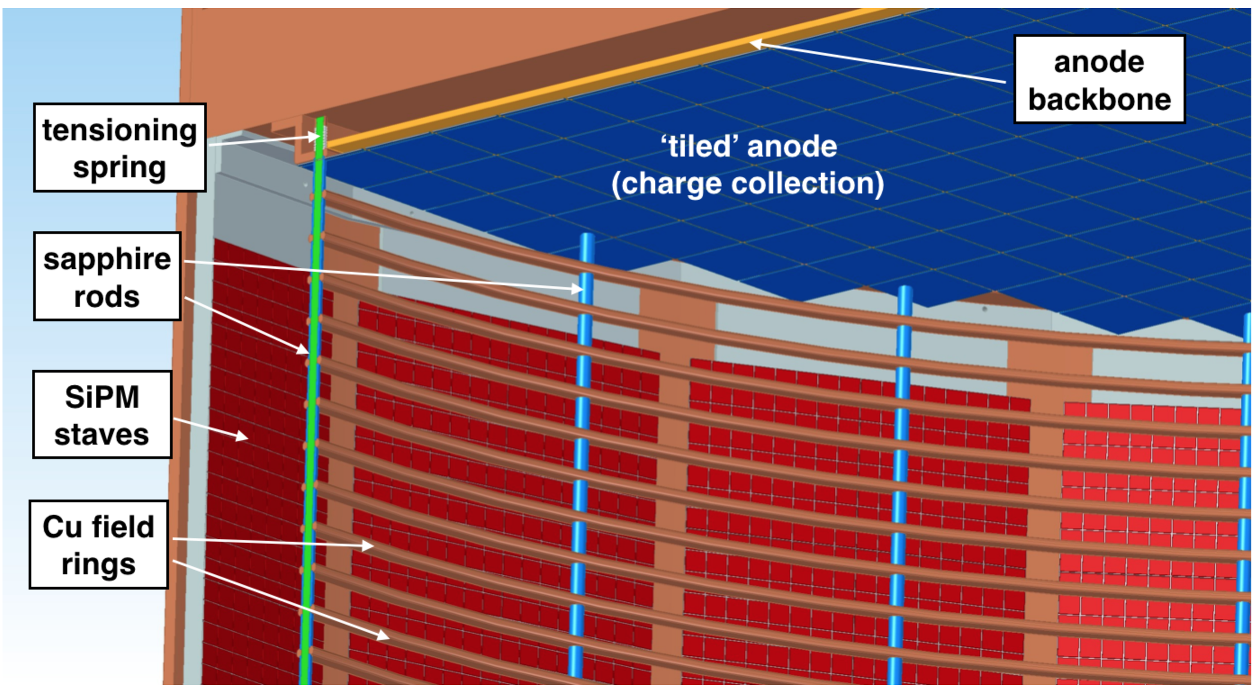

Figure 7: Artist's drawing of the inner view of the TPC near the anode. The field shaping rings will be spaced apart 1.6 cm and held together by long sapphire rods, tensioning springs at each end of the TPC hold the sapphire rods straight. Illustrated is the tiled nature of the anode and the placement of the light detecting Silicon Photomultiplier staves behind the field shaping rings [33].

Unlike in EXO-200, light collection in nEXO is not done by LAAPDs and does not take place behind the charge collection structure; SiPMs are arranged in staves on the side walls of the TPC covering a total 4.5 m^2 area. The choice for SiPMs rather than vacuum photomultipier tubes (PMTs) boasting similarly high gains is due to the fact that the latter have too high radioactivity levels. The placement of SiPMs on the side walls is required by the usage of non-transparent charge tiles but also motivated by the larger photosensitive area that can be achieved by mounting them there. The importance of having high light detection efficiency for good energy resolution is again stressed in the design of nEXO [33]. Modern silicon photomultipliers, unavailable at the time EXO-200 was assembled, were chosen because they provide multiple advantages over PMTs and LAAPDs, beyond just the lower radioactivity. SiPMs have much higher gains than LAAPDs, on the order of 10^6 compared to 10^2 [44, 45]; they are also instrumented to be squares and thus allow for higher photosensitive coverage than circular shaped LAAPDs. The high capacitance and lower gain of LAAPDs was the main limiting factor of the achievable energy resolution $\sigma_E/E = 1.15\%$ at 2.5 MeV in EXO-200 [34]. Without these drawbacks, SiPMs are a promising alternative. Nevertheless, other factors still remain to be optimized for light collection like making the TPC's passive components as reflective as possible at the liquid Xe scintillation wavelength of 175 nm. Designing the field cage to be as open as possible is also important to allow scintillation photons to reach the SiPMs, as well as applying anti-reflective coatings at the aforementioned wavelength to the latter's surface [46]. Given the importance of having highly efficient light collection, the nEXO collaboration is testing and characterizing different models of SiPMs and is one of the groups at the forefront of R&D for SiPMs sensitive at 175 nm [44, 47].

With the usage of newer technology and using the experience acquired from EXO-200 the nEXO collaboration is aiming to achieve a projected $0\nu\beta\beta$ half -life sensitivity close to 10^{28} yrs after 10 years of data collection [48]. Additionally, it is expected to probe the $\langle m_{\beta\beta} \rangle$ mass range between 5.7 and 17.7 meV (refer to Figure 3b) where the range of mass values is due to two different methods used to compute the nuclear matrix elements specified in eq. 2 [49,50].

On top of the already discussed improvements for nEXO, the collaboration is also developing even more powerful background rejection techniques to successfully identify $0\nu\beta\beta$ events. One of these techniques, called Barium-tagging, involves the extraction and tagging of the ^{136}Ba daughter ion resulting from a ^{136}Xe double beta decay. It is described more in detail in [51, 52]. Implementing Ba-tagging successfully in an upgrade to nEXO would represent a major improvement in the rejection of backgrounds as it can differentiate between double beta decay events and background events; effectively leaving only regular $2\nu\beta\beta$ events as the background. The other technique involves detecting the Cherenkov radiation emitted by MeV energy electrons in liquid xenon to discriminate between the different types of interactions. The amount and direction of Cherenkov photons emitted from electrons depends on the latter's energy; a single electron at kinetic energy near $Q_{\beta\beta}$ (produced by photoelectric absorption of a γ at that energy for instance) will produce more Cherenkov photons than two electrons sharing the same total kinetic energy. Hence a precise measurement of the number of Cherenkov photons emitted can improve the ability to reject single-site γ backgrounds [53,54].

1.4 Overview of Silicon Photomultipliers

Silicon photomultipliers are a relatively new type of photosensor using semiconductor technology to detect low light signals with good timing resolution. On top of being insensitive to magnetic fields, requiring low operating voltages and generally coming in compact packages, they are a very viable alternative to photomultiplier tubes or APDs for sensitive light detection applications. SiPMs are collections of single photon avalanche photodiodes (SPADs). The basic working principle of a SPAD, whose structure is illustrated in Figure 8, is to use a semiconductor p-n junction as a means to convert a light

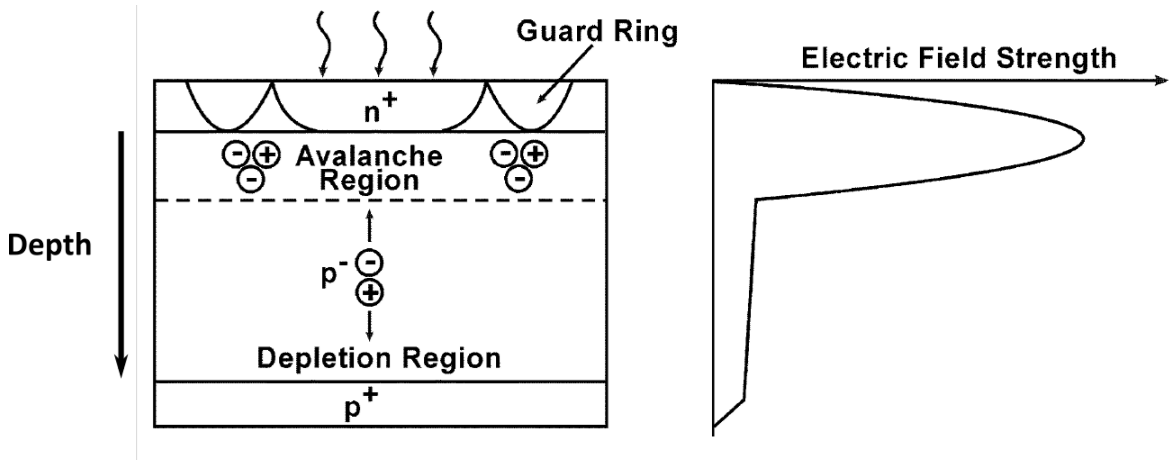

Figure 8: Structure of a single photon avalanche photodiode on the left. When photons create electron-hole pairs, the electric field in the depletion region accelerates electrons creating more pairs, resulting in a charge avalanche. The electric field strength in the p-n junction is demonstrated on the right [55].

signal into a stronger electrical signal. When a photon of sufficient energy hits an electron in the p-n junction it can create an electron-hole pair; if a high enough reverse bias is applied (past the junction's breakdown voltage), the electron can acquire enough energy to produce more pairs through impact ionization. As every electron is accelerated, this results in a charge avalanche in the p-n junction effectively converting an individual photon into a measurable electron current [56]. This mode of operation is referred to as the Geiger mode, in which the response of the SPAD is no longer proportional to the initial number of pairs created. The avalanche photodiode becomes a binary device with an on state whenever hit by a photon. Shown in Figure 9 is a circuit diagram of an SiPM, also featuring the circuit structure of a single SPAD. In the illustrated diagram, C_J is charged and reaches a voltage equal to V_{bias} that is larger than the breakdown voltage of the SPAD's p-n junction. This voltage difference $\Delta V = V_{bias} - V_{breakdown}$, called the overvoltage, greatly impacts the overall performance of SiPMs and affects numerous of their operating parameters as will be discussed shortly. When a photon creates an electron-hole pair in the semi conductor the switch closes and this causes C_J to discharge through

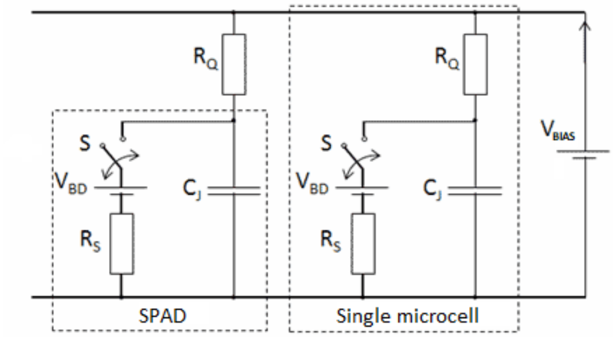

Figure 9: Circuit schematic for a silicon photomultiplier. Multiple SPAD cells in parallel represent the individual pixels of a SiPM. The bias voltage V_{BIAS} is set to be above the SPAD's breakdown voltage. C_J and R_S represent the capacitance and resistance of the SPAD p-n junction, respectively. R_Q is a quenching resistor in charge of stopping the avalanche process [57].

R_S (this corresponds to the avalanche). The quenching resistor R_Q is chosen to have a much higher resistance than R_S; it ensures that when the charge in C_J is getting low (and thus the avalanche is close to stopping), the applied potential V_{bias} cannot create a current through R_Q to perpetuate the avalanche. Following this quenching, C_J is recharged and the SPAD becomes ready for photon detection again. An important note is that the number of photons hitting a single SPAD does not change the signal it produces: as soon as a single (or several) photon(s) hits a SPAD , the avalanche begins and the SPAD cannot detect additional photons until it is recharged.

A SiPM follows the same operating principle, except that it is a large array of micron-sized SPADs (called pixels) in parallel. Every pixel operates independently, being able to produce a current regardless of whether neighboring pixels are ready or recharging. Pixels are grouped together in parallel and their currents sum up, thus assuming the photons hit different pixels, one can get a discrete measurement of the detected photon numbers for low enough photon density. When analyzed, SiPM signals are usually integrated and shown in histograms. This is because individual pixels firing together result in a signal that is proportional to the number of pixels that avalanched. An example of a histogram

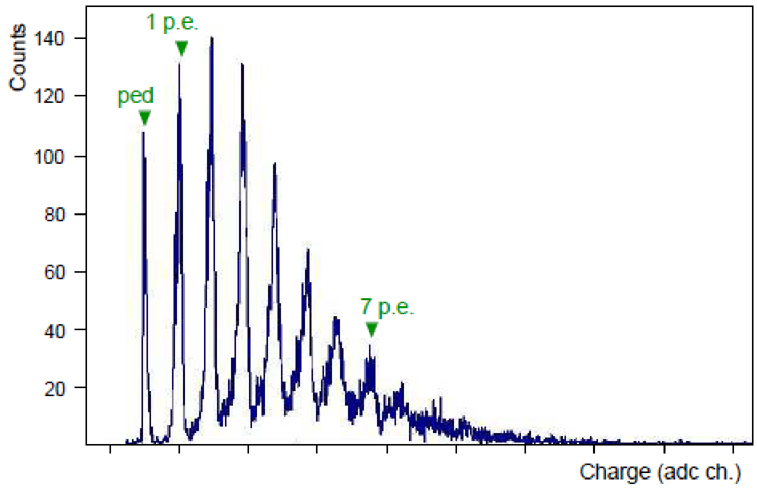

Figure 10: Integrated charge signal histogram for a typical low photon count SiPM signal. The left-most peak is referred to as the "pedestal" and represents the integrated signal for 0 pixels firing, every subsequent peak corresponds to the integrated signal from one more photoelectron avalanche [58].

can be seen in Figure 10, where each peak is separated from its neighbors by roughly the same amount of charge, corresponding to one more (or less) avalanche from a fired pixel. The first peak called the pedestal is the integrated signal when no pixel has been fired. The integral for the pedestal (ped) is the smallest, and its non-zero charge value is due to very small contributions from electrical noise. This distribution of integrated signals follows a Poisson distribution defined by:

$$P(X, \bar{N}_p) = \frac{\bar{N}_p^X \times e^{-\bar{N}_p}}{X!}, \tag{3}$$

with $P(X, \bar{N}_p)$ being the probability of detecting a signal corresponding to X photons if $\bar{N}_p$ photons hit the SiPM on average.

Dark counts are signals indistinguishable from regular photon induced avalanches, instead they arise from thermally excited electrons producing random and spontaneous avalanches. One can measure the dark rate of a SiPM by placing it in a fully light-tight dark environment and measuring the integrated charge signal histogram. The peaks to be populated will mainly be the pedestal and the 1 p.e. peak. Thus, by summing the number of counts for the 1 photoelectron peak (and those beyond) occurring in a certain time interval t one can determine the dark count rate at a specific temperature and ΔV as those are its main driving parameters.

Cross talk between SPADs occurs when one or more avalanches in the Si produce secondary photons (see [59]) that travel to neighboring pixels and induce avalanches there, too. These cross talk avalanches are essentially in-phase with the original ones as the photons take less than picoseconds to travel to neighboring pixels given their micron sized dimension. Therefore, when looking at the time trace of a SiPM pulse on a voltage or current measuring device (such as in Figure 11), there is no way of knowing which pulses are due purely to primary photons since every pulse corresponding to a signal that is 2 p.e. or larger can have cross-talk contributions. Thus, by using the dark count rate integrated spectrum, one can obtain the cross talk probability by making use of the fact that there will be peaks corresponding to 2 p.e. or more. This probability can also be written as:

$$P_{crosstalk} = 1 - \frac{N_{1p.e}}{N_T - N_0}, \tag{4}$$

with $N_{1p.e}$ being the number of observed 1 photoelectron events, and N_T being the total number of peaks while N_0 is the number of counts at the pedestal [58].

Afterpulses are a phenomenon that happens when electrons are trapped by impurities in the silicon and released as the SPAD is recharging. This triggers a secondary avalanche and results in a secondary lagging pulse. Some after pulses can be seen in dark blue in Figure 11. Given any photon-induced avalanche in the silicon has a chance of producing an afterpulse, the amount of afterpulsing is measured as a probability given by:

$$P_{a.p.} = \frac{N_{a.p.}}{N_T - N_0}, \tag{5}$$

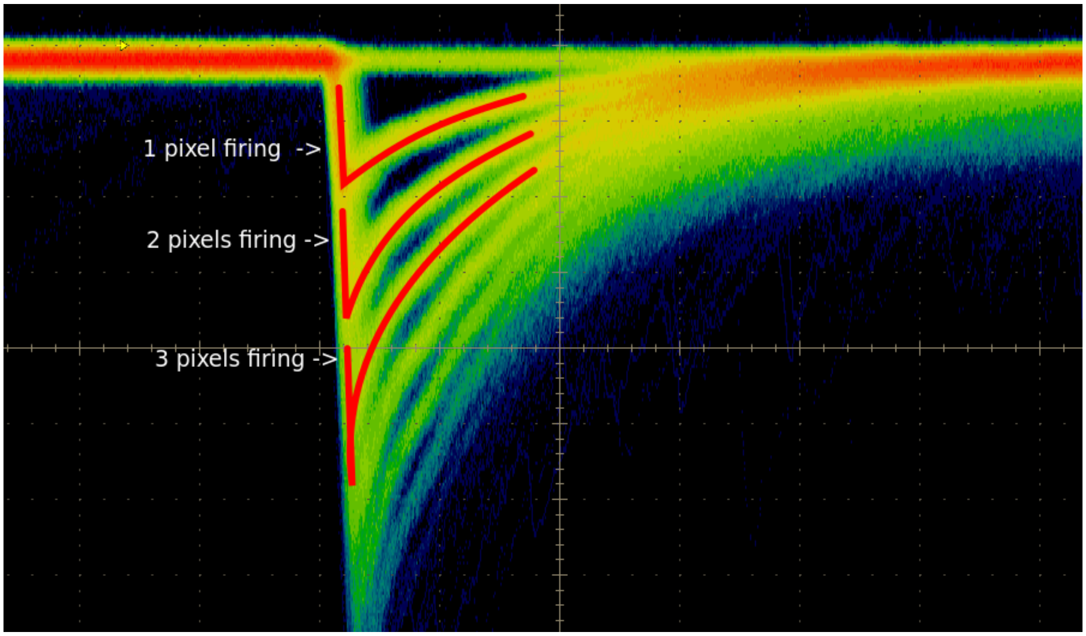

Figure 11: Examples of SiPM time trace signals. The increase in amplitude with increasing photoelectron number is clear. Peaks with crosstalk contributions are indistinguishable as they remain in phase. Afterpulsing is represented by secondary peaks (in dark blue here) following the signal from the main avalanche [60].

where $N_{a.p.}$ is the number of afterpulses that occur and N_T and N_0 are as defined in equation 4.

An SiPM's photon detection efficiency, i.e. the probability it detects a photon that hits it, is defined as $PDE = QE \times \epsilon_{geo} \times \epsilon_{Geiger}$ where QE is the quantum efficiency of a photon producing an electron-hole pair in the p-n junction, ϵ_{geo} is the percentage of the SiPM area that is photosensitive and ϵ_{Geiger} is the probability that the generated electron-hole pair starts an avalanche [61]. Alternatively, one can measure the PDE by using information from eq. 3 and a dim light source known to emit a low photon number N_S (N_S can be measured with a calibrated PMT, for example). From the distribution of integrated signals for a total of N_T events, the probability to measure 0 photons (the only signal not affected by cross-talk or afterpulsing) is given by $P(0, N_{det}) = N_0/N_T = e^{-N_{det}}$ where N_0 is the number of counts at the pedestal and N_{det} the mean (number of photons) of the Poisson distribution, respectively. Thus, one can obtain $N_{det} = \ln(N_T/N_0)$ corresponding to the average number of photons detected by the SiPM. However, dark counts contribute to N_T, and thus to N_{det}, which means their contribution must be subtracted to obtain the true number of photons detected by the SiPM. This dark count contribution is defined as $N^D_{det} = \ln(N^D_T/N^D_0)$ where N^D_T and N^D_0 are the total number of events and the pedestal counts, respectively, for a distribution of integrated dark count events. Finally, the photon detection efficiency of an SiPM can also be expressed as $PDE = (N_{det} - N^D_{det})/N_S$ [62,63].

The final main parameter defining SiPMs is the gain. The gain of a SiPM can be defined as:

$$G = \frac{QDC/ch}{e^- \times K_{amp}} \times \Delta_{pp}. \tag{6}$$

Where QDC/ch represents the amount of charge in 1 unit of the integrated adc signal (the x-axis of Figure 10), e^- is the electron charge, K_{amp} are extra amplification factors from additional electronics and Δ_{pp} is the distance between two adjacent peaks.

The SiPM properties described above are all dependent, to various degrees, on overvoltage ΔV and temperature, therefore a thorough characterization as a function of these two parameters is extremely important to the proper operation and optimization of SiPMs for different applications [44,62,64,65].

1.5 Scintillation in Liquid Xenon

Xenon, along with helium, argon and krypton, is part of a category of materials called noble gases. These types of materials exhibit the property of being able to emit light when excited in collisions with ionizing radiation. This gives noble gas detectors two processes through which energy deposition from ionizing particles can be measured: the collection of charge and light, the latter allowing timing information to be obtained. Over the past decades, liquid xenon in particular has been used as an active medium in many detectors such as the gamma-ray imaging telescope LXeGRIT [66], XENON100 [67] a time projection chamber trying to detect dark matter, EXO-200, a 175 kg TPC trying to observe neutrinoless double beta decay [36], and MEG searching for the $\mu^+ \rightarrow e^-\gamma$ decay using liquid xenon [68]. LXe has multiple properties that make it a desirable detector medium; it has a high atomic number and density, $Z = 54$ and $\rho = 3$ g/cm^3, respectively [69], giving it high stopping power and allowing for high energy deposition per unit distance. The boiling temperature of xenon is 164.9 K at STP [69], which is relatively high compared to other noble scintillators like argon or krypton, lowering requirements when it comes to the cooling power needed to keep running an experiment that uses LXe. One point of importance among all scintillators is their purity requirement; presence of impurities in their volume leads to trapping of ionized electrons and absorption of their scintillation light, both detrimental to energy deposition measurements [70].

LXe scintillation photons have a wavelength of 175 nm [46]; coined as "Vacuum Ultraviolet" (VUV) radiation due to their low wavelength. This term arises from the fact that sub 200 nm wavelengths are absorbed over very short distances in air thus usually requiring the use of vacuum setups if they are to be detected with good efficiency [71,72]. LXe scintillation is produced by the following two mechanisms:

$$\begin{aligned} \mathrm{Xe}^+ + \mathrm{Xe} &\rightarrow \mathrm{Xe}_2^+ \\ \mathrm{Xe}_2^+ + e^- &\rightarrow \mathrm{Xe}^{**} + \mathrm{Xe} \\ \mathrm{Xe}^{**} &\rightarrow \mathrm{Xe}^* + heat \\ \mathrm{Xe}^* + \mathrm{Xe} + \mathrm{Xe} &\rightarrow \mathrm{Xe}_2^* + \mathrm{Xe} \\ \mathrm{Xe}_2^* &\rightarrow 2\mathrm{Xe} + h\nu. \end{aligned} \tag{7}$$

$$\begin{aligned} \mathrm{Xe}^* + \mathrm{Xe} + \mathrm{Xe} &\rightarrow \mathrm{Xe}_2^* + \mathrm{Xe} \\ \mathrm{Xe}_2^* &\rightarrow 2\mathrm{Xe} + h\nu. \end{aligned} \tag{8}$$

The first process (in eq 7) involves Xe^+ ions, and excited states of xenon atoms denoted as Xe^* and Xe^{**} which combine into xenon excimers Xe_2^*; the second process (in eq. 8) only involes excited xenon atoms Xe^* and excimers [73]. The emitted VUV scintillation photons are denoted as $h\nu$.

A main parameter of interest for scintillators is the W-value, it denotes the average energy needed to create one electron-ion pair. If an incoming particle deposits E_T energy in a scintillator, energy conservation requires the following equality to be satisfied [74]:

$$E_T = E_i \times N_i + E_* \times N_* + N_i \times \epsilon. \tag{9}$$

Where E_i and N_i are the energy required to ionize an electron and the number of electron-ion pairs produced in the liquid volume, E_* and N_* are the energy required to excite an atom and the number of excited atoms respectively, and ϵ is the average kinetic energy of the ionized electrons. The W-value can be obtained by diving E_T by the number of electron-ion pairs [73]:

$$W = \frac{E_T}{N_i} = E_i + E_* \times \frac{N_*}{N_i} + \epsilon. \tag{10}$$

This is the quantity of interest in scintillators because it relates to the ionization yield, i.e. the number of electron-ion pairs produced per unit energy. Time projection chamber-based experiments like EXO-200 owe a lot of their energy resolution to the collection of charge during interactions; when ionizing radiation enters the TPC it deposits energy in the LXe volume. This energy deposition can ionize atoms whose electrons are drifted using an applied electric field and collected at the walls of the TPC. Thus, a good understanding of the mechanism behind the creation of electron-ion pairs coupled with an efficient charge collection system is important if an accurate measurement of energy deposition is to be made.

Nevertheless, as shown in eq. 7, electron-ion pairs can still recombine to produce scintillation light, which motivates the definition of an "average energy per photon emitted" related to the scintillation yield. The average energy needed to create one scintillation photon W_γ, assuming there is no photon absorption by impurities, [75] is given by:

$$W_\gamma = \frac{E_T}{N_i + N_*} = \frac{W \times N_i}{N_i + N_*}. \tag{11}$$

Another characteristic that makes liquid xenon a very attractive detector material compared to other noble gases beyond its higher stopping power is its low W-value of 15.6 eV [76]; being significantly lower than those of Ar and Kr. Xenon is the noble gas with the lowest W-value, giving it the highest ionization yield [73,77]. With the relevant background and theory presented, the following chapter introduces and gives and overview of the experiment discussed in this thesis and its main components.

2 Development of a VUV Electroluminescent Light Source

2.1 Experiment Overview

As discussed in chapter 1, nEXO's ability to successfully detect a $0\nu\beta\beta$ decay, if it occurs, is largely limited by the detector's energy resolution. The efficiency of LXe scintillation light collection is a major component of the energy resolution and is largely dependent on the performance of the SiPMs. Thus, a good characterization of the different operating parameters of the SiPMs, overviewed in section 1.4, is necessary for proper optimization of light collection and understanding of the measured signal. The remainder of this work discusses the working principle, experimental setup, and results from a controlled VUV electroluminescent light source aimed to be used for SiPM characterization. The electroluminescent light source (ELS) is a project that was started in 2016 and various efforts have gone into designing, machining, simulating and assembling the components for the light source as well as testing its charge collection capabilities ([78–81]). The main topics treated in this thesis will be a verification of the aforementioned charge collection and the first results of VUV photons produced by the light source. Unlike in nEXO where liquid xenon is used, this light source uses gaseous xenon and it does not require any cryogenic equipment to operate. It should be noted that liquid and gas xenon do not emit photons of exactly the same wavelength; LXe emits 175 nm [46] photons whereas gaseous xenon (GXe) peaks at 172 nm [82]. The width at half maximum of the emission lines are ~ 10 nm and ~ 12 nm for the liquid and gas phase, respectively [46, 83]. Nevertheless, these wavelengths are so close that no significant impact is expected when used in SiPM testing and characterization.

The working principle of the GXe electroluminescent light source is illustrated in Figure 12. An external LED or flash lamp light source ($\lambda = 265$ nm and $E_{photon} = 4.68$ eV) back illuminates a sapphire window coated with silver, acting as the photocathode (work function 4.52-4.74 eV [69]), located inside a GXe filled vacuum chamber, and produces photoelectrons. A needle shaped anode inside the chamber facing the photocathode is biased at high potential (kV range) and generates an electric field that accelerates the electrons. Once they acquire sufficient energy they can excite, but not ionize, xenon atoms; thus, this method of light emission uses the mechanism described in section 1.5, equation 8, or [84]. The external light sources chosen for developing this project were the Thorlabs M265L3 Mounted LED (265 nm/10 mW [85]) and the Hamamatsu L11035-03 xenon flash Lamp (185-2000 nm/5 W [86]) illustrated in Figure 13. The components inside the chamber are made of stainless steel, aluminum and copper, the latter gold plated, whose work functions are respectively 4.31 eV [87], 4.06-4.26 eV, and 5.31-5.47 eV [69]. Photons produced at the lower end of the Xe flash lamp's emission spectrum, spanning the range

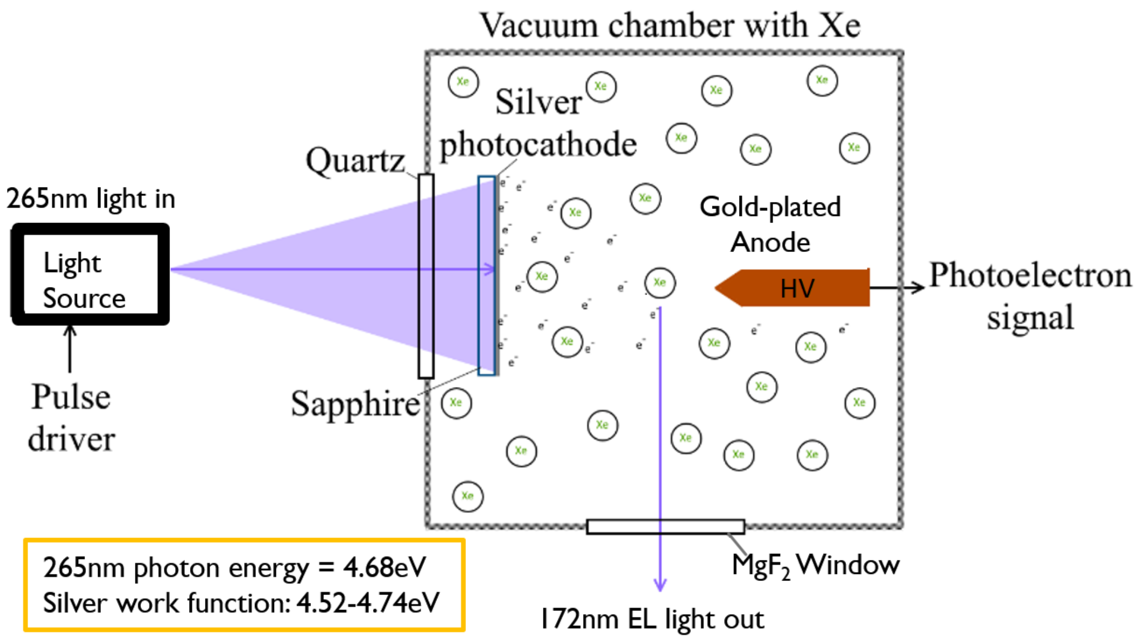

Figure 12: Diagram for the working principle of the ELS. An external UV light source is used to produce photoelectrons from a silver photocathode. Those are drifted in a gas xenon volume, exciting the xenon atoms which produce 172 nm electroluminescent light. The charge signal is collected at an anode, biased with a high voltage (HV), that also generates the drift field, while the light signal is measured with a PMT placed at the MgF_2 window of the vacuum chamber. Figure modified from [79].

185 - 2000 nm (0.6 - 6.7 eV), carry sufficiently high energy to generate photoelectrons from all types of materials which is problematic since only photoelectron (p.e.) emission on the silver photocathode is desired in order to create a well localized electron cloud to achieve short output electroluminescent pulses. For this reason, a 265±2 nm center frequency (12±2 nm FWHM) band-pass filter was used to limit the wavelengths impinging on the Ag cathode [88] in some measurements. Additionally, focusing lenses not shown in Figure 13 are used for both light sources to focus as much of their emission cone onto the photocathode as possible.

The anode is connected to a SHV feedthrough and depending on the desired voltage is either biased with a ±30 V Rohde Schwarz NGE100 (see [89]) or a ± 5 kV Bertan high voltage power supply. Given that the photoelectrons are emitted in bunches and

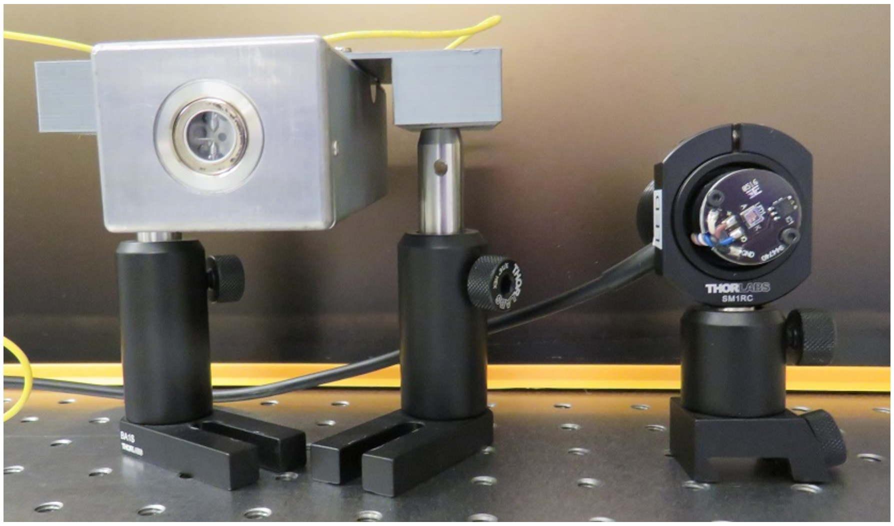

Figure 13: UV light sources used to illuminate the silver photocathode for photoelectron production. On the left is a 5 W Hamamatsu L11035 xenon flash lamp used with a 265 nm bandpass filter (not shown) to limit its normally broad (185-2000 nm) emission spectrum; the filter decreases the lamp's power by about one order of magnitude. On the Right is a 10 mW mounted Thorlabs M265L3 LED with a narrow emission spectrum centered around 265 nm (11 nm FWHM) [85].

at regular intervals, a charge sensitive preamplifier (CSP) is used to measure the charge produced by each light pulse. CSPs are devices that integrate the current in events and output a voltage proportional to the charge collected. For this measurement a Cremat CR-Z-110-HV charge sensitive preamplifier [90] is used.

To produce xenon electroluminescence, the flash lamp or LED is used (with a lens to focus its output) to illuminate the cathode through a 51 mm diameter quartz viewport as shown in Figures 12 and 14a; meanwhile the 172 nm light is measured by a PMT placed immediately at the exit of a MgF_2 window (Figure 14b). The short attenuation length of 172 nm light in air due to absorption by molecular oxygen (few mm) is an issue that is mitigated by purging the volume between the PMT and the MgF_2 window with nitrogen gas, which exhibits much lower absorption [72, 91].

Given the sensitive nature of the experiment any external light leakage is to be eliminated, thus the whole setup is enclosed in a light-tight dark box shown in Figure 15

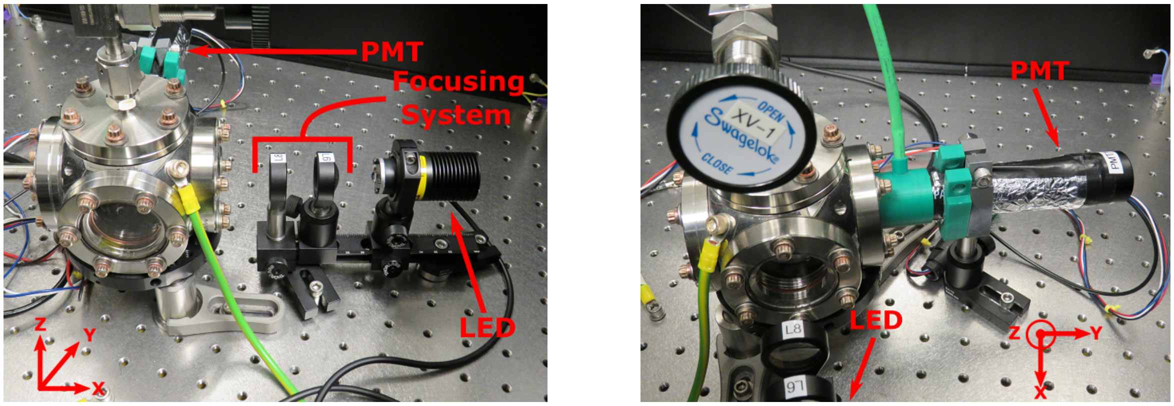

(a) LED and Lens Focusing System. **(b)** PMT Positioned for Light Collection.

Figure 14: On the left is the light emitting diode with two lenses to focus the beam onto the photocathode located in front of a 51 mm diameter quartz viewport. The three components are placed on a small optical rail to allow fine tuning of distances and achieve the best possible focusing. On the right is shown the PMT placed immediately at the exit of a 25 mm diameter MgF_2 viewport, a tube connected to the green cylindrical fitting at the front of the PMT flushes nitrogen gas to reduce the absorption of the 172 nm wavelength VUV photons.

and further covered with a thick black blanket inside to prevent reflections of the 265 nm wavelength from the inner panels of the box to enter the PMT. A panel with feedthroughs at the front of the box is used to manage the electrical and purge gas connections.

The ELS aims to produce light pulses to test and characterize SiPMs that will be used in nEXO, which, as mentioned in section 1.3 will be detecting the 175 nm xenon scintillation light emitted during $2\nu\beta\beta$ and $0\nu\beta\beta$ decays. The time-scale of the emitted scintillation light is on the ns time scale [92]; however, nEXO is limited to μs scale sampling rates (see [33]) in order to prevent liquid Xe boiling from the higher power required by faster sampling rates. Nevertheless, the conditions under which the SiPMs will be tested (ns time-scale pulses and single photon measurements) are much more stringent than the application they will be used for; thus, one goal of the presented project is to minimize the width of the pulses produced by the ELS. The pulse duration of the 172 nm light is expected to change as a function of the duration of the input 265 nm pulse. This is be-

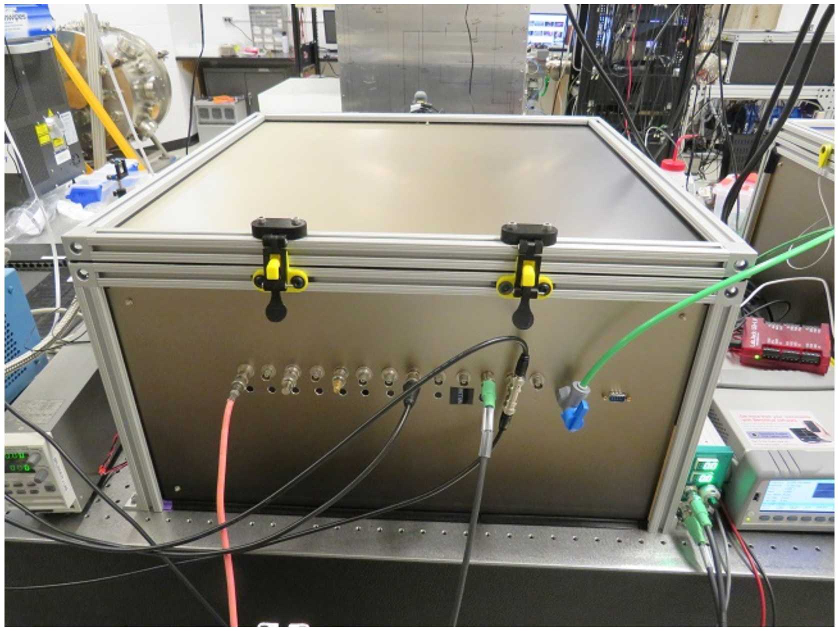

Figure 15: Dark Box to house the electroluminescent light source. The box is fully light-tight to prevent outer light leakage from entering the PMT. The front panel features feedthroughs to power the different electronics inside the box such as the CSP, PMT, the 265 nm light sources and to read the output signals, as well as a feedthrough valve for the nitrogen gas purge. All panels are electrically grounded to the optical table to prevent RF signal pickup from other experiments.

cause shorter input pulse durations result in lesser time spreads between the first and last emitted photoelectrons. The shortest pulses the xenon flash lamp can emit have FWHM of approximately 200 ns (according to [86]), whereas the LED pulse width can go to as low as 20 ns in duration, with the drawback of much reduced initial photons. Various parameters of the experiment can be adjusted in the attempt to produce electroluminescence in the xenon. The ones described in this thesis are the variation of xenon gas pressure inside the chamber and the effect on light production of two different anode geometries maintained at two fixed distances from the photocathode.

2.2 Xenon Cell Design

The design philosophy of the chamber used for the electroluminescent light source was to build a modular chamber with few, simple-shaped components to allow for easy modification. A CF 2.75″ spherical cube from Kimball Physics is used for the core of the vacuum chamber [93]. On three of the cube viewports are installed windows. As mentioned earlier, a $\varnothing = 51$ mm diameter quartz viewport is placed at the ”front” of the chamber from where the input pulses arrive; the viewports on the sides are $\varnothing = 51$ mm calcium fluoride and a $\varnothing = 25$ mm magnesium fluoride windows. They are chosen due to their higher 172 nm wavelength transmission compared to quartz ($\sim 85\%$ for MgF_2) [94]. For the first test and results described in this thesis, only the MgF_2 window was used as its transmission is slightly better than that of CaF_2 and only one PMT was available, future measurements investigating the topology of the EL light emission or its timing can use both windows. Despite not directly being used, the larger size of the CaF_2 viewport offers a good view of the inside of the chamber and can serve to approximate the distance between the needle and the cathode to see if it is close to the target separation. There are no concerns of light leaving the chamber and reflecting back in through the CaF_2 window given the dark blanket used to cover the experiment.

Pictures of the chamber and setup are shown in Figures 14a and 14b. A view of the inside of the chamber with the main components labelled is shown in Figure 16. The input light pulse is transmitted through both a quartz viewport and a sapphire window before arriving at the silver photocathode. The silver film thickness is small in order to allow photoelectrons to escape the bulk of the material. However, this also leaves the photocathode partially transparent which results in 265 nm light not only propagating into the chamber from the sides of the sapphire holder but also through the silver film. Given the reflective nature of the metal components inside the chamber, a fraction of the input pulse is reflected out through the MgF_2 viewport and is also detected by the PMT; this is referred to as “leakage light”. The 3 standoffs that support the sapphire

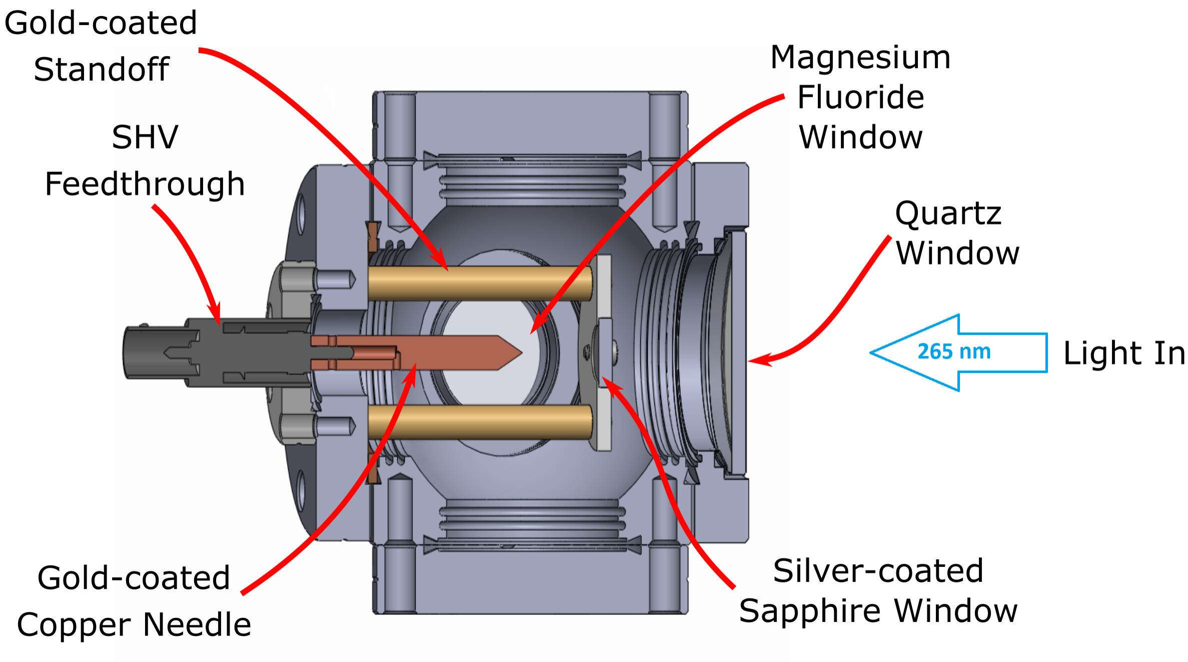

Figure 16: Inner structure of the ELS vacuum chamber. Labelled are the main components of the chamber. The anode makes contact with a push-on SHV feedthrough welded to a CF 1.33″ flange. Also shown are the three standoffs holding the sapphire window; they are gold-plated like the copper anode, to reduce their susceptibility to photoelectron emission. The quartz and MgF_2 viewports for light input and output respectively are also labelled.

holder, along with the copper anode needle, receive incident 265 nm light both from direct transmission through the silver as well as from reflection off the chamber walls. To minimize the undesired photoelectron emission from these components they were gold-plated. Gold has a work function of 5.31-5.47 eV which is higher than the energy of incident 265 nm (4.68 eV) photons. The use of focusing optics in front of the flash lamp and LED was observed to slightly increase the intensity of the light impinging on the 12.5 mm diameter photocathode and thus increase photoelectron production but to also reduce the amount of leakage light.

The only component with an applied potential in this assembly is the anode needle, everything else is held at ground. In this case, the electric field inside the chamber is purely due to the anode needle and its geometry as well as the bias applied to it. Two different geometries were tested in this thesis, a gold-coated copper needle and a thin stainless steel needle which are illustrated in Figures 17a and 17b, respectively.

(a) Gold-plated Copper Anode.

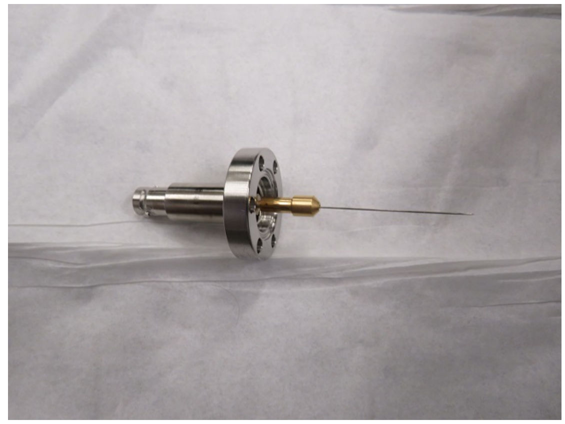

(b) Stainless Steel Anode.

Figure 17: On the left: The gold-plated anode needle pushed on the the welded SHV pin. Firm contact between the needle and the pin is ensured by two set screws, a venting hole to evacuate any trapped air is also visible. On the right: The stainless steel needle is inserted and fixed into a gold-plated push-on connector via set a screw. The connector is pushed on to the SHV pin to ensure electrical contact.

Different needle geometries were investigated to see how a different field shape and gradient affects the production of electroluminescent light. Needles with sharp tips are expected to produce fields that spread over a smaller region but have much stronger gradients; with the opposite being the expectation for needles with larger tips. The stronger gradient of the stainless steel needle will accelerate electrons over a shorter distance than the gold-plated needle. Since this distance is shorter the electrons are also expected to collide with fewer xenon atoms and lose less energy due to elastic collision. However, given the much faster decay of the field strength when using a sharp needle, depending on the cathode-anode separation, it is possible that its magnitude at the silver film is too weak to successfully attract the photoelectrons (which are released from the photocathode at sub eV energies). Given its stronger gradient near the tip, the stainless steel needle is expected to produce a larger number of photons per photoelectron. This can be understood by looking at the number of electroluminescent photons produced per electron per unit length in xenon as a function of the applied E-field and pressure found in [84]:

$$n_{ph}/x = (151E/p - 131) \times p, \tag{12}$$

where n_{ph} is the number of photons produced, x is the distance, E is the electric field (in kV/cm) and p is the pressure in bar. This equation can be rearranged into

$$x = \frac{1}{(151E/p - 131) \times p}, \tag{13}$$

to give the distance required to create one photon per electron. From this, it is clear that a stronger electric field results in shorter drift distance necessary for photon production. When applying high voltages in gas xenon, there is a pressure dependent breakdown voltage where direct ionization of the atoms begins as a result of the strong field; this causes the normally insulating gas to become conductive and may result in electric discharge within the Xe. The breakdown voltage threshold (described by Paschen's Law) is a function of both the gas density and the distance between the two electrodes across which the electric field is generated. Figure 18 shows the threshold DC voltage for pure gas xenon for two recent experiments discussed in [95, 96] as a function of Pd (pressure times distance). Both use plates for the anode and cathode and the former investigates pressures between 7 Torr - 196 Torr with a gap of 0.13 mm while the latter uses a 5 mm gap and pressures between 700 Torr - 8000 Torr. The ELS uses a very different electrode configuration that is not made of parallel plates resulting in different voltage thresholds for Xe breakdown. For instance, using the stainless steel needle with 600 Torr of Xe, and a photocathode-anode distance of 7.5 mm, results in a Pd value of 450 Torr cm but the breakdown threshold for this pressure in the ELS has been observed to be 2.4 kV, rather than the expected ~ 10 kV based on the data from Figure 18. This significantly lower threshold voltage is likely due to the fact that the ELS uses needle shaped anodes, whose

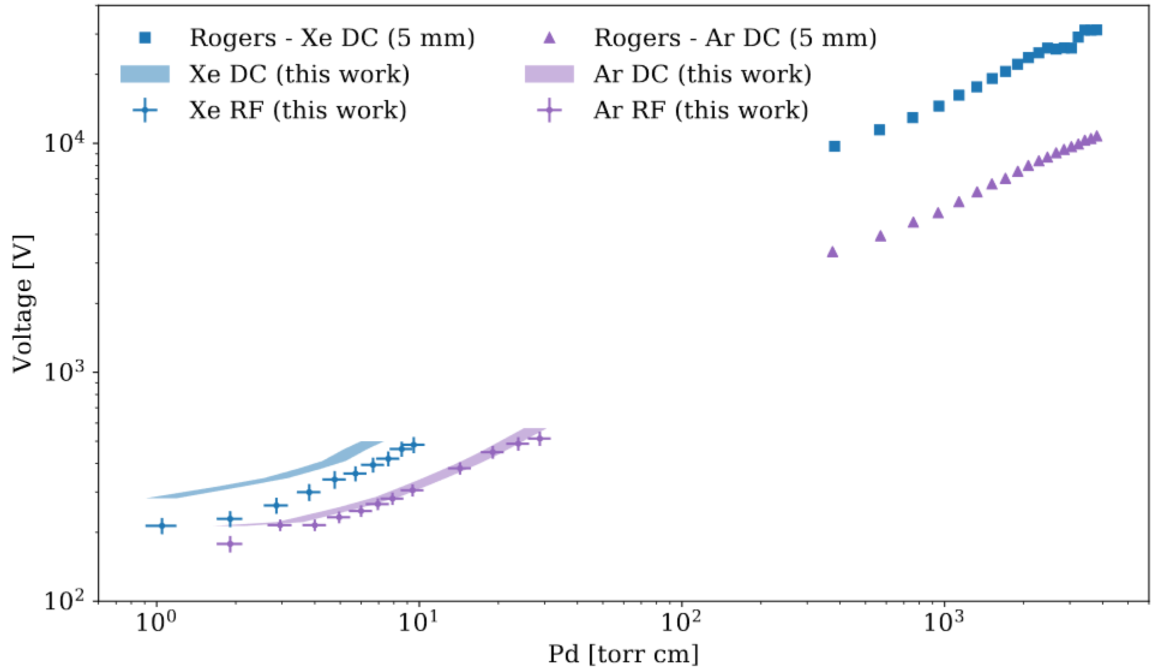

Figure 18: Breakdown voltage threshold in gas xenon as a function of pressure multiplied by distance between electrodes. This plot and the data for Pd $< 10^2$ Torr are from [95] while the data for Pd $> 10^2$ is from [96].

field is much stronger near the tip. This creates electric fields strong enough to cause breakdown at much lower voltages. This is expected to occur at lower applied biases for the steel needle than the gold one due its pointier tip. Despite the large difference between breakdown thresholds cited in literature and those observed in the ELS the overall trend of increasing voltage with increasing pressure for a fixed gap is maintained.

2.3 Xenon Gas System

Supply, purification, and recovery of the xenon gas is done by a gas handling system equipped with a turbomolecular pump and connected to the ELS. The structure shown in Figure 19 is a mobile aluminum profile cart which holds the gas handling system, mainly built with ultra high vacuum (UHV) compatible Swagelok Vacuum Coupling Radiation (VCR) tubing. The turbomolecular pump is used to ensure a clean environment for the

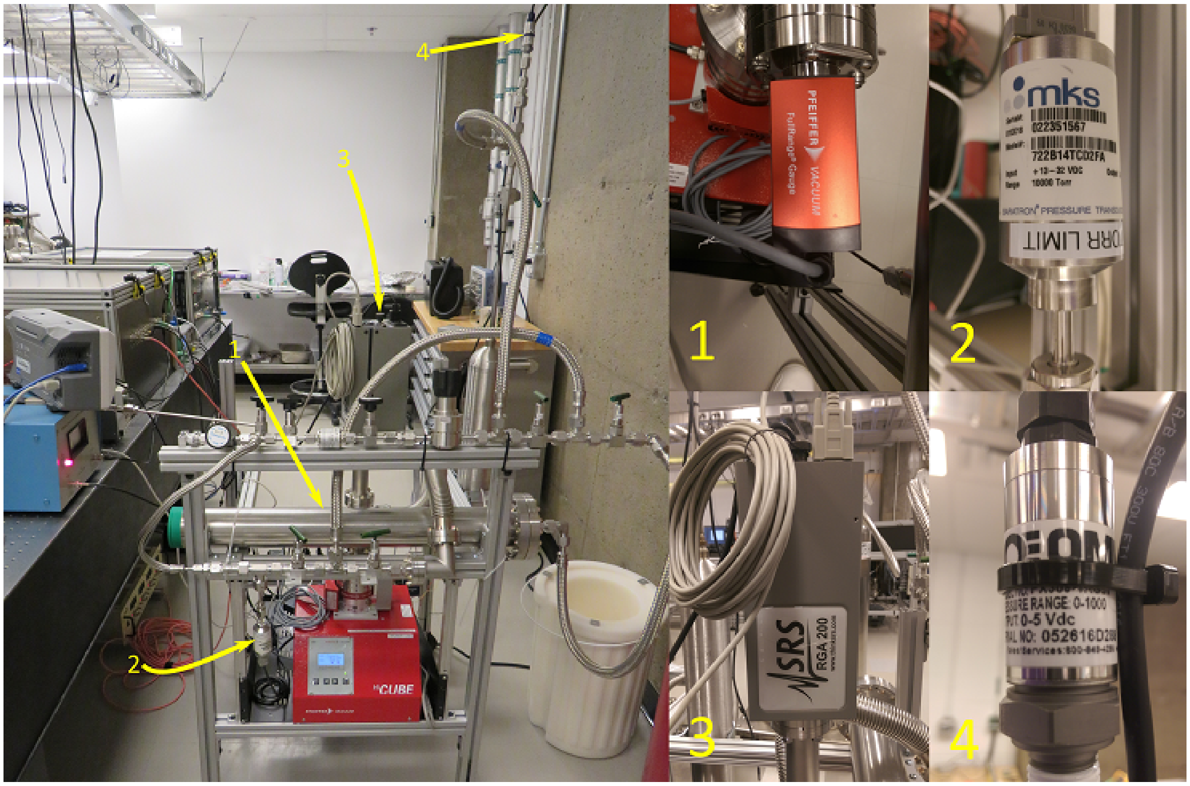

Figure 19: The gas handling system used for the pumping, filling and recovery of the xenon gas used in the ELS. In red is a Pfeiffer HighCube Eco pump stand coupled with a Pfeiffer PKR361 full range pressure gauge (gauge labelled as 1) used to reach vacuums of 10^{-10} Torr. The system is also equipped with an Omega PX309 [98] (4) gauge to measure the gas pressure in the xenon tank and an MKS 722B Baraton [99] (2) used to determine the pressure inside the chamber. To recover the xenon gas from the system, the white dewar is filled with liquid nitrogen and the vertical cylinder containing the xenon is lowered into it. A residual gas analyzer (3) is also attached to the system to perform leak checking and ensure good vacuum quality before any xenon is allowed to flow.

xenon gas as the latter's purity directly influences its light yield. Thus the chamber and the xenon pathway in the gas handling system are pumped to a vacuum as low as 10^{-10} Torr before any xenon is deployed. A Xe purifier removes impurities at a level of 1 part per trillion (ppt) [97].

There is a VCR feedthrough on the left panel of the dark box that enables the vacuum tubing connection between the gas handling system and the ELS chamber. The gas handling system also features three pressure gauges, a xenon purifier, a pressure regulator and a residual gas analyzer (RGA) along with valves to close off different parts of the system depending on what it is being used for. The system has two gas tanks, one which holds the xenon gas and another one that is typically pumped to vacuum and can be used to temporarily lower the xenon pressure in the system. This allows for measurements at lower pressure values to be taken without having to fully recover the gas, do a full vacuum pump down of the system, and refill it again. The gas handling system, while mostly used for the ELS chamber, can be disconnected and moved to other experiments given the mobile cart it is built on. As mentioned, before filling with xenon, the system is pumped to vacuums around 10^{-10} Torr; it is then leak checked using helium and the RGA. When filling the chamber with xenon, the valves are opened such that all the gas that reaches the chamber flows through the pressure regulator and the xenon purifier, the latter being used to remove impurities such as CO_2, CO, O_2 and H_2. The regulator lets in increasing amounts of gas until the target pressure is reached on the Baratron after which the regulator and all the valves are closed. A detailed diagram of the gas handling system is presented in Figure 20 with the Xe filling path being shown in red.

Given the high price of xenon gas, it is desirable to reuse the available amount for multiple chamber fillings, and since the Xe gas system is a closed system, the most practical recovery option is cryopumping. For the recovery of the xenon, a dewar (shown in the bottom right of the gas handling system in Figure 19) is filled with liquid nitrogen and the xenon tank is lowered into it. The liquid nitrogen at 77 K cools the cylinder far below the Xe condensation point thus greatly lowering the pressure inside the tank as the xenon liquefies. When the valves are open in the remainder of the system, the xenon gas is effectively sucked back into the tank. The cryopumping path is different from the filling path as gas cannot flow backwards through the purifier and the pressure regulator. For this reason, by closing different valves, a second path to the xenon gas cylinder can be created as illustrated in blue in Figure 20.

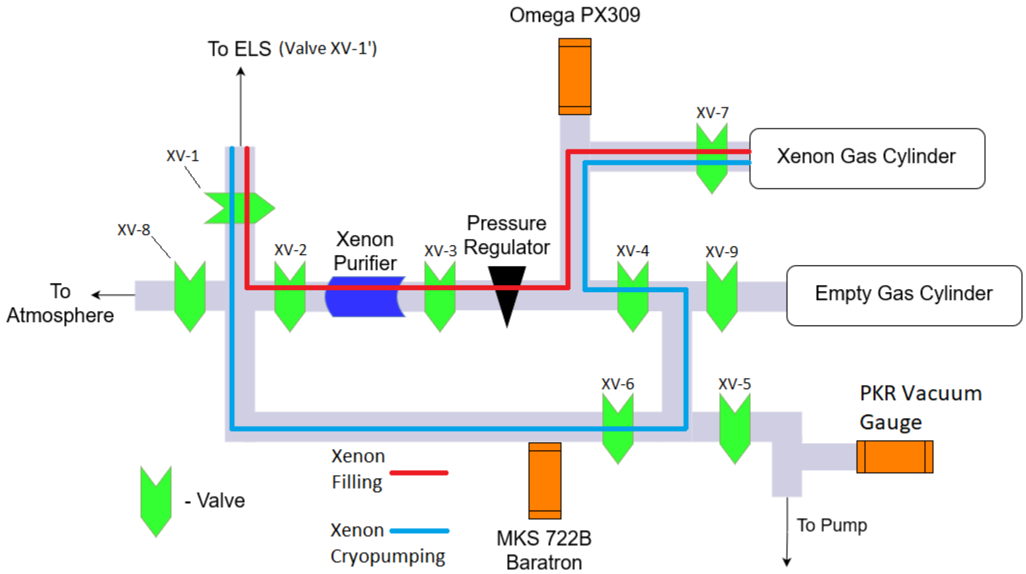

Figure 20: Diagram for the ELS gas handling system, along with main components and outlets. Labelled valves (in green) are located throughout the system to close off different areas depending on whether the system is used for filling the chamber with xenon or for cryopumping the gas back into the cylinder; the gas xenon paths for both filling and cryopumping are shown in red and blue, respectively. The Baratron is used to measure the gas pressure in a volume which includes the chamber, whereas the Omega is used to monitor the gas pressure in the xenon bottle (at a level of 2900 Torr when all the gas is in the bottle). Also shown is the secondary gas cylinder usually pumped to vacuum that can be used to reduce the pressure in the chamber without having to cryopump and refill.

In Figure 21a, the typical evolution of the pressure measured by the Baratron during a chamber filling is shown for a final pressure of 1450 Torr. The system is initially at vacuum due to a full pump down of both the chamber and the gas handling system (region I). The full pump down is done prior to Xe filling to remove ambient air that slowly leaks into the vacuum tubing or that is introduced into the chamber when the latter is opened for modifications. Pumping is also used as a measure against H_2O desorption from the chamber walls and to remove other gases such as N_2, He, Kr, Ar, as well as many hydrocarbons and fluorocarbons which are not removed by the purifier. With the system at vacuum, valves XV-2 and XV-3 in Fig. 20 are opened (region II), which releases a very small amount of leftover xenon from the previous filling (note from Figure 20 that the

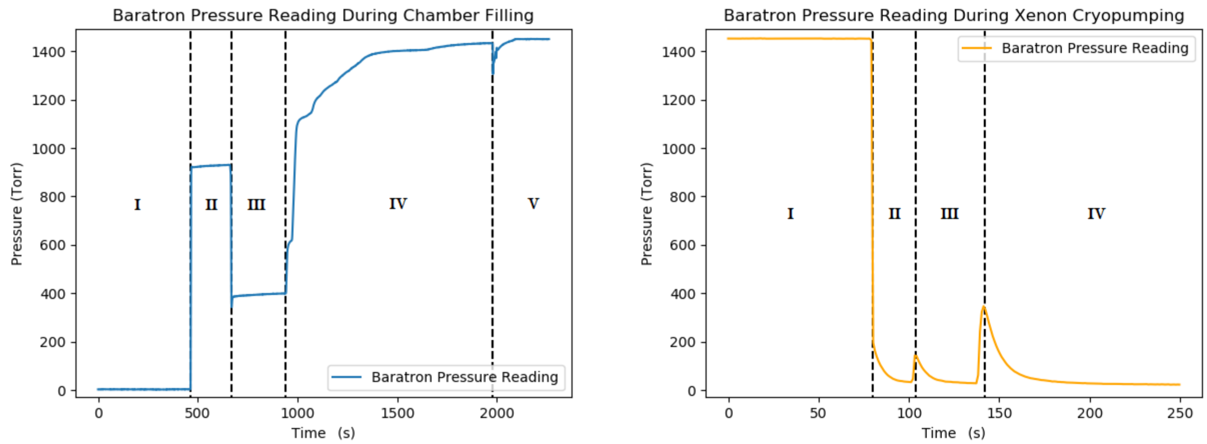

(a) Pressure Reading During Filling. **(b)** Pressure Reading During Cryopumping.

Figure 21: On the left: Baratron pressure reading during filling. Regions I-IV represent the different stages of the filling process. In region I, the gas system is at vacuum, in II the valves around the purifier are opened and the remaining xenon from previous operations is released. In III the chamber is opened which reduces some of the pressure and then closed; region IV represents the gradual pressure build up in the system using the regulator. In V, the chamber is opened again and the regulator adjusted so that the pressure in the system reaches 1450 Torr. On the right: The Baratron reading during the xenon cryopumping. In region I, the system is at a steady 1450 Torr pressure, whereas in region II the valves to the liquid nitrogen cooled gas cylinder are opened causing a large drop in pressure as the xenon gets cryopumped back into the cylinder. Regions III and IV represent the cryopumping of the gas in the VCR tubing between the gas handling system and the chamber and of the gas inside the chamber itself respectively.

tubing between XV-2 and XV-3 with the purifier is not cryopumped). In region III, valve XV-1′ (on the chamber) as well as XV-1 are also opened to let some of that xenon flow into the chamber, while XV-7 is closed. If the pressure in the chamber was 1450 Torr during the previous filling, this results in around 350 Torr - 380 Torr of Xe. Following this, the chamber is closed (XV-1′) to test its leakage and electroluminescent light output briefly at low xenon pressures before proceeding. In region IV, the pressure regulator is changed to let increasing amounts of gas into the system to slowly approach the target Baratron-read pressure. Once the pressure is within 50 Torr of the target value, the valve on the chamber is opened again, causing a drop in the Baratron reading (shown by the pressure dip in region V) followed by a final pressure fine tuning to 1450 Torr using the regulator.

As shown above, filling the ELS with Xe, or even raising the pressure in the chamber by just 100 Torr can take a significant amount of time if the pressure is to be set accurately as this requires the regulator to be adjusted very slowly and left to reach a steady state multiple times. On the other hand, cryopumping the xenon back into the cylinder is far quicker. Shown in Figure 21b is the measured pressure over time during a typical Xe recovery. Region I shows the steady state pressure of the gas in the system prior to recovery. Once the xenon gas cylinder is lowered into the liquid nitrogen dewar and cold, valves XV-4, XV-6 and XV-7 are opened, resulting in the pressure drop shown in region II, where the gas between valve XV-1 and XV-7 is recovered in the cylinder. Similarly, regions III and IV represent the recovery of the gas in the tubing between XV-1 and XV-1′ and the gas inside the chamber itself, respectively. The whole cryopumping process takes only a few minutes once the gas tank has been placed into liquid nitrogen. Once the bottom of the Baratron scale reading is reached at around 9 Torr, valve XV-7 is closed. This bottoming out of the Baratron scale is demonstrated by the plateauing behavior of the reading towards the end of region IV. It is worth to note that waiting too long before closing XV-7 can have a detrimental effect and actually increase the pressure of xenon gas in the system if the tank is allowed to warm up. Similar plots can be made for the pressure reading at the Omega transducer, depicting the evolution of the gas pressure at the outlet of the Xe gas cylinder.

3 Instrumentation and Data Taking Methods

3.1 Steel Needle Production

As outlined in section 2.2, two anode needle geometries will be investigated in this work. The copper needle, with a diameter of 6.25 mm had already been machined, gold-plated and installed. The distance between its tip and the photocathode is approximately 14 mm and its tip length (distance along the needle axis from tip to full needle diameter) is 5.5 mm; this results in a tip angle of $\sim 30°$. Given the expectation that the steel needle's field covers a smaller region and is stronger than the gold-plated needle's field near the tip, an anode-cathode separation of 7.5 mm was chosen for the stainless steel needle. Taking into account the depth of the push-on connector shown in Figure 17b and the aforementioned desired distance, the necessary length of the steel needle was calculated to be roughly 52 mm. To machine the needle, a 52 mm long segment was cut from a 0.5 mm diameter stainless steel rod and a disc sander was used to machine the tip; a diagram of the process is shown in Figure 22. The needle was held at its back end with one hand and rotated in the direction opposite to the disc sander's rotation in order to obtain a tip that is symmetric along the needle's axis. To produce a tip that is as sharp as possible, the

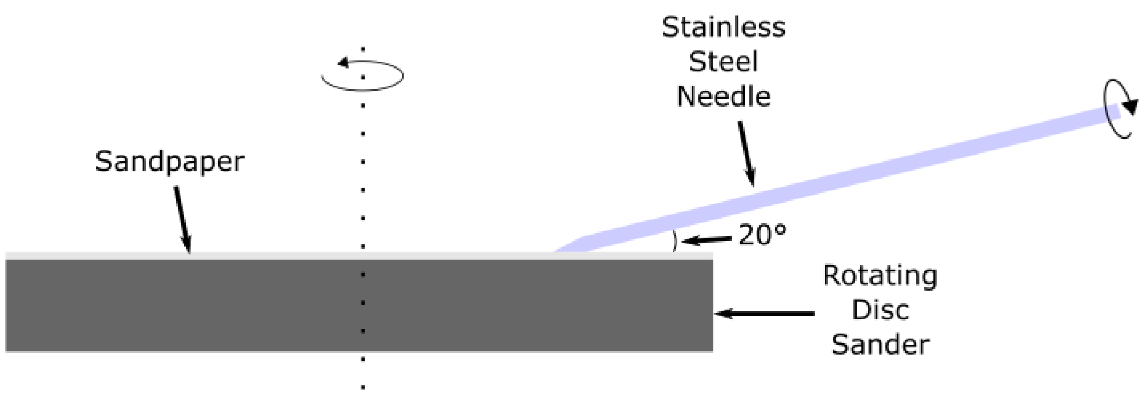

Figure 22: Diagram of the machining process for the stainless steel needle. Shown are the rotating disc sander and thin sandpaper as well as the needle itself and the approximate angle of contact with the sand-paper.

angle between the sand paper and the needle was kept as small as possible, at approximately 20 ° (smaller angles were not really possible due to the sander's design). However, the needle was quite flexible and would easily bend; most notably due to friction with the rotating sandpaper and from the downward pressure applied to keep it in contact with the former. To prevent this bending which undesirably alters the angle between the tip and the sandpaper, very gentle finger nail pressure was applied with the other hand near the needle tip. The quality of the needle tip was monitored by regularly observing it under an optical microscope until no change in the sharpness was noticed. The final tip length of the stainless steel needle is $\sim$ 0.8 mm.

3.2 Pressure Measuring Devices, RGA, and the Pump Stand

As outlined in section 2.3, there are three pressure gauges in the gas handling system responsible for the determination of pressures at various points. A Pfeiffer PKR361 vacuum gauge is installed on a 2.75″ CF cross and powered by the turbo pump controller; its measurement range is between 7.5×10^{-10} - 750 Torr. It is connected to the Display Control Unit (DCU) of the Pfeiffer pump stand. Information about the current pressure measured by the PKR361 vacuum gauge can be viewed on the pump stand's display control unit as shown in Figure 23. Note how the pressure measured is displayed in units of hPA. It is not possible to change this default setting; the conversion factor is $\sim$0.750 Torr/hPa.

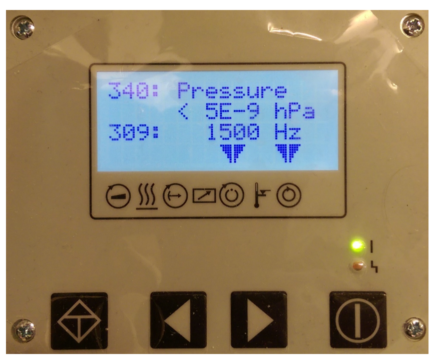

Figure 23: Pfeiffer pump stand display control unit. The display can output the state of two parameters at once. In this case the pressure measured by the PKR361 and the rotation frequency of the turbo pump are displayed. The buttons on the DCU can be used to navigate, monitor and change the different parameters of the pump stand, such as the drive current, turbo pump power, backing pump operation mode and more.

The MKS 722B Baratron absolute pressure transducer is sensitive to a range of pressures ranging from 1 - 10,000 Torr and is used as an approximate measurement of the pressure in the chamber. The Omega PX309 has a dynamic gauge pressure range of 0 - 1000 psi and is used to monitor the Xe pressure inside the xenon gas cylinder. Both the Baratron and Omega are powered using a 15 V DC power supply and they output 0 - 10 V and 0 - 5 V signals, respectively. The Omega and the Baratron's voltage outputs are connected to LabJack analog input channels, through which they are read then converted to pressure values. The output voltage of both devices scales linearly with the pressure they measure, and the following two equations, where P stands for pressure and V for the voltage output, are used to convert their voltage reading into pressure [99,100]:

$$P_{Baratron} = \frac{10,000\text{Torr}}{10\text{V} - 0\text{V}} \times V_{Baratron} = \frac{1,000\text{Torr}}{\text{V}} \times V_{Baratron}. \tag{14}$$

$$P_{Omega} = P_{Ambient} + \frac{51,754\text{Torr} - P_{Ambient}}{5\text{V} - 0\text{V}} \times V_{Omega}. \tag{15}$$

The constant $P_{Ambient}$ offset in equation 15 is present because the Omega measures gauge pressure, i.e. relative to atmospheric pressure. Python code queries the LabJack periodically for the voltage values at the relevant input channels and converts the voltage to pressure, creating a live time trace on a GUI made with the Spinmob package [101]. The data can also be saved for future analysis and plotting; Figures 21a and 21b were produced with data acquired through the LabJack. As the gas handling system is designed with VCR tubing and fittings, its ability to reach high vacuum levels is reliant on the leak-tightness of the of the junctions made by sandwiching stainless-steel VCR gaskets between male and female VCR fittings. Good leak-tightness is achieved by tightening the male-female junction enough to deform the gasket and create a leak-tight metal to metal junction. This permanent deformation of the gaskets makes them unsuitable for repeated usage. Thus, when modifications are made to the inside of the chamber, or when the gas handling system is disconnected, the stainless-steel VCR gaskets on the connections that were opened must be replaced. If done properly this usually guarantees that no major leaks will be present; a clear sign of the contrary is when the PKR361 gauge's reading never drops below 10^{-5} Torr. This is usually a sign that one of the VCR junctions has not been tightened enough and is resolved fairy simply. The female VCR fittings feature small holes as shown in Figure 24; to detect which of the junctions is leaking, ethanol is sprayed into the hole and as it evaporates inside the tubing the pressure reading on the PKR361 will spike.

Figure 24: Male-female VCR junction with leak checking hole. When leak checking, He gas or ethanol is sprayed into every single junction whose gasket has been changed.

While this is enough to detect large leaks, it is not the only leak checking technique employed. Once the pressure drops below 10^{-6} Torr, a SRS200 (Stanford Research Systems) residual gas analyzer coupled with helium gas is used to eliminate smaller leaks if they are present. The RGA is essentially a mass spectrometer that uses electrons emitted from a metal filament to fragment compounds in a low pressure gas into different ions and by measuring their mass-to-charge ratios it is possible to determine what compounds are present in the gas [102]. The analyzer is interfaced with an RGA software provided by SRS [103]. The RGA's filament is "turned on" and left to heat for a few minutes before any scans or leak checking is performed. In the "on" state, a current is applied to the filament, heating it up and causing it to release electrons; it is also subjected to a negative bias in order to repel and accelerate these electrons away. However, when the filament is being initially heated, it not only emits electrons but also metal particles in non-negligible amounts causing the internal pressure of the gas handling system to temporarily rise to 10^{-7} Torr. The composition of the gas in the tubing during pump down should be mainly atmospheric air and water vapour (compounds of 42 AMU and below). Nevertheless, the outgassing of metals does not influence nor interfere with the helium leak checking where the quadrupole in the RGA is set to only detect He ions. He gas is flushed into the leak checking holes shown in Figure 24 while the RGA software is used to set the gas analyzer to monitor helium levels as a function of time. The helium leak checker is held at each junction for about 30 s and the RGA reading is monitored. A steady increase in the helium level reading indicates that the junction being tested is leaking and it is tightened further until the leak is eliminated.

As described in the caption of Figure 23, the Pfeiffer DCU is also used to control the pump stand. Despite being simple to operate on top of requiring very little adjustment compared to other components of the gas handling system, the pump stand still has its share of details worth mentioning. For one, unlike some backing and turbo pump systems in which the turbo pump should not be turned on until the pressure is lower than some value (often around 1-2 Torr [104]), the turbo pump of the Pfeiffer pump stand can be turned on simultaneously as the backing pump, and both can start pumping down from atmospheric pressure. This is possible because the pump stand adjusts the current supplied to the turbo pump and gradually increases the rotor rotation frequency as pressure decreases while keeping it low enough to avoid damage to the pump. However, it is paramount to avoid opening tubing segments that are at high pressures relative to the one near the pump inlet (measured by the PKR361 gauge) when the turbo pump is rotating at high frequencies. This sudden denser volume of gas being sucked into the turbo pump could damage the rotors. If an unpumped segment of the gas handling system is to be brought to vacuum, the turbo pump must manually be turned off and it is recommended to wait for its rotation frequency (1500 Hz maximum as shown in Figure 23) to drop to the low 100's before any additional segments are opened. It is also possible to monitor the drive current supplied to the turbo pump. The drive current supplied to the turbo pump at nominal operation when it has reached maximum rotation frequency is $\sim$0.8 A. However, when the rotors are accelerating, or when there is a leak, the drive current is normally between 1 A - 3 A. Thus, if the pump's rotors have reached their maximal rotation frequency of 1.5 kHz, but the drive current is 1 A or higher, it is usually an indication of a leak in the system.

3.3 Methods and Apparatuses for Charge Collection

3.3.1 Charge Collection Overview

As explained in section 2.1, a key concept in this experiment is the ability to produce photoelectrons on a silver photocathode and accelerate them through the gas xenon. Thus, the ability to actually create and attract charge is arguably the most important part of the 172 nm VUV photon production process. For this reason charge measurements are done in vacuum to ensure proper collection and function of the photocathode and anode. It is especially important to do them when the anode needle has been changed in order to verify that the new geometry can collect charge at all and catch any possible shorting in the chamber before it is filled with Xe.

For charge collection measurements, only the xenon flash lamp is used and not the LED. Carrying significantly less energy per pulse, the LED produces a much lower number of photoelectrons and since the goal here is merely to test charge collection and see how it evolves as the anode bias changes the light source that produces the largest signal on the charge sensitive pre-amplifier is chosen. The charge collection measurements are performed with and without a 265 nm bandpass filter in front of the flash lamp in order to have two sources of confirmation for the trend of the charge signal as the bias is varied. These filter and filterless measurements are also done to ensure that photoelectrons are being produced by 265 nm photons hitting the photocathode and not just surfaces like the chamber's walls.

3.3.2 The Xenon Flash Lamp

As with typical xenon flash lamps, the Hamamatsu L11035 xenon flash lamp used for the ELS uses a volume of xenon gas with a high voltage trigger and a pair of electrodes connected to a capacitor. The trigger creates a spark inside the gas which prompts a discharge of the capacitor through the electrodes; this current ionizes the gas and leads to a flash of light. The Hamamatsu lamp is operated through a conjunction of DC power supply and signal generator. The former is used to power the flash lamp and is required to apply a bias of 11 V at a maximum current limit of 1 A. The signal generator is used as a trigger to control the light pulsing frequency. The lamp, whose pulse width is fixed, requires a bias of 5 V to be applied for at least 10 μs in order to turn on. It uses one of two modes to control the voltage applied across the capacitor (400-600 V) and thus the energy released by its discharge; the "internal" and "external" modes selected via a designated switch on the lamp shown in Figure 25. In the former, a trimmer potentiometer located next to the switch can be adjusted to vary the capacitor bias and thus the intensity of the lamp's emitted light pulses. In the latter, this bias is controlled by supplying an external voltage between 3.2-4.8 V. For the charge collection measurements, a 50% duty cycle square wave at 200 Hz is sent from the signal generator to control the frequency of the light pulsing, and in order to obtain the most intense light pulses, the internal mode is used with the potentiometer set to maximum.

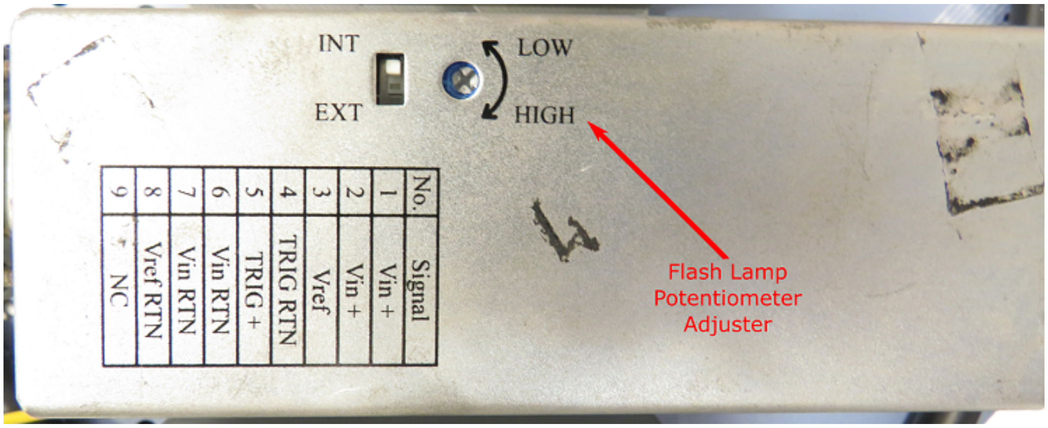

Figure 25: Labeled is the trimmer potentiometer used to adjust the charge stored in the lamp capacitor and therefore the intensity of the light pulses when the lamp is set to internal discharge mode. Next to it is the switch used to change between the discharge modes as well as a table for the required connections to each pin on the lamp's connector.

3.3.3 The Charge Sensitive Preamplifier

The preamplifier used for the charge collection measurements is the Cremat CR-Z-110-HV. The CSP not only features a port to read out the charge collected on the anode, but also a port connected to an external power supply used to bias the anode. When a charge cloud is produced at the photocathode and collected at the anode, the charge is integrated by the CSP and an output pulse with peak height proportional to said charge is measured at the CSP's output. Figures 26a and 26b show the input and output ports of the CSP as well as a simplified diagram of its circuit, respectively. The CSP's gain is 1.4 V/pC, i.e. 1 pico-Coulomb of charge collected by the anode will result in a pulse whose peak height is 1.4 V. The maximum bias that can be applied to the anode using the CSP is ± 2 kV, and while the CSP could be used to collect charge while the PMT simultaneously collects light, the range of positive bias values applied on the anode during light measurements goes well above 2 kV. Given this limitation, it is only used for charge collection measurements done in vacuum, where a few hundreds of volts are enough to saturate the CSP's output range of $\sim \pm 3$ V. The charge integration is done by a feedback capacitor (C_f=1.4 pF) in the CR-110 module labelled in Figure 26b; this capacitor discharges through the feedback

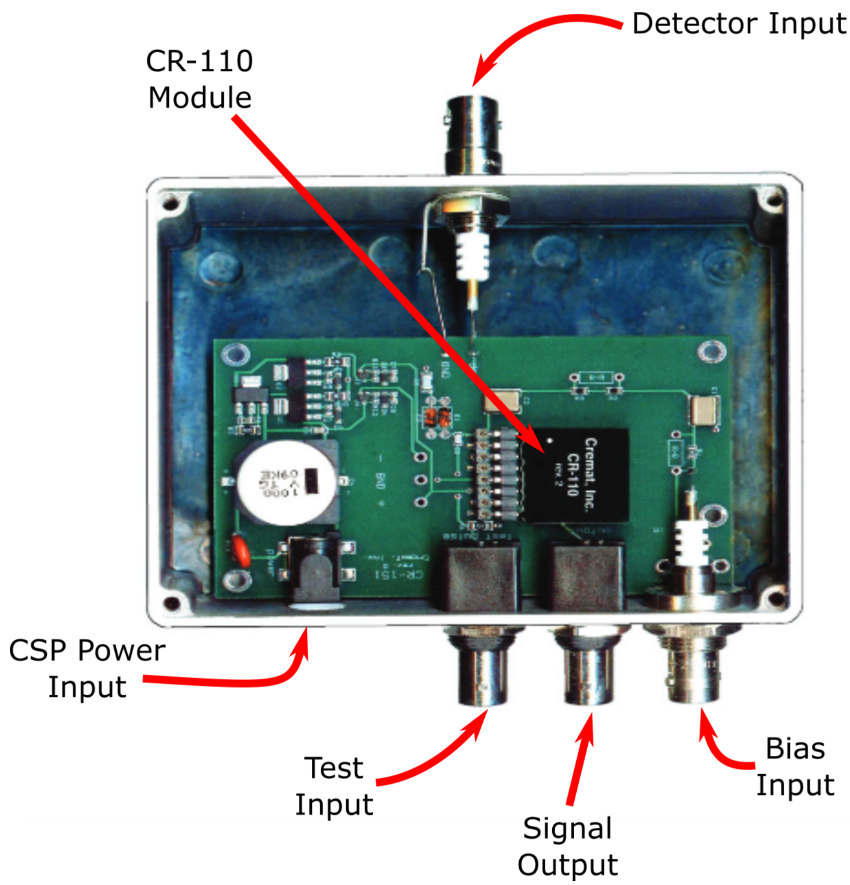

(a) Main input/output ports of the Cremat CSP.

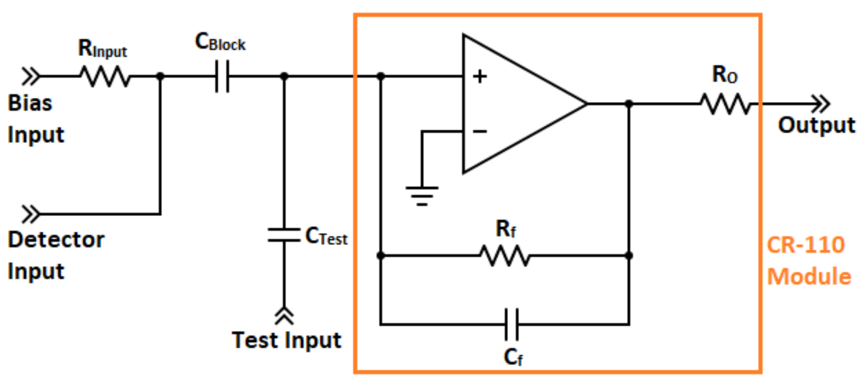

(b) Simplified circuit diagram of the CSP.

Figure 26: a) Picture of the CSP along with the ports used to for input and output. The input to bias the anode is SHV and the internal circuitry of the CSP allows biases up to ± 2 kV. b) Circuit schematic. The CR-110 Module integrates the charge using feedback capacitor C_f; the latter discharges through the feedback resistor R_f resulting in an exponential decay of the output voltage peak. The test input can be used to test the CR-110 module and the CSP's output.

resistor (R_f=100 MΩ) and produces a decaying pulse. The rise time of the pulse is around 7 ns while the decay time is given by $\tau = R_f C_f$ =140 μs. The CSP also features a test input port with a 1 pF capacitor (C_{Test}); a square wave can be applied to simulate an incoming charge signal and verify the gain or decay time of the CSP. The resistor R_{Input} is a 200 MΩ resistor that prevents any charge collected at the anode from going to the anode bias input and instead through the lower impedance of the 0.01 μF blocking capacitor (C_{Block}). Likewise, this capacitor also prevents any DC bias applied to the needle from affecting the CR-110 module and the output.

3.3.4 Setup and Methodology for Charge Collection Measurements

In this section, more specific steps for the procedure will be provided as well as an explanation of the experimental setup. The hardware layout inside the dark box as well as a diagram of the full experimental setup for charge measurements are shown in Figures 27a and 27b, respectively. Charge collection measurements are always performed either after changes are done to the inside of the chamber or when the experiment has undergone a period of inactivity to test if electrons can be accelerated to the anode at all in vacuum before doing so in gas xenon.

Given two different needle geometries are being investigated in this thesis, there are two sets of voltage ranges used to bias the anodes. For the thin stainless steel needle discussed in section 2.2 it is necessary to go to biases of a few hundred volts in order to saturate the reading, as opposed to only 4 V for the thick gold-plated copper needle when no 265 nm filter is used. However, since the goal for these measurements is merely to verify that charge collection works and that the output increases with increasing positive bias, the bias ranges are not explicitly chosen with the goal to saturate the CSP output. Data is taken at various voltage values within the bias ranges shown in Table 1 for each geometry. For data acquisition, a python script that heavily uses the functionalities of the

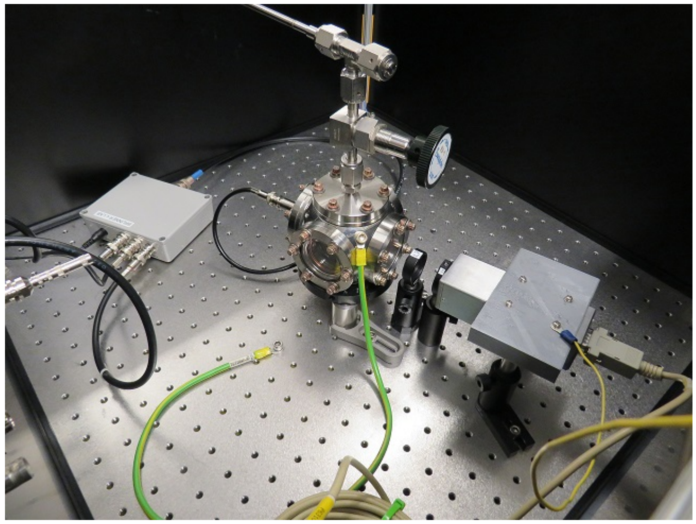

(a) CSP, ELS Chamber and Flash Lamp in Dark Box.

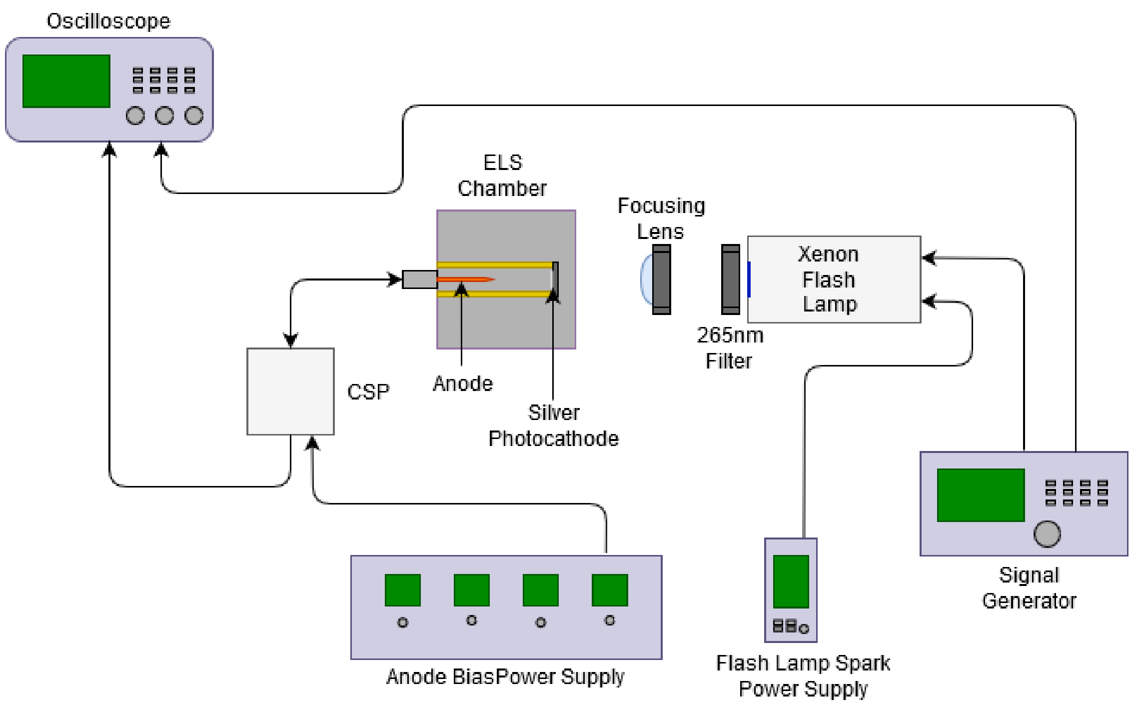

(b) Diagram of the Full Charge Collection Setup.

Figure 27: In a) is shown the inside of the dark box during charge measurements; a thick black blanket (not shown) is used to cover the chamber and lamp to prevent light from scattering off the inner panels. In b) is a diagram of the whole charge measurement setup including all the electronics and the signals that play a role in the measurement.

	Stainless Steel Needle	Gold-Plated Needle
No Filter	-100 V to +200 V	-30 V to +4 V
With 265 nm Filter	-100 V to +250 V	-30 V to +30 V

Table 1: Bias ranges for charge collecting measurements for the two needle geometries.

Spinmob package (see [101]) was written to query the scope and pull the voltage time traces before saving them into csv files. An example a single trace on the oscilloscope's screen can be seen in Figure 28. Note that in this Figure the anode bias which is 50 V has

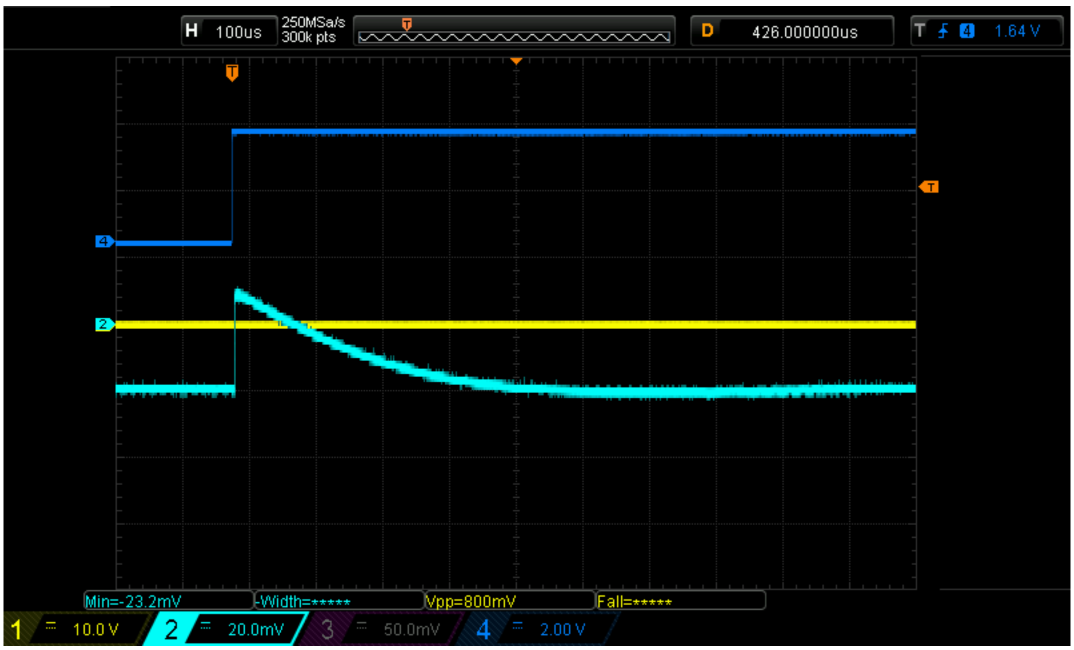

Figure 28: Example of data traces on the oscilloscope for the CSP output pulse (light blue ch. 2) and the Xe Flash Lamp trigger square wave (dark blue ch. 4). In this example, the bias applied to the anode is 50 V which results in a positive peak. For negative biases, where electrons are being emitted from the anode needle rather than collected, the peak has a negative amplitude. This negative amplitude plateaus in magnitude relatively quickly in the negative bias region.

not been Tee'd off to the oscilloscope, hence channel 1 measures 0 V. The light blue trace (channel 2) represents the CSP output pulse and the darker blue trace (channel 4) measures the square wave synchronized to the xenon lamp trigger. The saved raw data traces can then be fitted to extract the amplitude and plotted against bias to see the evolution of the collected photoelectron signal. If the data shows a consistent increase in the collected charge with increasing positive bias and there are no obvious problems, the next step is to proceed with light measurements for the geometry in question. Recorded charge data will be presented and discussed in section 4.1 for both anode geometries.

3.4 Methods and Apparatuses for Light Measurement

3.4.1 Electroluminescent Light Measurements Overview

As per the title of this thesis, the goal of the electroluminescent light source is to produce controlled pulses of 172 nm light to be used for SiPM testing for nEXO. This work describes the very first results of successful electroluminescent light production. In section 3.3, it was discussed how the Xe flash lamp allows for large amounts of input light to enter the ELS Chamber and thus produce a large number of photoelectrons off the silver photocathode. It might seem like it is also a good 265 nm controlled light source to use for the production of VUV photons; however, its relatively long pulse width (~200 ns [86]) produces electroluminescent pulses whose pulse width is around ~400 ns. Given the target pulse widths discussed in section 2.1, a controlled UV light source with a shorter pulse width such as the Thorlabs M265L3 LED which can emit pulses as short as 20 ns is required. A Photomultiplier tube is used to collect the VUV photons produced as well as the leakage 265 nm light pulse of which it triggers; the data acquisition of the signal from the PMT is done via digitizer for the steel needle instead of the oscilloscope. The digitizer can trigger and read data at rates of up to 7 kHz, allowing for large numbers of triggers to be acquired in short time.

3.4.2 Focusing and Driving the Thorlabs 265 nm UV LED

The Thorlabs M265L3 is a 10 mW LED with an spectral emission spectrum width of 11 nm and an emission cone of 130 °. As the LED already emits wavelengths centered narrowly around 265 nm, there is no need for a bandpass filter. Instead, a system of 2 lenses shown in Figure 14a is used to collimate and focus the LED light into a narrow spot. This was done with two goals in mind. The first being to increase the overall amount of photons impinging at the photocathode and also focus them to the center of the photocathode. The second was to reduce leakage into the PMT by redirecting light that would otherwise reflect into the chamber via the sides of the cathode holder. Focusing most photons to impinge at the center of the photocathode is beneficial if short electroluminescence pulse widths are desired since more localized photoelectron emission near the cathode center results in lesser differences in drift time to the anode.

To achieve nanosecond scale input pulses, the combination of a Keysight 33500B signal generator [105] and an ENI 325LA RF amplifier [106] is used. The LED's turn-on voltage is stated as a minimum of 6.8 V; however, this is for continuous operation. In the case of a short nanosecond pulse with this amplitude, the light intensity emitted by the LED is far too little to measure an EL signal on the PMT. Thus, the RF amplifier is used to increase the voltage applied to the LED to much greater values. Tests performed on the UV LED have shown that it can be biased with voltages over 70 V for ns-scale time periods to produce intense pulses and still operate for extended periods of time without suffering damage. The signal generator is used to set the width of the voltage pulse, an amplitude and a repetition frequency. This signal is then input to an RF amplifier and sent to the LED with an amplitude around 3 orders of magnitude higher. The only parameter that is changed is the pulse width, as measurements are taken at 80 ns and 160 ns input pulse widths. The signal generator's output square pulse has a height of 75 mVpp and the repetition frequency is 45 kHz. This results in LED pulses being released every 22 μs; the leakage from the LED and the EL pulse can both be captured in a 2.5 μs digitizes window meaning there is no potential overlap of a 172 nm pulse with a leakage pulse from the next LED flash.

3.4.3 Photomultiplier Tube and Digitizer

To measure the 172 nm photons produced in the ELS a Hamamatsu R6834 photomultiplier tube [107] is placed at the front of a MgF_2 viewport. A photomulitplier tube (shown in Figure 14b, next to the chamber, and Figure 29 [107]) is an apparatus that uses a photocathode to emit photoelectrons and cascade them down a series of dynodes, effectively multiplying them to create a measurable current when they arrive at the anode. The Hamamatsu PMT uses the "box and grid" geometry for its photocathode-dynodes-anode arrangement which is illustrated in Figure 29. A voltage control box is used to apply a

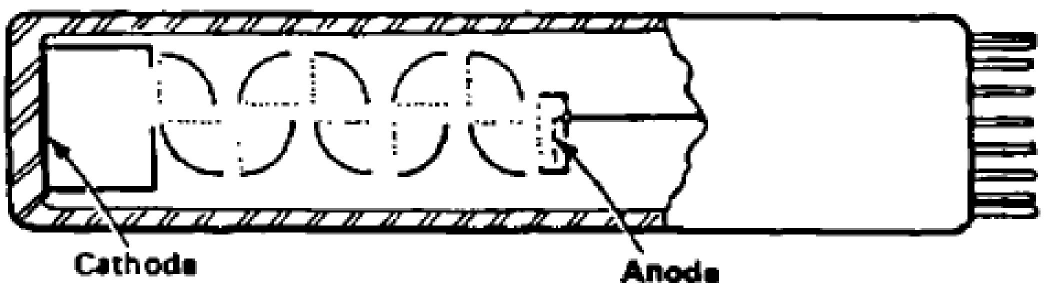

Figure 29: Schematic of the box and grid geometry for a PMT. Photoelectrons are emitted when a photon strike the cathode and are attracted to a series of dynodes, each at progressively higher bias than the previous one. When an electron strikes a dynode, the energy transfer liberates secondary electrons creating a cascade, a process which greatly multiplies the e^- to form a measurable current collected at the anode. This electron multiplication process allows PMTs to commonly reach gains of $10^5 - 10^6$ [56].

bias from 0 to 6 volts to the PMT base which gets internally multiplied by 250 for a maximum of 1.5 kV between the anode and photocathode. There are 11 multiplication stages, corresponding to the number of dynodes, and voltage dividers hold each two consecutive dynodes at equal potential difference of $V_{bias}/12$; where V_{bias} is the voltage between the anode and photocathode; it is divided by 12 to account for each multiplication stage plus the anode which also needs to be biased to collect the electrons. The PMT bias can be adjusted across a wide range of values; however, given how the gain of the PMT is directly proportional to the potential difference between two consecutive anodes, too low bias could mean not enough amplification of the photoelectron signal to be measurable. Too high bias is also undesirable since this increases the dark count rate and risks damaging the PMT if the current at the anode is too high. Generally, voltage values of photon pulses measured on the PMT output are to be kept below 1 V given the input range of the digitizer discussed below; for the ELS a bias of typically 4.5 V (1125 V between anode and cathode) is used, resulting in LED leakage pulse heights of just over 200 mV while keeping the noise acceptably low for the smaller ELS pulse. Additionally, as mentioned in section 2.1, 172 nm light is absorbed across very short distances in air due to the presence of oxygen; this is mitigated by continuously purging the volume between the PMT photocathode and the magnesium fluoride window with nitrogen gas.

A CAEN DT5730 digitizer (see [108]) is used for rapid data acquisition of the light signal measured by the PMT. It is a 14-bit digitizer with a 250 MHz bandwidth, sampling rate of 500 MS/s and an input voltage range between -1 V and +1 V using an ADC converter to transform voltage values into bit representation. The voltage resolution of the digitizer is given by its full voltage range divided by the number of discrete voltage intervals and is equal to 2 V/$2^{14} = 1.22 \times 10^{-4}$ V. The digitizer samples voltage values from the PMT every 2 nanoseconds and for light measurements the number of samples for one trigger is set to 1270, resulting in a raw data time trace of 2.5 μs duration. The CAEN DT5730 is operated using a GUI written in C++ to optimize data transfer speed, allowing it to save data at rates up to $\sim$7 kHz. All the data acquisition parameters such as the trigger channel, the trigger level, the number of samples to be saved per trigger, the % of samples in the post-trigger window, etc. can be configured with the GUI. Moreover, is it possible to plot triggers and monitor what the saved data looks like in real time as the GUI can plot the latest trigger at fixed time intervals set by the user. A trigger of a leakage pulse and no electroluminescence light obtained using this plotting function is shown in Figure 30 below. Combined with the ability to zoom in on specific ADC voltage or sample ranges,

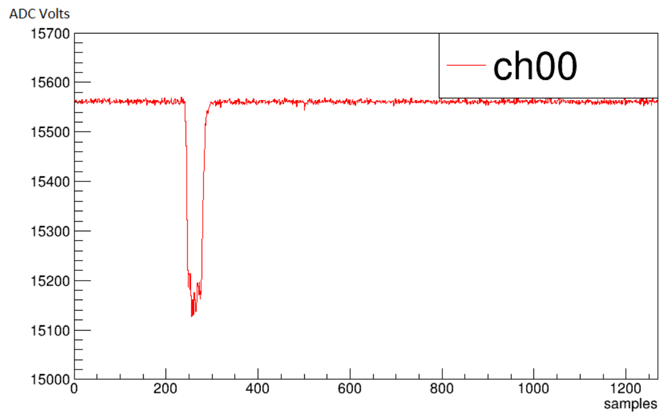

Figure 30: Raw data for a single trigger of an 80 ns LED leakage pulse on the digitizer GUI. The y-axis represents the ADC Voltage and the x-axis the time samples, where the time difference between two time samples is 2 ns.

this is as effective as observing the signal in real time on an oscilloscope. For analysis, the baseline of each trigger is determined and subtracted (in Figure 30 this value is roughly 15560 ADC volts) and the ADC Voltage values can be converted back to volts knowing the full voltage scale and the digitizer's resolution in bits. Converting the time axis is simply a multiplication of each sample number by 2 ns / sample. Unlike for charge measurements where the acquisition and analysis code is written in Python, all the code for the digitizer is written in C++. This not only speeds up data acquisition but also lends itself naturally to the usage of the Root scientific toolkit developed for CERN [109]. Root allows for the raw data to be saved in highly compressed files, significantly lowering the storage load. The toolkit can also be used during analysis to extract and calculate properties of interest. For plotting and fitting, Uproot is used to import the analyzed data files in python [110].

3.4.4 Setup and Methodology for Light Measurements

The procedure for light collection measurements is much alike the one for the charge counterpart. The difference being that the PMT, LED and digitizer are used instead of the oscilloscope for DAQ. Unlike for charge data measurements, there are also significantly more parameters to vary for electroluminescence light detection. As outlined in section

3.4.2, measurements are performed at two different LED pulse durations, namely 80 ns and 160 ns. Since the evolution of the electroluminescence light as a function of anode bias is one of the target measurements, a high voltage power supply is used to take data in intervals of 100 V starting at 900 V and ending either when the bias is high enough to cause a breakdown in xenon gas or, for the stainless steel needle specifically, when it reaches $\sim$2.8 kV, where the electrical noise on the PMT baseline signal is noticed to increase significantly for a reason not well understood. Many of the pressures at which measurements are taken with the stainless steel anode require biases higher than 2.8 kV to induce gas breakdown; yet, the PMT signal still deteriorates when the anode bias reaches 2.8 kV. Note that this deterioration is not observed with the gold-plated needle, where the bias is increased to 4 kV without issues.

Before any measurements are taken, the xenon pressure in the chamber is adjusted to the target value after which the chamber valve is closed. All electronics can then be configured and a few test runs can be performed by triggering off leakage pulses to make sure everything works normally. Note that it is imperative to keep the box closed while the PMT is being biased. Ambient light exposure may cause damage to the PMT; thus whenever light data is being taken, the clamps on the box lid are closed. The main components of the light setup were previously shown inside the dark box in Figures 14a and 14b; Figure 31 is a detailed diagram of the whole light collection setup.

Once all the electronics are tested and the PMT can detect leakage, the bias on the anode is incremented. Around 100,000 triggers are taken at every bias voltage for every one of the aforementioned pulse widths, at every pressure. Once this is complete for a specific pressure, an extra $\sim$100 Torr of xenon is added to the chamber and the same measurements are performed for pressures up to 1450 Torr.

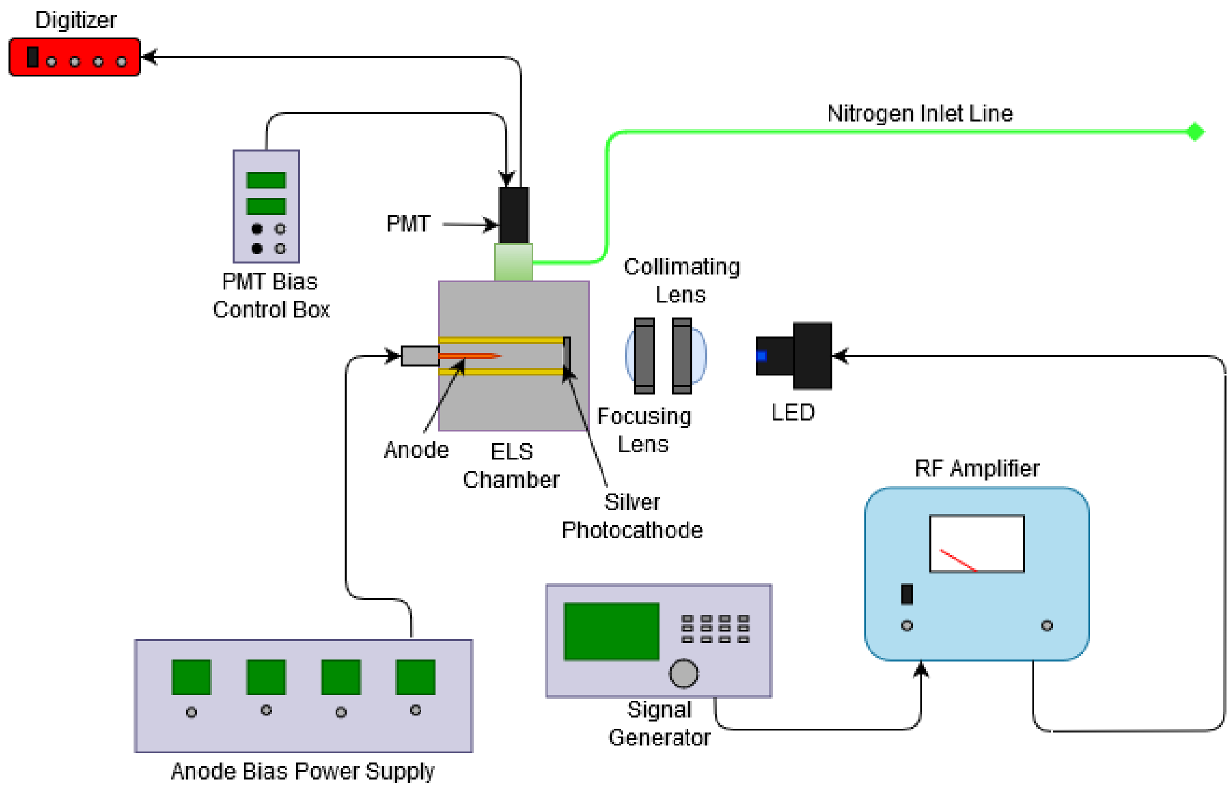

Figure 31: A diagram of all the components involved in producing and measuring electroluminescent light pulses. Illustrated are also all the signals involved in the measurement as well as the nitrogen inlet line to purge the volume of air between the MgF_2 window and the face of the PMT.

4 Data and Results

4.1 Charge Data Measurements

4.1.1 Gold-Plated Copper Needle Charge Measurements

As mentioned in section 2.2, in its initial design, the ELS used a copper anode needle which was later gold-plated to reduce its photoelectron emission. As this needle geometry was the first available, charge and light measurements were attempted with it before changing to the stainless steel needle. These charge measurements were primarily done to verify the charge production and collection capabilities of the ELS, which had undergone a long period of inactivity. However, they also resolved an uncertainty about the CSP's behavior when it came to the polarity of the bias it applies to the needle. Measurements taken by previous students in 2018 (see [79]) observed pulses where the magnitude of the amplitudes grew larger with increasing bias regardless of its polarity. As the amplitude is only expected to increase with increasing positive voltage, their measurements led them to question whether the CSP was perhaps inverting the polarity of the input bias.

It was previously described in section 3.3.4 how charge measurements were performed and Figure 28 shows a single waveform of the CSP output. For charge data, 200 raw waveforms are saved from the oscilloscope for various anode biases in the ranges given in Table1 depending on the needle and presence of 265 nm filter. The Rigol 1074Z has a 2-3 Hz acquisition rate (despite the Xe lamp flashing at 100 Hz); additionally, it has an 8 bit resolution for its vertical axis. As such, changing its vertical scale impacts its voltage resolution. Thus, in order to maximize the voltage resolution of recorded waveforms for every single bias, a test measurement had to be done beforehand to determine the optimal vertical scale and offset by hand. Additionally, when a change in bias occurs there is a period of 30-45 s for the charge signal baseline to settle. This ultimately led to the whole acquisition process (including vertical scale/offset and anode bias change) being automated for the sake of convenience. Shown in Figure 32 is a plot of the CSP signal evolution as a function of anode bias for the gold-plated needle with no 265 nm filter in front of the flash lamp. Each time trace is the result of 200 averaged waveforms. There is a noticeable evolution of the pulse amplitude as increasing positive biases are applied. To obtain a more precise measure of the amplitudes of these CSP pulse they are fitted to the convolution of an exponential and Gaussian distribution function shown below:

$$V(t) = \int_{\Delta T - 10\sigma}^{t} \frac{A}{\sqrt{2\pi\sigma^2}} e^{-\frac{t-t'}{\tau}} e^{-\frac{(\Delta T - t')}{2\sigma^2}} dt'. \tag{16}$$

This function was chosen to encompass both the exponentially decaying behavior of the pulse as well as the fast ns-scale rise time of the CSP signal (see [90]). As seen from the

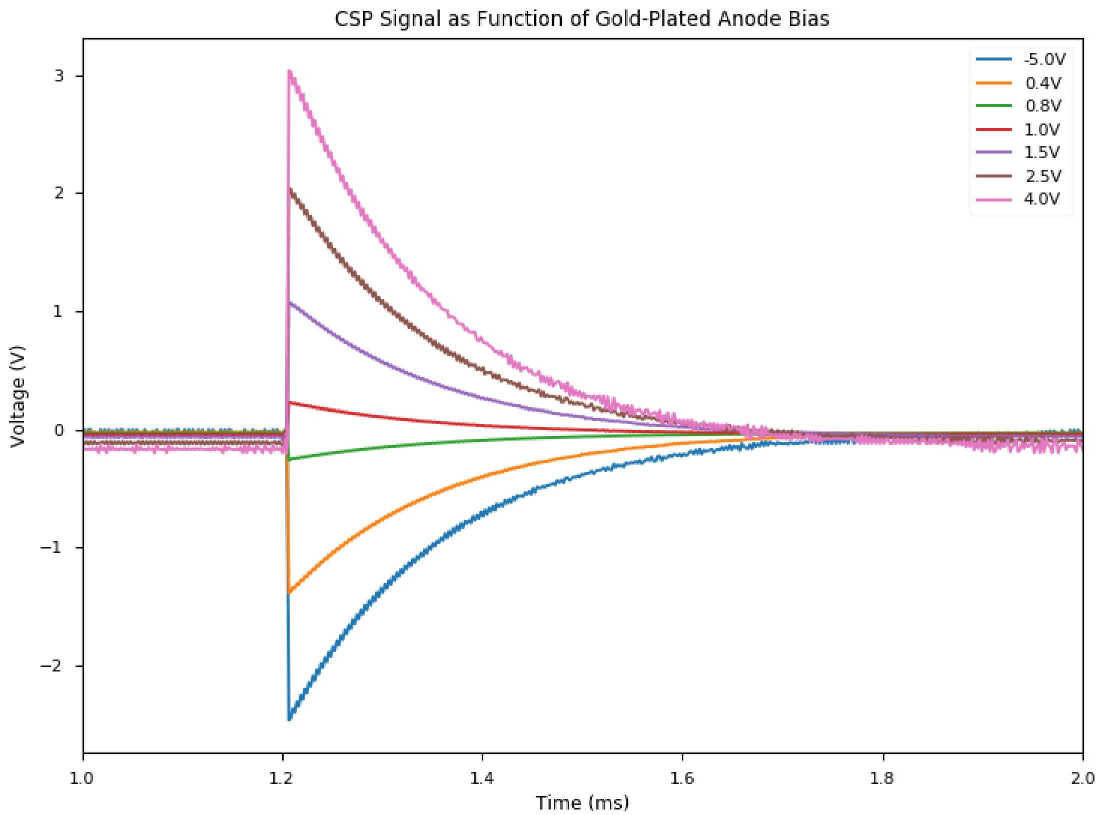

Figure 32: Averaged 200 raw data pulses per bias from the CSP for a variety of biases with the Xe flash lamp and no filter. Note how the amplitude at 0.4 V bias is negative despite the positive polarity of the applied bias. This is a sign of net photoelectron emission from the anode which is overcome by applying higher voltages.

raw averaged data traces in Figure 32, there is a time period of $\sim$1.2 μs before the sharp rise of the pulse where no charge is measured at the CSP. Using a very small value of $\sigma \approx 0.01$ μs (which determines the width of the Gaussian) and $\Delta T \approx 1.2$ μs (determining the center of the distribution) results in a Gaussian peak that is extremely narrow, and its product with the exponential is essentially 0 for the time period until $t \approx 1.2$ μs. Once t gets near, and past $t = \Delta T$, the product in the integrand has non-zero contributions which result in the shapes observed in Fig. 32. A narrow Gaussian results in a short rise-time to amplitude A on the rising edge of the pulse; meanwhile, as t increases past the center of the Gaussian, the decaying exponential provides progressively smaller contributions to the integral, resulting in the exponentially decaying tail of the pulse with a time constant

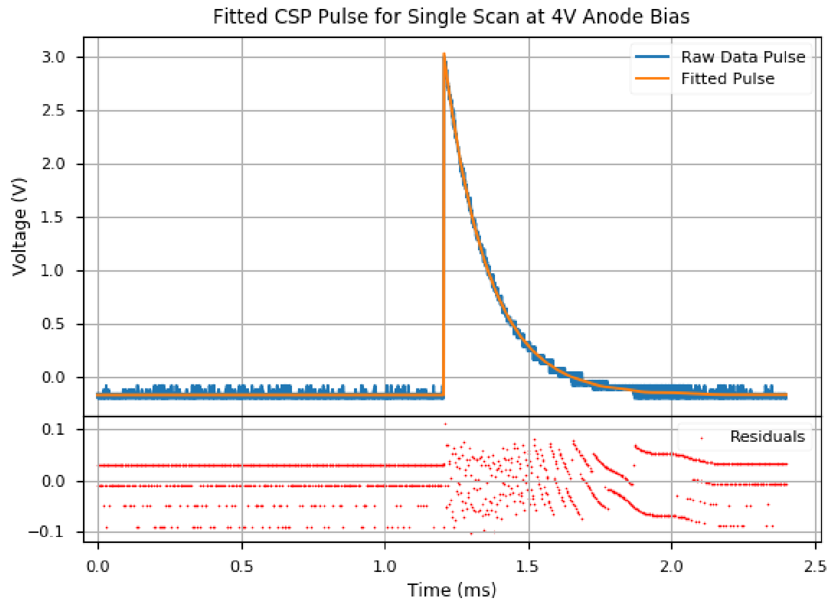

Figure 33: Fit of an individual raw data trace from the charge sensitive preamplifier taken with no filter and +4 V anode bias. The units of the residuals are the same as those for the main plot. Furthermore the residual uncertainties are $\sim$0.06 V but were not included as they cause major clutter given the amount of data points.

$\tau \approx 140\ \mu$s. An example of a single fitted raw pulse is shown in Figure 33. Each of the 200 raw data traces is fitted individually and their parameters and uncertainties are combined. This results in peak height as a function of anode bias which is plotted for the voltages chosen over the different bias ranges. The results for the gold-plated anode are shown in Fig. 34a and 34b for unfiltered and filtered light scans, respectively. Both, filtered and unfiltered scans were initially planned to cover the same range of investigated biases between $\pm$30 V; however, the positive voltages in the unfiltered scans only go to 4 V as the CSP already reaches its maximal output of 3 V. In Figure 34a the error bars on the data points are too small to see with or without plot markers given their magnitude compared to the voltage range spanned by the amplitudes. In the case of the filtered light measurements, the error bars are visible in Figure 34b as their amplitudes span a voltage range 2 orders of magnitude lower. The uncertainty on the amplitude is mainly driven by the noise from the CSP signal as well as the limited oscilloscope resolution. Thus, given

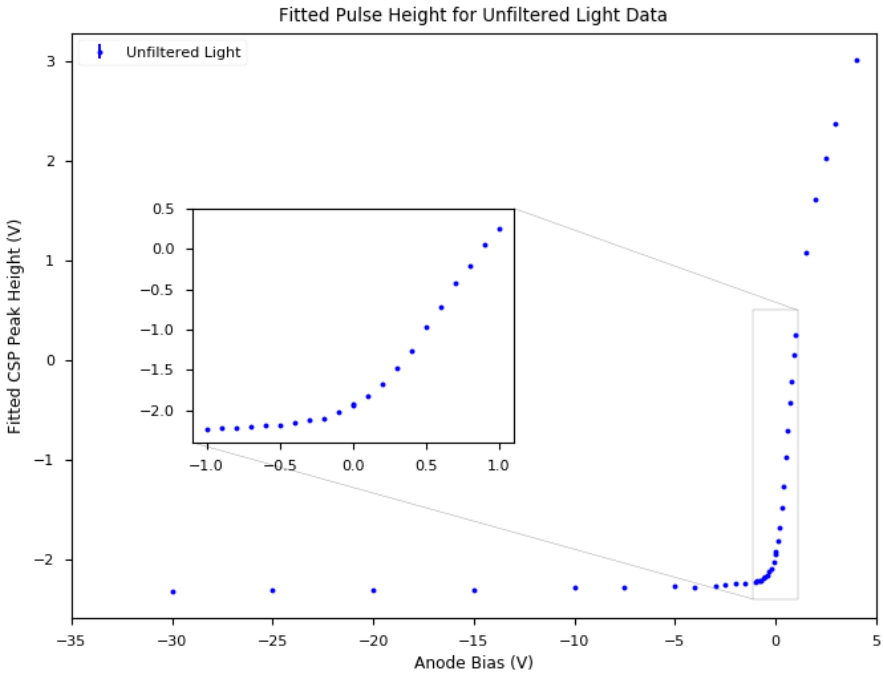

(a) Pulse height vs. anode bias with Xe lamp.

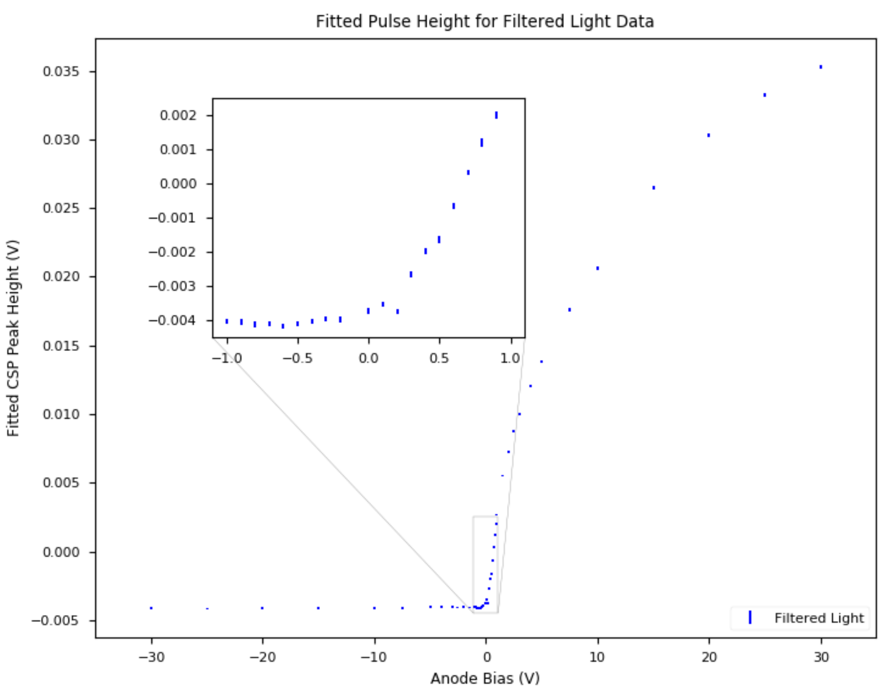

(b) Pulse height vs. anode bias with Xe lamp + 265 nm filter.

Figure 34: In a) is shown the evolution of the pulse height for unfiltered light data as a function of the bias on the gold-plated anode. In b) is the same data shown for filtered light data. The insets show the increased density of data points near the 0 V pulse height crossing. Error bars were determined from the uncertainty in the amplitude fit parameter.

a constant noise from the CSP [90], the lower the signal the larger the noise relative to it; which ultimately leads to larger uncertainties in proportion to the pulse height.

When the Xe flash lamp is off, the CSP signal in vacuum remains at a constant 0 V, as expected since no photoelectrons are being emitted. Despite the gold-coating to reduce p.e. emission from the anode, both plots above clearly show that photoelectron production from the anode still occurs given the negative pulse heights which represent electron emission. This is mainly the case for the unfiltered scans where the wavelengths emitted from the Xe lamp go as low as 185 nm. For this reason, a small positive bias is necessary in order to recapture the electrons emitted from the needle and reach the 0 V signal. This bias value is ~ 0.88 V and ~ 0.67 V for the unfiltered and filtered scans, respectively. At the beginning of this section, the possibility of the CSP inverting the polarity of the input was mentioned based on previous measurements performed in [79]. However, Figures 34a and 34b are consistent with a non-inverting CSP, since the pulse amplitude grows larger with increasing positive bias, due to more photoelectrons collected from the photocathode, while plateauing in the negative bias region. This plateauing behavior is expected to occur at negative biases since the number of p.e. emitted from the anode itself, rather than the photocathode, remains practically constant.

4.1.2 Steel Needle Charge Measurements

Much like for the gold-plated needle, charge collection measurements were repeated with the stainless steel needle using the same methodology, and are shown in Figure 35. The trend for the stainless steel needle charge data is consistent with that established by the gold-plated needle scans; there is an increase in signal at increasing positive biases. However, the overall magnitude of the pulse heights for the steel needle measurements is much smaller. This can be explained by the fact that the field for the thin needle is a lot more restrained around the tip unlike for the larger gold-plated needle whose field extends much further. This impacts the steel needle's ability to attract photoelectrons

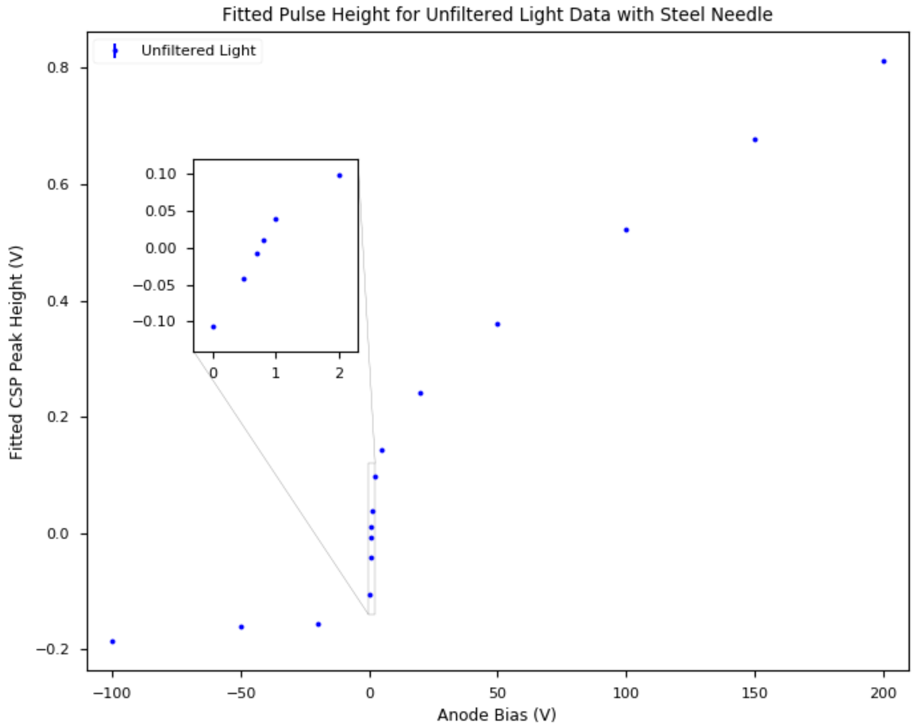

(a) Pulse height vs. anode bias with Xe lamp.

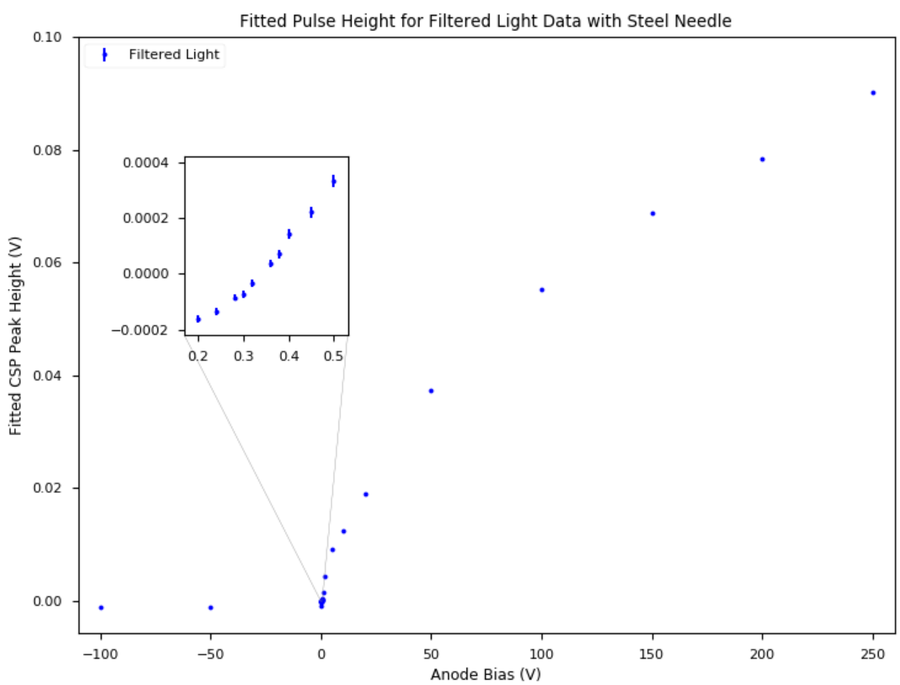

(b) Pulse height vs. anode bias with Xe lamp + 265 nm filter.

Figure 35: In a) is shown the evolution of the pulse height for unfiltered light data as a function of the bias on the stainless steel anode. In b) is the same data recorded with the filtered light source. Both plots feature insets showing the increased density of data points near the 0 V pulse height crossing.

emitted from the walls of the chamber and potentially even those emitted directly from the photocathode if the bias is not strong enough. This phenomenon is directly illustrated in Figure 36 for 2 V, 5 V, 10 V, and 20 V biases.

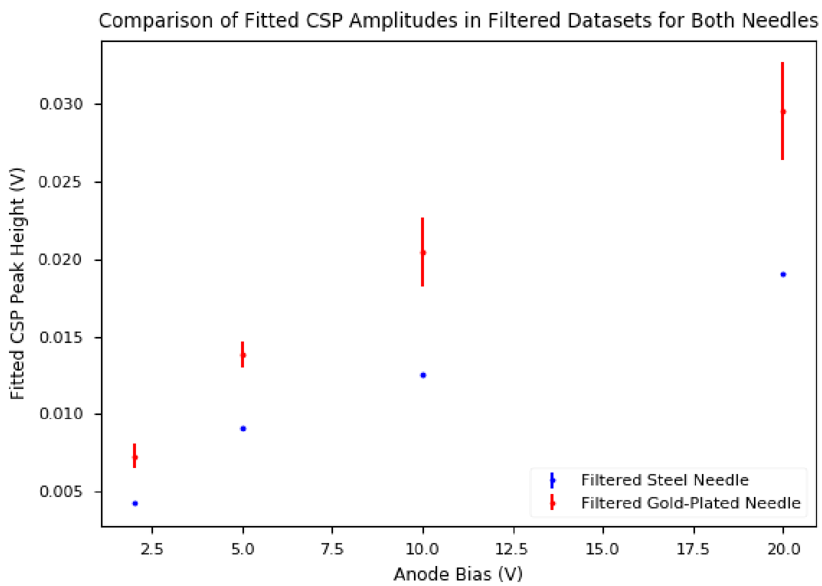

Figure 36: Comparison of charge signals for both needle geometries at various biases. The output for the gold-plated needle measurements was 50 Ω terminated (to reduce noise in that dataset) unlike for the steel needle, which results in the output being halved. This is a good example of the steel needle's very short range field. The Xe flash lamp was kept at the same distance relative to the photocathode for both datasets so the difference is not attributed to difference in incident light flux.

Worth noting is also the fact that the work function of stainless steel is 4.31 eV [87] which makes it susceptible to photoelectron emission from wavelengths as high as 288 nm, implying that even with the 265 nm filter there will still be photons energetic enough to produce photoelectrons from the steel needle. However, since the needle is thin, with a diameter of only 0.5 mm the number of photons that impinge on it is still far smaller than for the gold-plated anode which has a diameter of 6.25 mm. Therefore, the main reason for the steel needle data having a lesser absolute amplitude in the negative bias region is likely due to its geometry.

When looking at the insets in Figures 35a and 35b one would expect the biases needed to reach the 0 V signal to be lower than those in the gold-plated needle scans as the field at the vicinity of the steel anode is stronger. Indeed, the voltage needed for a 0 V signal in the unfiltered data is ~ 0.74 V and ~ 0.34 V for the filtered data. A potential reason for why the first bias cited is not even smaller is due to the lower steel work function especially compared to gold (5.31-5.47 eV [69]). When the filter is present and the wavelength is restricted around 265 nm (4.68 eV), emitted photoelectrons from the steel anode should have energies of at most ~ 0.38 eV which aligns quite well with the bias stated for the filtered scans' 0 V point.

These results confirm the desired characteristics of the ELS's charge production mechanism: consistent amounts of charge produced for each flash, as implied by the small uncertainties of the fitted CSP pulse heights, and increasing number of collected photoelectrons at the anode with increasing positive bias. The specific voltage and CSP amplitude values are not comparable to those in light measurements, as electron transport properties in vacuum and xenon are quite different; nevertheless, these charge collection measurements serve as a good sanity check and demonstrate p.e. production at the photocathode.

4.2 Light Data Measurements

4.2.1 Gold-Plated Copper Needle Light Measurements

The first needle geometry to be investigated is the gold-plated copper needle. This geometry is the very first anode that has been placed in the ELS. The authors of [79, 80] have already attempted measurements of 172 nm electroluminescent photons using the gold-plated needle but to no avail. To verify said past measurements, first tests were conducted at the same pressure of 1450 Torr and at the same bias range below 2 kV. The reason for the 2 kV bias limit stems from the fact that all previous measurements biased the anode through the CSP in the hope of being able to monitor both charge and light; and indeed as shown in [79], charge collection at non-zero gas pressures is feasible. However, at biases lower than 2 kV no electroluminescent light emission was observed with the gold-plated needle; this is most likely because the field generated by a 2 kV bias is too weak. In gas Xe, the reduced electric field (E-field divided by pressure) threshold for the onset of electroluminescence is between 0.8 $\mathrm{kVcm^{-1}bar^{-1}}$ and 1.0 $\mathrm{kVcm^{-1}bar^{-1}}$ according to [84, 111, 112]. In the case of the ELS with the gold-plated needle, as a first order approximation, a 2 kV bias on the anode at a pressure of 1450 Torr (2 bar) and an anode to cathode distance of 1.4 cm, as stated in section 3.1, produces a reduced electric field of approximately 0.7 $\mathrm{kVcm^{-1}bar^{-1}}$, insufficient for EL light emission. Given the fact that 2 kV is the bias limit of the CSP, the latter had to be removed from the system in order to take measurements at stronger electric fields. This resulted in the loss of charge collection and instead the maximum bias that can be applied to the anode is now only limited by the xenon breakdown voltage itself. Following this change, the anode bias was continuously increased until the chamber started sparking which meant Xe gas breakdown was achieved (at $\sim$4.2 kV). Additionally, as the bias exceeded approximately 3 kV a small secondary bump started emerging in the time trace of the PMT signal. Its shape and amplitude changed as the anode voltage increased up to 4 kV. This data is shown in Figure 37, where the first peak corresponding to the lamp leakage light which is truncated by the oscilloscope as it extends beyond the screen. This truncation was necessary given the comparatively much smaller scale of the EL pulse. In order to minimize noise on the EL pulse it was necessary for the vertical scale to be extremely small given its direct impact on the scope's resolution, as mentioned earlier in section 4.1.1. This bias dependence of the secondary pulse is a good sign that it is indeed electroluminescent light, as the higher the field the more likely the photoelectrons are to gain enough energy to excite Xe atoms between collisions and in turn the more EL photons are produced. To obtain more information on how these EL pulses change with bias when it comes to their amplitude, width

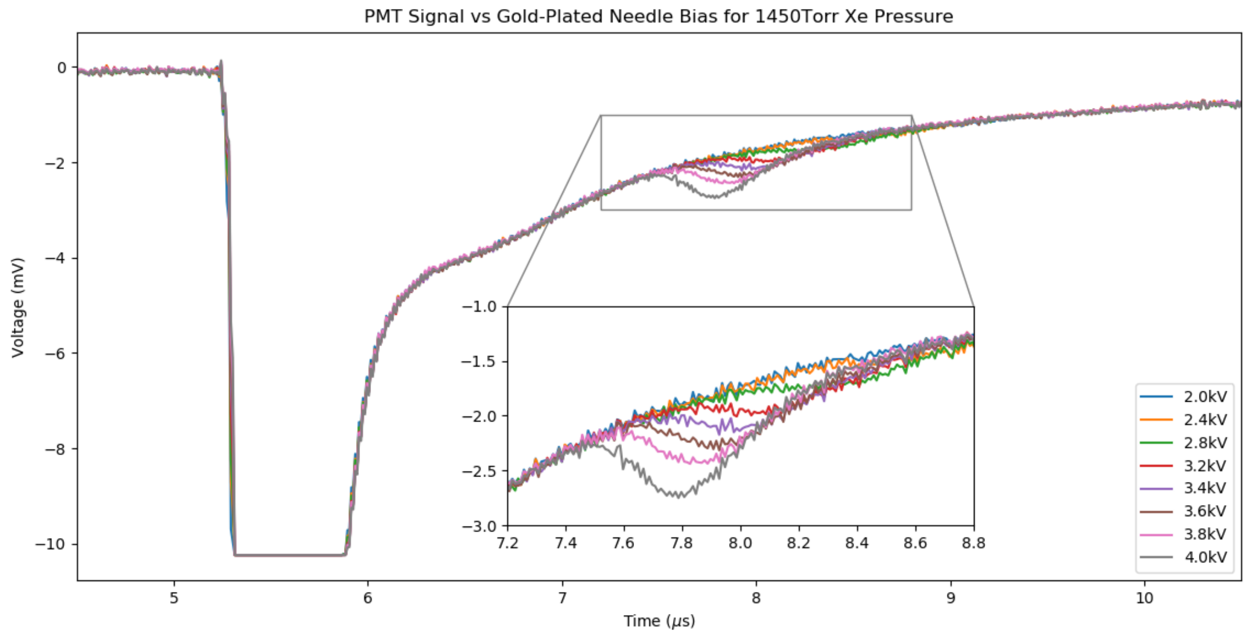

Figure 37: Averaged sets of 200 raw light data traces with the Xe flash lamp showing the emergence of electroluminescent light emission at around 8 μs. The bias was varied from 2 kV where no EL is noticeable to 4 kV where a very visible peak is present. The PMT bias was held at 2.4 V for these measurements to prevent the intense lamp signal from damaging the PMT.

and position in time, the raw data shown in Fig. 37 was fitted. The fitting function of choice for these PMT pulses was an exponentially modified Gaussian. The form of this fitting function is shown in equation 17 and is a well known model to fit PMT pulses, with examples of its application in chromatography measurements (see [113]) and data from the Daya Bay neutrino experiment (see [114, 115]):

$$V(x; A, \mu, \sigma, \lambda) = A \times \frac{\lambda}{2} e^{\frac{\lambda}{2}(2\mu + \lambda\sigma^2 - 2x)} \times erfc\Big(\frac{\mu + \lambda\sigma^2 - x}{\sqrt{2}\sigma}\Big), \tag{17}$$

$$erfc(x) = \frac{2}{\sqrt{\pi}} \int_x^\infty e^{-t^2} dt. \tag{18}$$

While equation 17 clearly features the exponential and Gaussian contributions, by algebraically manipulating it to express it in its equivalent integral convolution form, the contributions from its numerous parameters are easier to understand:

$$V_{Int.}(x; A, \mu, \sigma, \lambda) = \frac{A\lambda}{\sqrt{2\pi}\sigma} \int_0^\infty e^{-\lambda t'} \times e^{-\frac{(x-\mu-t')^2}{2\sigma^2}} dt'. \tag{19}$$

In this form, the role of each parameter is much clearer; A relates to the amplitude of the peak, λ is the decay rate of the exponential by which the Gaussian is modified, μ is the center of the unmodified Gaussian and σ, its standard deviation, drives the width of the distribution. One important note is that the mean and standard deviation of the modified distribution change and are expressed as m and s, respectively [113]:

$$\begin{aligned} m =& \mu + 1/\lambda, \\ s =& \sqrt{\sigma^2 + (1/\lambda)^2}. \end{aligned} \tag{20}$$

The best measure of the amplitude of the EL pulses from this fitting function is given by $A \times \lambda/2$ from equation 17, which, given the units of each parameter (volts for A and s^{-1} for λ), ends up having units of V$\times$s^{-1}; nevertheless, the overall function has proper units of volts given the integral of the Gaussian has units of time.

For the data shown in Figure 37, where every waveform is composed of two overlapping pulses (leakage pulse and EL pulse that emerges on the former's tail) it is necessary to fit a sum of these functions along with a constant parameter to describe the baseline, resulting in an overall fitting function defined by:

$$f(x; A_1, \mu_1, \sigma_1, \lambda_1, A_2, \mu_2, \sigma_2, \lambda_2, B) = V(x; A_1, \mu_1, \sigma_1, \lambda_1) + V(x; A_2, \mu_2, \sigma_2, \lambda_2) + B. \tag{21}$$

A fit of the 4 kV raw data is shown in Figure 38. It is important to note that the fitting time interval chosen for these fits is restricted to 7.25 μs - 10 μs. This is done for two reasons, the first being the fact that the leakage peak from the flash lamp is truncated and

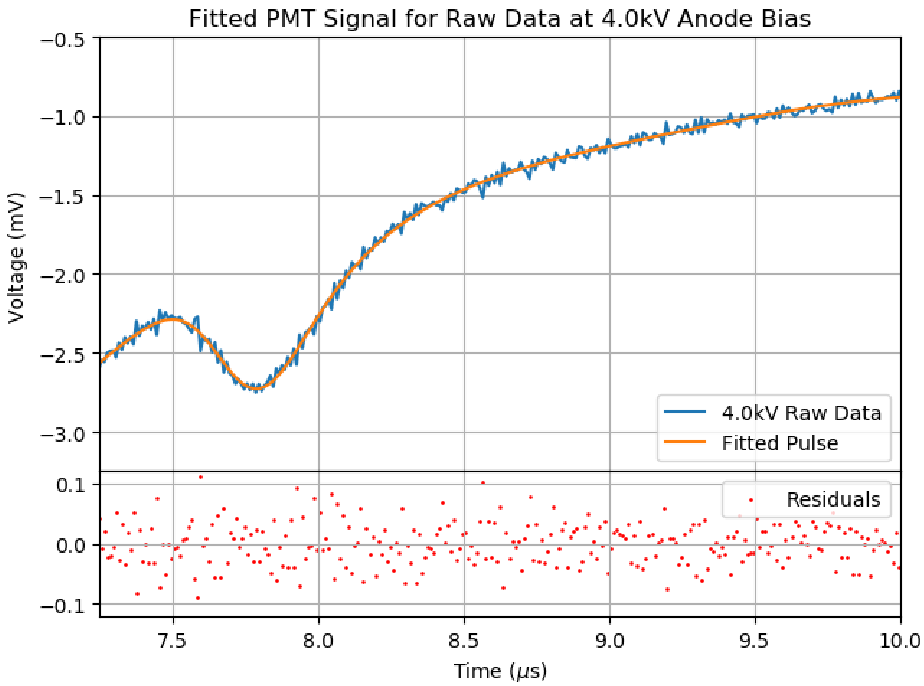

Figure 38: Fit of the 4 kV electroluminescent pulse raw data. Shown are also residuals with uncertainties on the order of 0.1 mV. Even without the inclusion of the afterpulsing contribution there is not any noticeable deviation from the raw data as suggested by the lack of trend on the residuals. The residuals' units are the same as those of the y-axis.

thus not fully present; hence, only the region where its decaying tail overlaps with the EL pulse is chosen. The second reason has to do with the consistent presence of an extremely shallow second peak around 6.5 μs $\sim$ 7 μs. This is presumed to be a very shallow feature which stems from the primary leakage pulse and is most likely due to PMT afterpulsing. Initially, a fit including 3 of the terms presented in eq. 17 was attempted to try to account for the afterpulsing. However, beyond a noticeable reduction in fitting speed, the resulting parameters for the EL pulse do not change in any decimal digit larger than the uncertainty on the parameters themselves. For this reason, the fit to the afterpulsing was omitted and the time interval adjusted accordingly. Some of these pulses need to be fitted with more caution than others, namely the ones with lower amplitudes need more accurate initial parameters to obtain a good fit. Trying to fit the 2 kV data in particular can be said to be questionable as Figure 37 suggests no real evidence whatsoever of electroluminescence for this data. Nevertheless, by fitting the aforementioned pulses it is easy to see an evolution in both their amplitude, position and width as illustrated in Fig. 39.

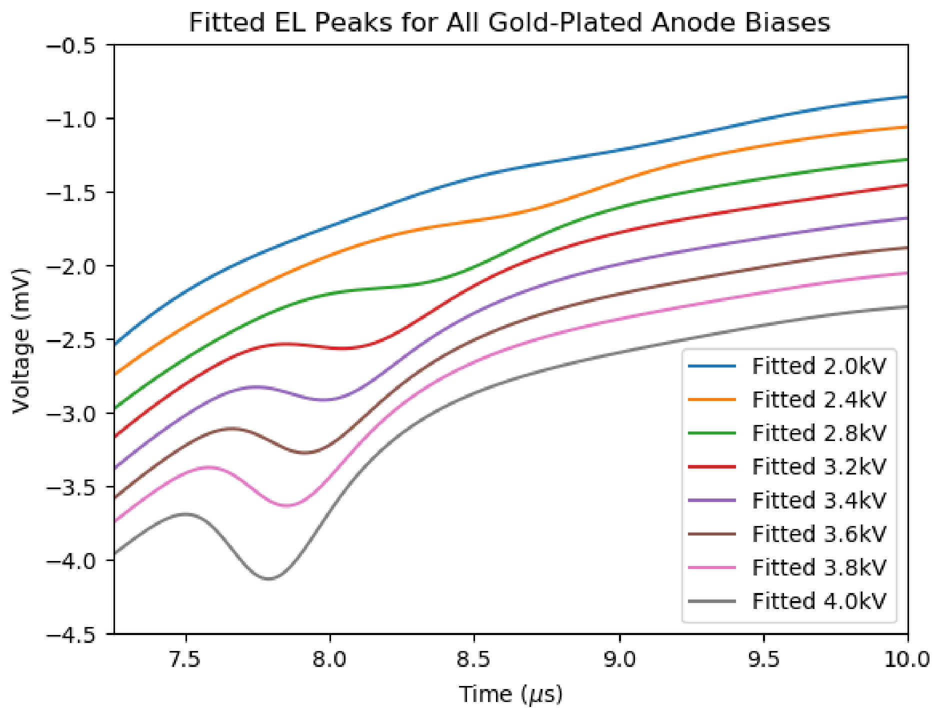

Figure 39: Fits for all EL pulses at various gold-plated anode biases between 2 kV and 4 kV. A clear trend can be seen both in the height, position and width of the peaks. Note that the fits are vertically offset by 0.1 mV each for clarity; however, there is no horizontal offset.

From the fits in Figure 39, three trends emerge with increasing anode bias; most notably a larger pulse amplitude corresponding to more photon emission, but also noticeable is that EL light pulses occur earlier in time and have shorter widths. All of the fit parameters proper to the pulses illustrated above are presented in Table 2 showing these trends quantitatively. Note how the fitted parameters for the 2 kV pulse have very large uncertainties compared to the other fits. Based on the error of the fit parameters and the shape of the data for 2 kV bias it is really hard to believe that there is an EL pulse at all. For the fits with anode biases at 2.4 - 4 kV the trends are relatively clear even when un-

Bias (kV)	Amplitude $A \times \lambda/2$ (mV$\times\mu$s^{-1})	m (μs)	s (μs)
2.0	$(-1.00 \pm 2.00) \times 10^{0}$	8.00±1.00	0.700±0.700
2.4	$(-3.00 \pm 1.00) \times 10^{-1}$	8.70±0.10	0.470±0.090
2.8	$(-4.00 \pm 2.00) \times 10^{-1}$	8.40±0.10	0.250±0.040
3.2	$(-3.20 \pm 0.50) \times 10^{-1}$	8.33±0.04	0.280±0.030
3.4	$(-4.10 \pm 0.40) \times 10^{-1}$	8.24±0.03	0.260±0.020
3.6	$(-5.00 \pm 0.40) \times 10^{-1}$	8.14±0.02	0.230±0.010
3.8	$(-6.40 \pm 0.50) \times 10^{-1}$	8.03±0.02	0.200±0.010
4.0	$(-8.80 \pm 0.60) \times 10^{-1}$	7.93±0.01	0.170±0.008

Table 2: All fit parameters for the gold-plated anode EL pulse measurements. The units for the amplitude are in mV$\times\mu$ s^{-1} as both the A term and the $\lambda/2$ term affect the amplitude of the pulse. The units of λ are inverse time as it must cancel out the time units from the complementary error function (given in eq. 18).

certainties are considered: as anode bias increases the EL pulse's amplitude increases, it occurs earlier in time (decreasing m) and also becomes narrower (decreasing s).

The increase in amplitude is directly correlated to the field strength; a higher field at constant pressure means more energy gain for photoelectrons before successive collisions and thus a lower distance travelled to produce a 172 nm photon, as seen from eq. 12, meaning more photons produced in total across the same drift distance. The mean of the pulse decreases with increasing voltage because a higher bias (and thus stronger field) increases electron drift speed in the Xe (see [116, 117] for electron drift speed in mm/μs as a function of reduced electric field E/p). In turn, they take less time to reach the region near the anode tip where the gradient is strongest and most EL photons are produced, which causes the pulse to occur earlier. The larger pulse width at lower biases can be understood by considering both the evolution of the drift velocity as well as the distance required to produce one EL photon. From [116, 117] one can see that, at a constant pressure, the weaker the electric field, the lower the drift speed; in addition, from eq. 12 a lower electric field increases the drift distance required to produce a photon. This results in more time required to produce each subsequent photon, effectively increasing the length of the pulse.

4.2.2 Steel Needle Light Measurements

The gold-plated anode was changed to a much pointier and thinner stainless steel needle mainly for the reason that the former simply seemed to produce too little EL light. Despite being a great proof of concept for the experiment, the pulses shown in Figure 37 leave much to be desired, especially for the applications needed for SiPM testing. Even when pushed to the highest bias right before Xe gas breakdown, the pulse amplitudes are only one order of magnitude larger than the electronics noise. Additionally, the Xe flash lamp is unfortunately indispensable for the gold-plated needle geometry: it is impossible to produce EL light using the LED with the gold-plated anode as the latter's weaker field gradient coupled with the greatly reduced number of photoelectrons produced by the LED did not allow any detection of EL light regardless of anode bias. Furthermore, this dependence on the Xe flash lamp for the gold-plated needle geometry places a strict limit on the maximum bias voltage that can be applied to the PMT to avoid damage. This is also detrimental, as higher PMT biases greatly increase the signal (the EL pulses discussed in this section for instance do not become visible until $V_{PMT} > 3.8$ V).

Before the focusing lens system described in section 3.4.2 was assembled, the LED was quickly tested at various settings with the steel needle using a xenon pressure of 381 Torr and a PMT voltage of 4.5 V (kept constant through all measurements in this subsection). It was quickly realized that despite the much lower breakdown voltage of 1.8 kV at this pressure, EL pulses could already be produced at voltages as low $\sim$ 1.1 kV - 1.2 kV. To verify that the emitted photons are indeed electroluminescent in origin, a 172$\pm$2.5 nm center wavelength and 20$\pm$7.5 nm FWHM filter from eSource Optics (see [118]) was used. Note that the only process that could produce 172 nm light was electroluminescence, as the LED is the only other source of light, and its emission wavelength is sharply centered around 265 nm. The expected signal once the filter is placed in front of the PMT is thus a disappearance of the LED leakage pulse and an $\sim 85\%$ attenuation of the secondary pulse, according to the filter specifications found in [118]. 200 averaged raw data traces are shown in Figure 40 with and without 172 nm filter in front of the PMT.

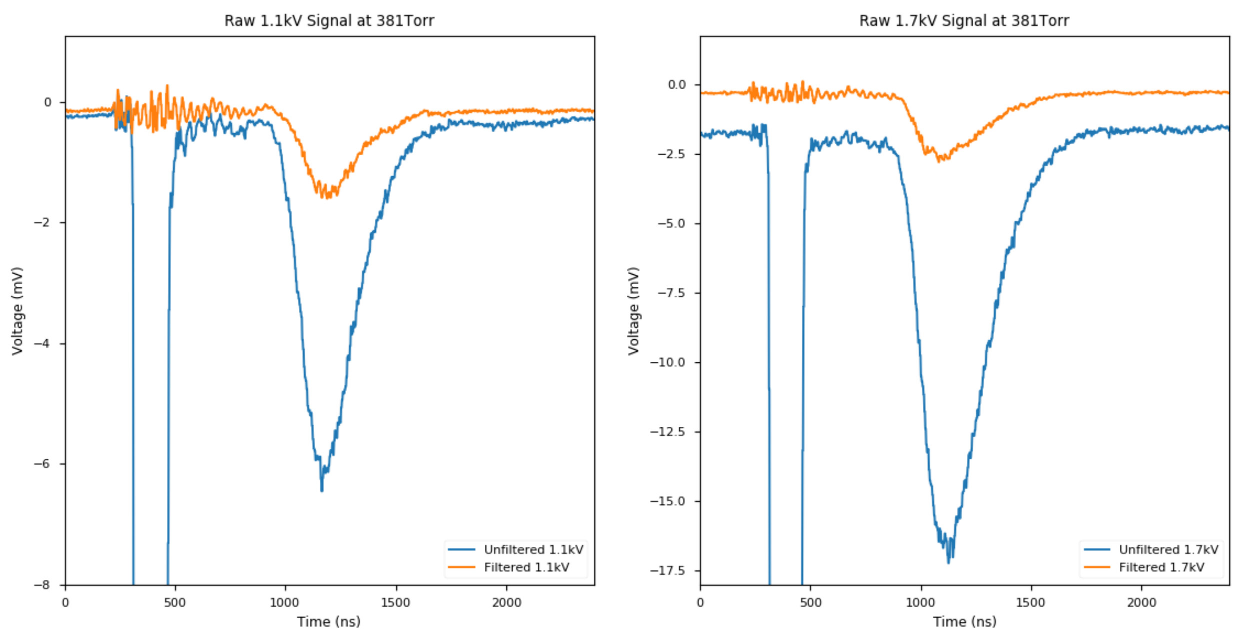

Figure 40: On the left: Raw data with and without 172 nm filter in front of the PMT at 1.1 kV. On the right: same data but at a 1.7 kV bias. When the leakage pulse is attenuated the electronic noise left is due to the signal generator input into the LED.

The methodology for the steel needle data is very similar to the one in the previous section with one major difference. The oscilloscope is replaced with the CAEN digitizer and the primary data processing and analysis is done in Root. Given the digitizer's much quicker data acquisition rate (up to 7 kHz) as mentioned in section 3.4.1, Root and C++ are used in order to quickly acquire and package the data in highly compressed data files. The raw data files are processed in Root and are then loaded into Python via Uproot for plotting and fitting (see [110] for details about Uproot).

With the digitizer's fast data collection, the amount of data traces collected for every pulse width and bias is on the order of 10^6 rather than the 200 pulses recorded with the oscilloscope. This large number of waveforms is averaged in Root and imported into Python as a single trace for fitting. An example of raw waveforms imported into Python is shown in Fig. 41 for a few biases at 700 Torr Xe pressure using 80 ns LED pulses. Notice how the EL signal is

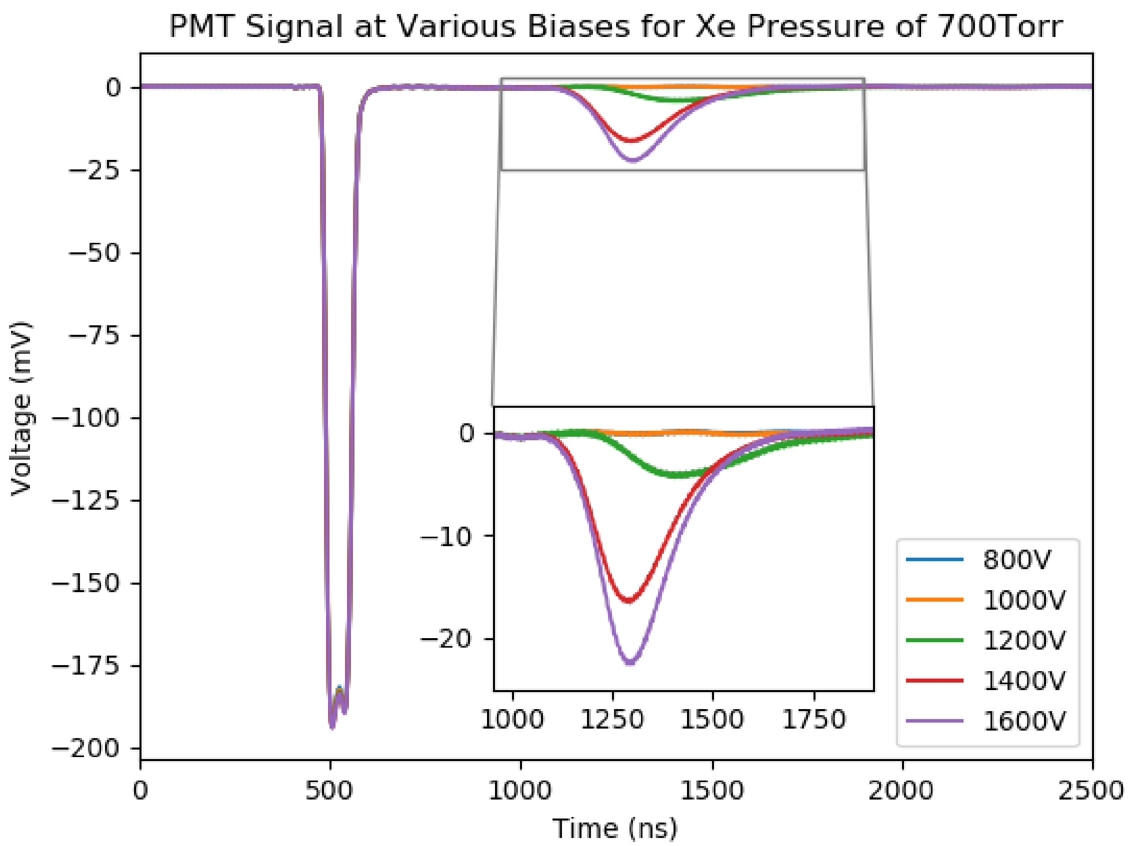

Figure 41: Raw data traces from Root imported in Python for various biases. Notice the digitizer's ability to fit both the full leakage pulse and the EL pulse without losing resolution. Data points are taken every 2 ns and a full trigger window lasts for 2.5 μs.

already appearing at 1.2 kV with an amplitude of 5 mV using the much weaker LED as light source and proceeds to reach much higher amplitudes within a few hundred volts of anode bias. Recall that the primary goal of the steel needle is to have much stronger field gradients near the anode tip in an attempt to produce as much EL light as possible. A confined field helps with accelerating the electrons over a much shorter distance and thus minimizes energy losses due to elastic scattering; something longer range fields like the one of the gold-plated anode fail to achieve. For this reason, the amplitude of the

EL pulses will be the main quantity of interest when comparing the fits in this subsection. Since the LED is used for these measurements, its leakage pulse does not have any overlap with the EL pulse as can be seen in Figure 41. Thus, equation 17 with the addition of a baseline term B is enough to fit the 172 nm pulses. In Figure 42, approximately 10^6 raw waveforms were averaged and fitted.

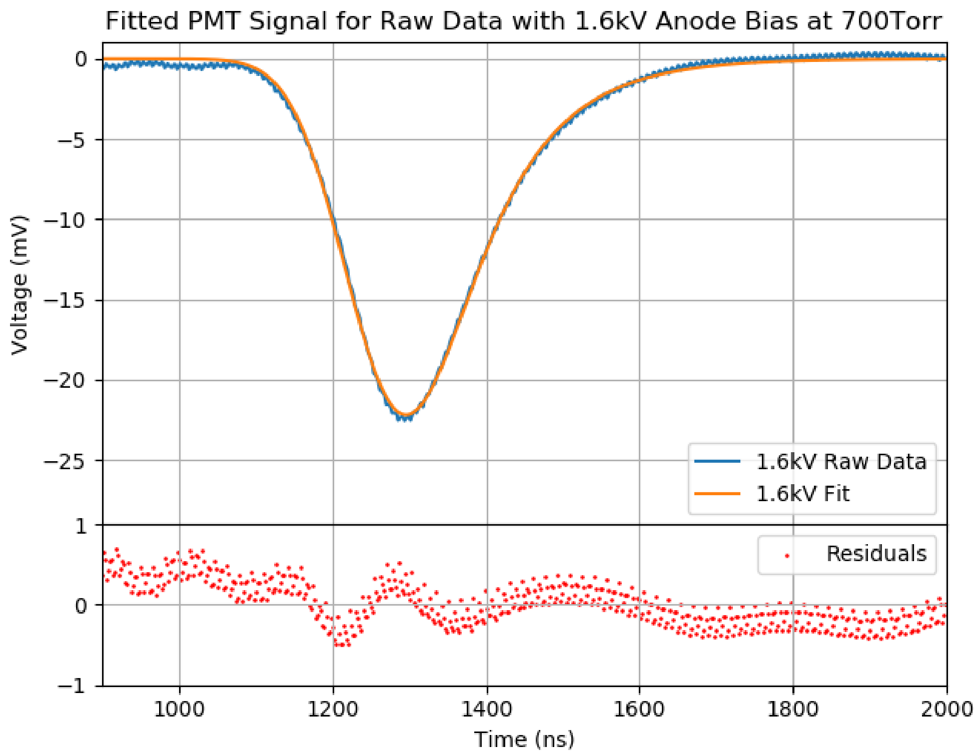

Figure 42: Fit of approximately 10^6 averaged raw data traces of electroluminescent light at 700 Torr and 1.6 kV bias. This wavy behavior of the residuals is common for basically all EL pulses with the steel needle. The small ripples before the peak in the raw data might be due to noise from the digitizer or the PMT. The uncertainties on the residuals have been omitted for clarity and are on the order of 0.2 mV. As in previous plots with residuals, their units are the same as those of the main y-axis.

The initial target for the bias ranges for every pressure was to start at 900 V and stop once the bias is within $200 - 300$ V of the breakdown voltage. The reason for this is that as the bias gets closer to breakdown the baseline on the raw data traces as well as the pulses (both leakage and EL) themselves start becoming unstable and greatly fluctuate. Additionally, for biases around 2.8 kV and higher it was noticed from looking at single triggers on the digitizer that an increase in both the signal noise and the baseline magnitude was present, both effects increasing with higher voltages. This happened even for pressures like 1450 Torr where the breakdown was much higher than 2.8 kV. The source of this effect is not understood but it is surmised to possibly be due to the metallic dark box front panel through which all connections pass, as noise issues stemming from it were observed on a few instance during charge data tests. Furthermore, as the steel needle light data measurements were taken over different days, a change in the intensity of the LED leakage pulse was observed as shown in Figure 43.

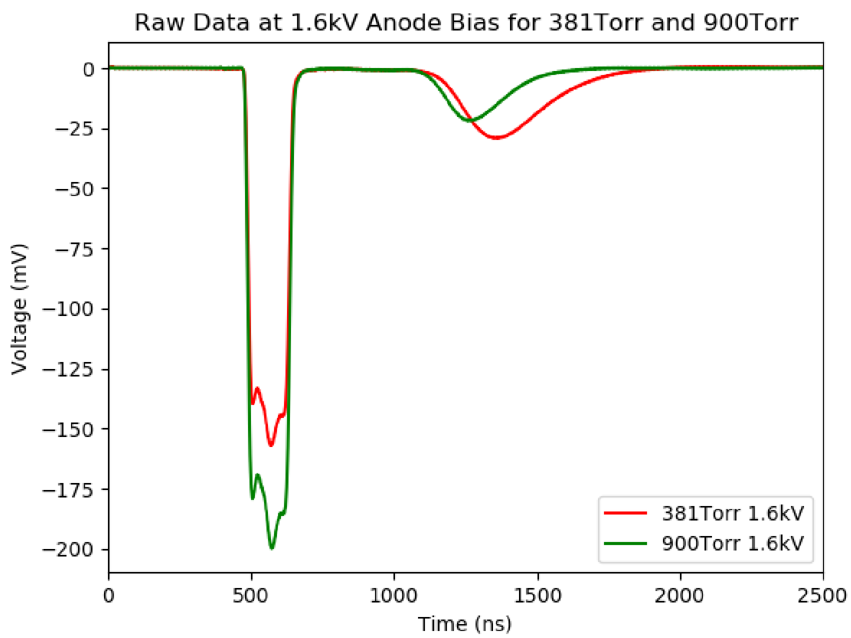

Figure 43: Example of different leakage amplitudes for two different pressures at the same anode bias. The data sets for 381 Torr and 900 Torr were taken on Oct. 11$^{\text{th}}$ 2019 and Oct. 14$^{\text{th}}$ 2019, respectively.

For this reason, the amplitude of an EL pulse here will be normalized by dividing it by the amplitude of the leakage pulse from the same trace. This is motivated by the fact that more intense LED pulses will produce more photoelectrons and thus more electroluminescent light at a given pressure and bias. Since the units of amplitude were previously in voltage multiplied by inverse time, the division explained above results in normalized amplitudes having units of inverse time and are given by $(A_{EL}\lambda)/(2A_{Leak})$. Figures 44 and 46 are heat map plots of the normalized amplitude achieved using 80 ns and 160 ns long LED input pulses, respectively. These heat maps show the normalized amplitude as a function of anode bias and Xe pressure. The uncertainty in each of the values is shown in heat map format again in Figures 45 and 47 for 80 ns and 160 ns long LED pulses respectively.

Figures 44 and 46 demonstrate two very clear trends: an increase in the minimum bias required to produce EL as the gas pressure increases, and an overall increase in the normalized amplitude for any given pressure as bias is increased. To understand the former, recall from section 4.2.1 that there is a threshold for the reduced electric field before electroluminescence begins. As the pressure in the system increases, so must the strength of the electric field in order to meet this threshold. A higher pressure not only means more energy losses to elastic scattering compared to the same bias at a lower pressure, but given the field's more localized nature, its strength at the cathode at lower voltages could be too weak for electrons to even reach the high field region. Meanwhile, the amplitude increase with increasing bias, at least until breakdown in the gas, or the aforementioned noise increase at biases of 2.8 kV and more, is due to the reduced drift distance required for EL photons to be produced and hence a larger number of 172 nm photons emitted. One can also see from both maps that for the biases and pressures investigated, the overall amplitude seems to go down with increasing pressure. However, this could be false and if the noise and signal deterioration issues faced beyond 2.8 kV were resolved one might expect to see amplitudes reaching or even surpassing the maximal values obtained at lower pressures. After all there will be a larger amount of Xe atoms to excite and the

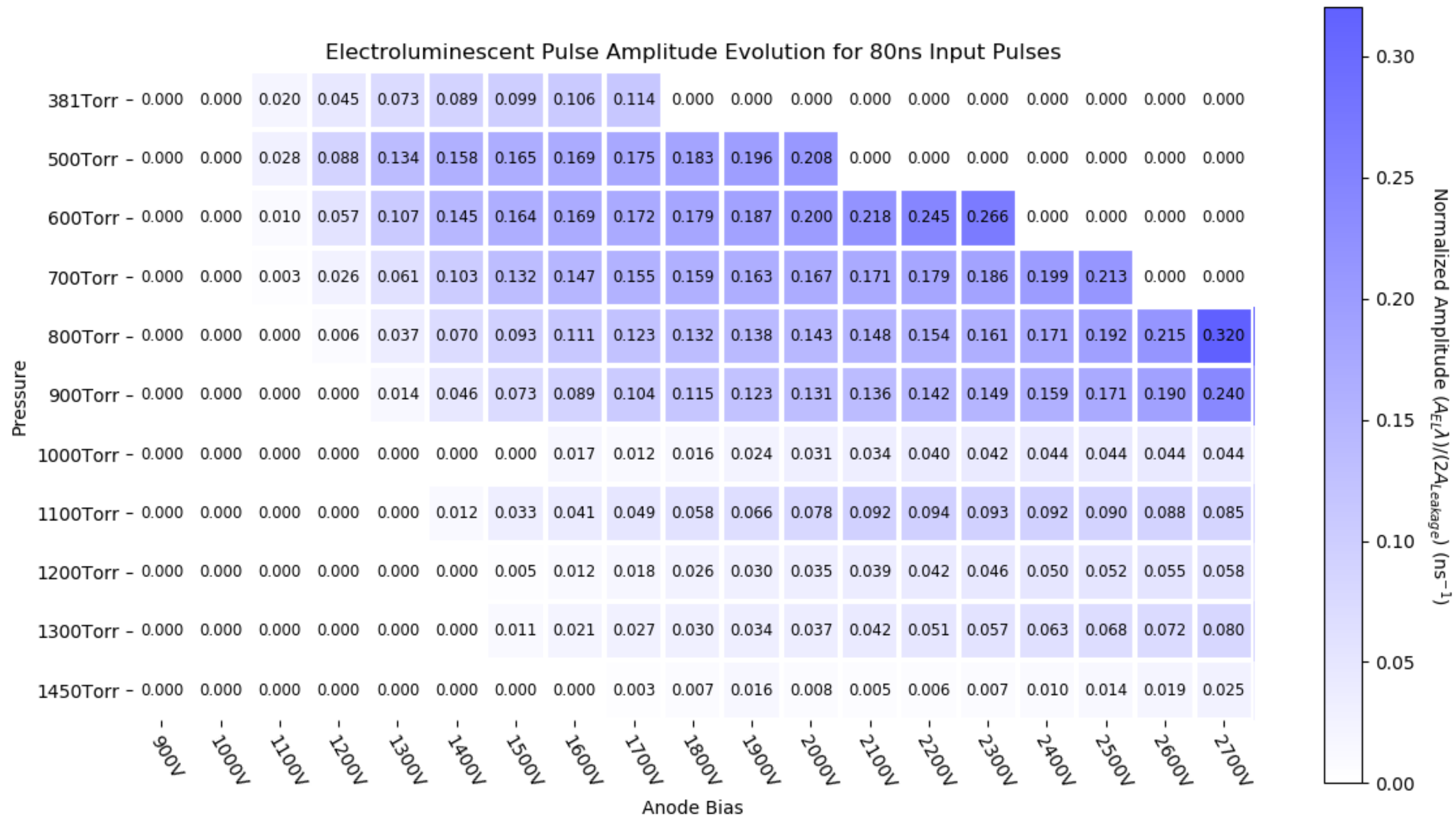

Figure 44: Map showing the evolution of normalized electroluminescent pulse amplitudes as a function of pressure and steel anode bias for 80ns LED input pulses. Values of 0 amplitude on the left side of the map are due to the lack of EL light while those on the right side of the map are due to voltages very near, at or above breakdown.

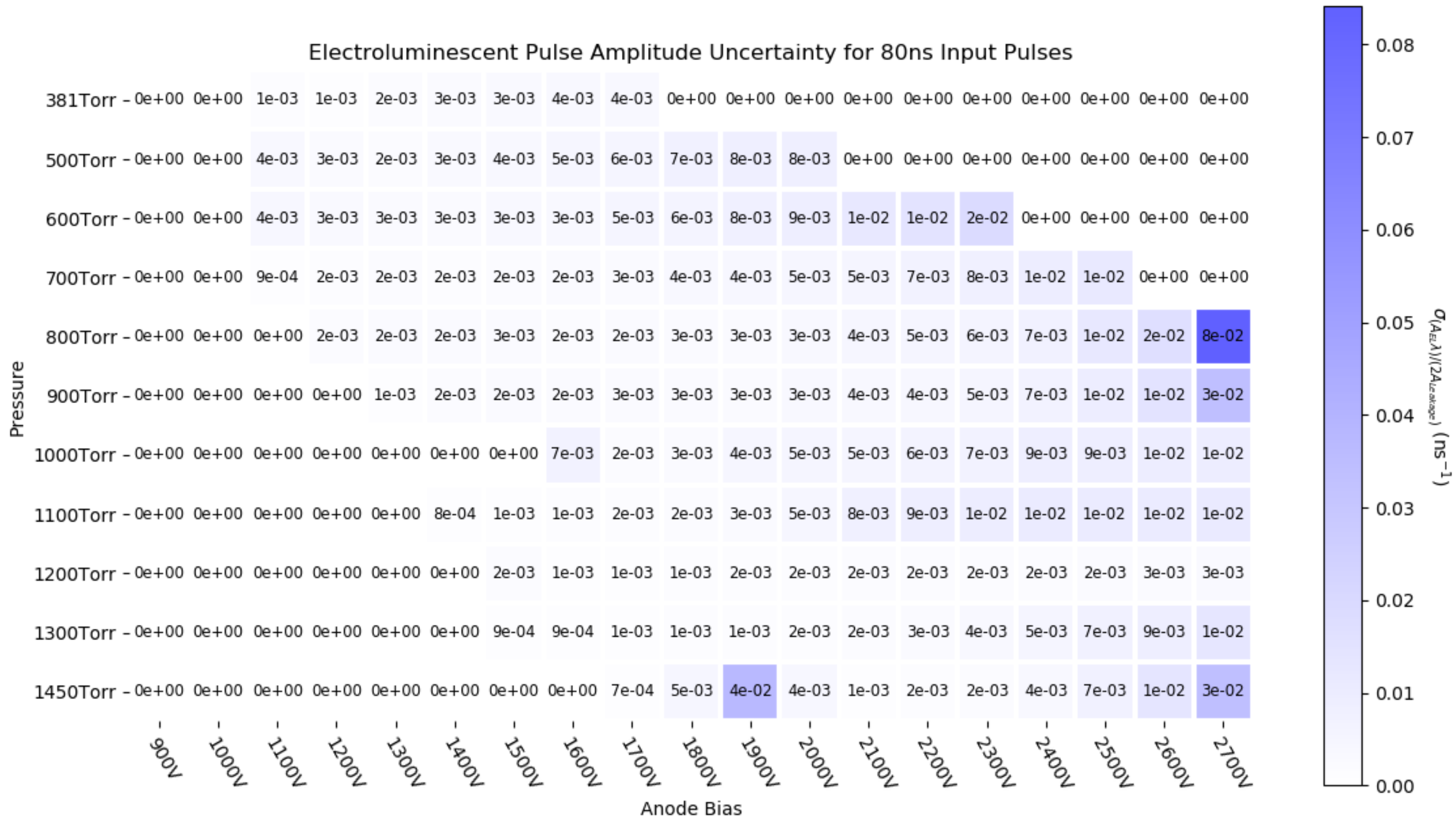

Figure 45: Map of the uncertainty on the normalized amplitudes shown on the previous page.

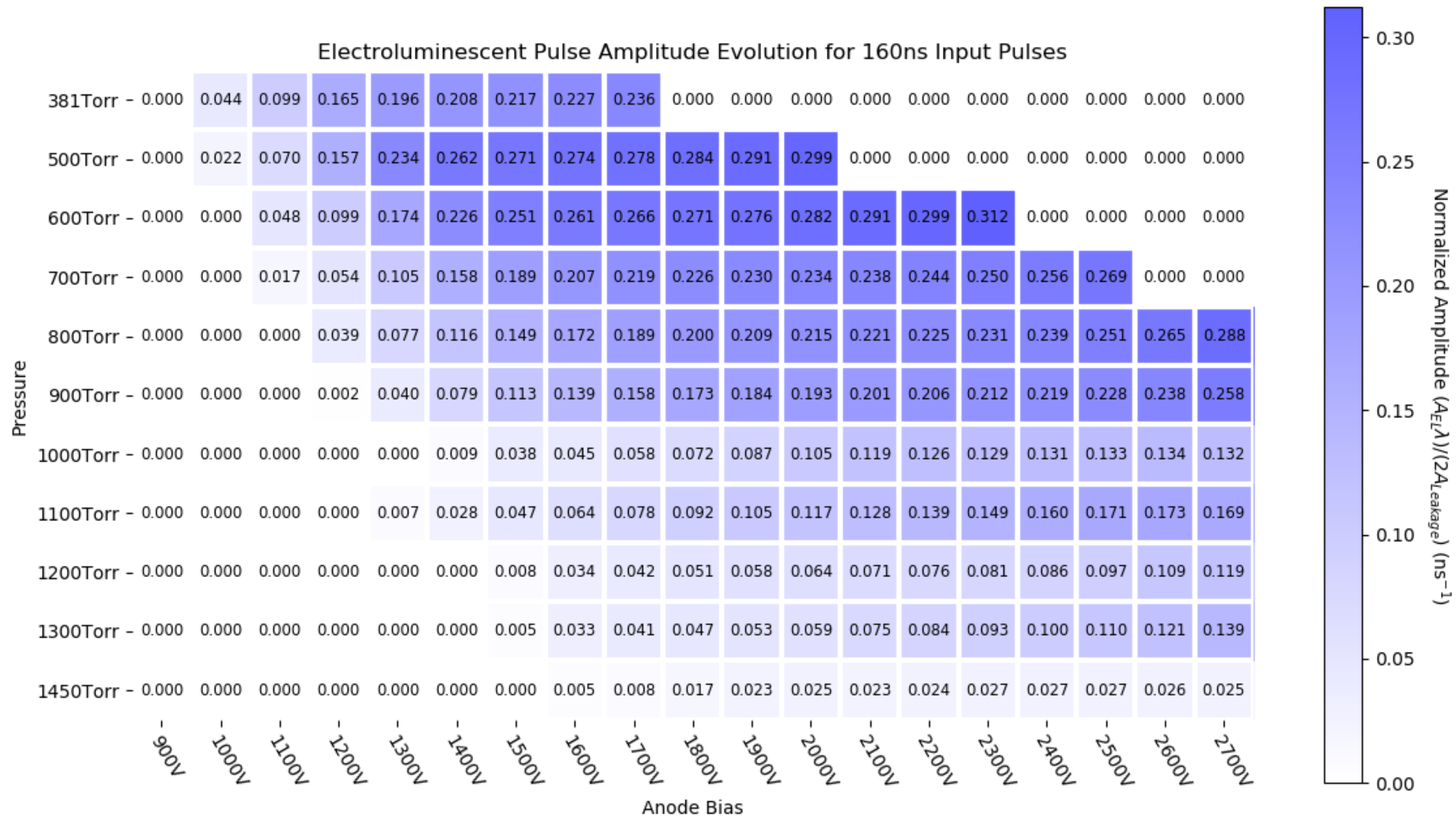

Figure 46: Map showing the evolution of normalized electroluminescent pulse amplitudes as a function of pressure and steel anode bias for 160ns LED input pulses. As with the 80ns input pulse data, amplitudes of 0 on the left side of the map are due to the lack of EL light while those on the right side of the map are due to voltages very near, at or above breakdown.

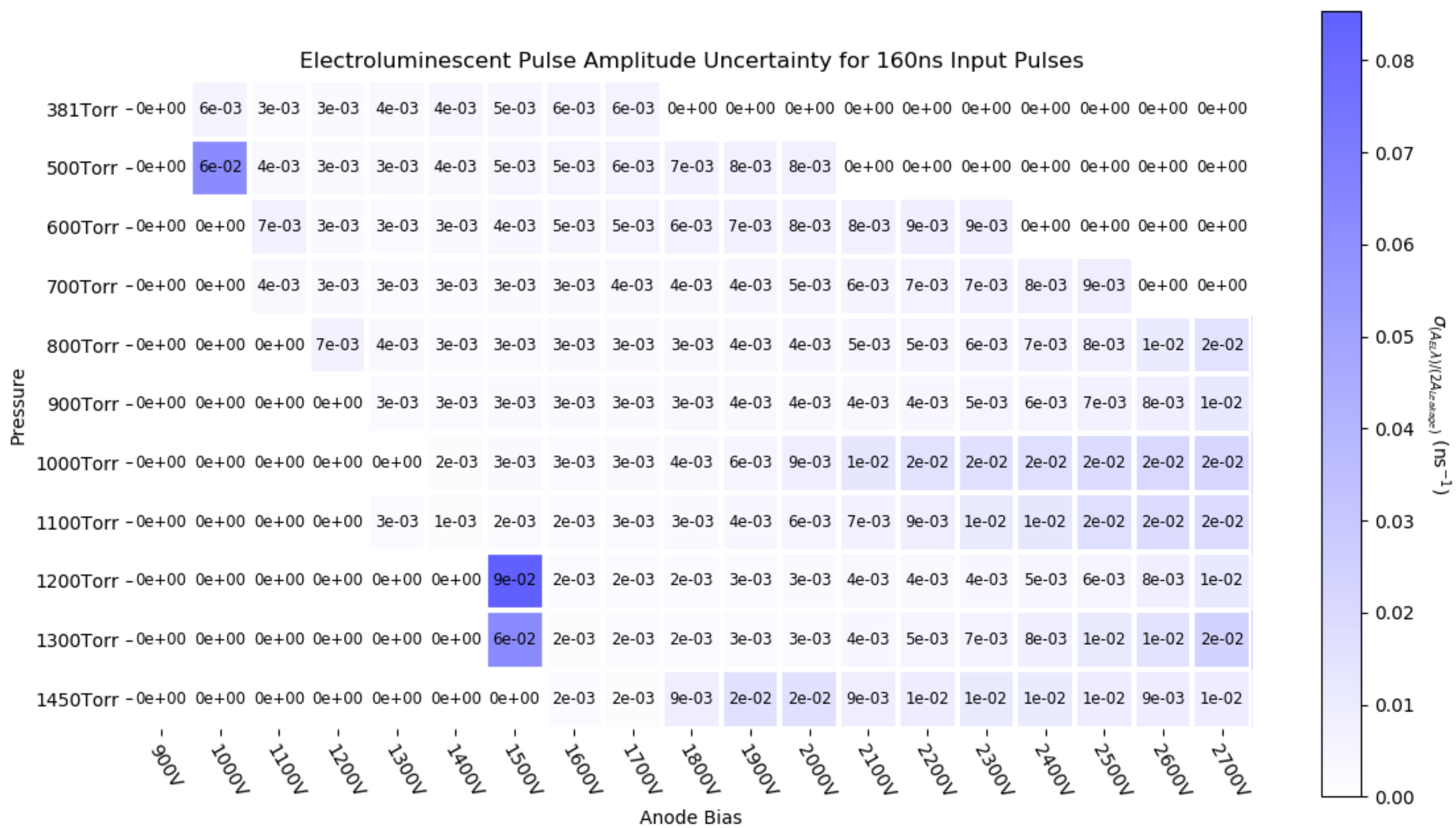

Figure 47: Map of the uncertainty on the normalized amplitudes shown on the previous page.

bias for pressures above 1000 Torr can be increased by more than 800 V before breakdown occurs. However, due to the stainless steel anode's geometry, it is possible that its field at the cathode is too weak to drift the emitted photoelectrons as the gas density keeps increasing with pressure. This can result in much lower electron numbers at the anode tip. One common and odd feature of both maps is the systematically lower normalized amplitude of the 1000 Torr data. Even with uncertainties under consideration, the data for all biases is far lower than one would expect by looking at the neighboring data points. Additionally, this is directly reflected by the raw data, too, as shown in Figure 48 for 160 ns input pulses. The reason for this is not understood; the leakage amplitudes for all data

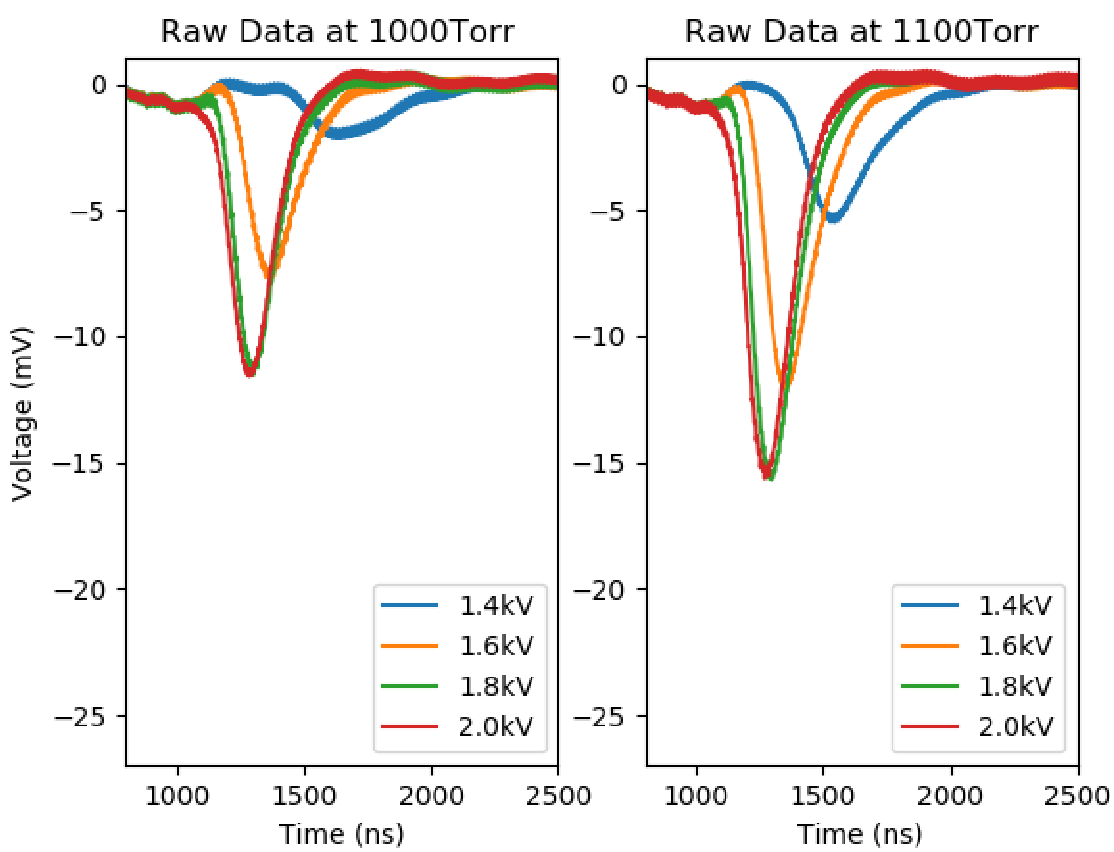

Figure 48: Comparison of 4 biases for pressures of 1000 Torr and 1100 Torr showing systematically smaller EL pulses at 1000 Torr pressure.

sets except 381/500/600 Torr are consistent with eachother. The 1000 Torr measurements were performed on the same day as the 700/800/900/1100 Torr measurements and none of these display a similar anomaly.

Successful EL emission has been demonstrated for the steel needle at various pressures and biases with the maximum amplitude for an anode-photocathode separation of 7.5 mm occurring at a pressure of 600 Torr and a bias of 2.3 kV. While electroluminescence in Xe gas was produced with two different anode geometries, the EL pulses shown in this work still have pulse widths of a few hundred nanoseconds and are too long to be used for SiPM testing. Possible changes to the experimental setup that can be made in the future to mediate this include taking measurements at shorter anode-photocathode distances to investigate if bringing the high field region closer to the cathode decreases the pulse width as well as the effect this has on the pulse amplitude. A shorter pulse width and a more intense UV LED can also be used to produce photoelectrons in a shorter time span; while the Thorlabs UV LED used here could output pulses as short as 20 ns in duration, it was observed that their intensity was too low to produce EL emission.

5 Conclusion

As the only neutral fermionic, and now known to be massive, elementary particles, neutrinos are still mysterious to physicists more than 60 years after their discovery [1–5]. Experiments around the world tackle question about the neutrino's properties such as its mass and its possible Majorana nature.

The nEXO experiment plans to investigate the latter by using a 5 tonne LXe TPC in an attempt to detect neutrinoless double beta decay [31, 33]. The detection of this exotic event in ^{136}Xe would confirm the Majorana nature of neutrinos. Furthermore, it would also be a direct observation of violation of lepton number conservation which represents physics beyond the Standard Model of Particle Physics; the leptogenetic nature of the process could also be a hint to solving the matter-antimatter asymmetry observed in the universe [30]. To detect a $0\nu\beta\beta$ decay, nEXO will use silicon photomultipliers to sense the scintillation signal in liquid xenon; given the extremely rare nature of this decay, the detector needs extremely good light energy resolution.

The work presented in this thesis describes the development and first results of an electroluminescent light source to produce VUV photons for SiPM testing and characterization for nEXO. First results of VUV photon production were demonstrated using a Xe flash lamp and a gold-plated copper anode at 1450 Torr. The evolution of electroluminescent pulses produced at biases ranging from 2-4 kV were demonstrated and fitted. The highest intensity pulses made with the gold-plated needle had an approximate 500 ns duration and sub mV amplitudes. In order to improve on the intensity of the VUV pulses a sharp and thin steel needle was fabricated and tested. The evolution of EL pulses produced with it, using a 265 nm LED, was shown for two different pulse durations and based on the provided results, the optimal pressure and bias for the steel needle are 600 Torr and 2.3 kV respectively. Despite boasting higher intensity for the VUV photon pulses, the steel needle geometry does not really improve on the output pulse duration. Moving forward, future measurements could include varying the anode-cathode distance and observing its impact on the amplitude and duration of the resulting pulses, or using a higher intensity, shorter input pulse duration LED to produce larger amounts of photoelectrons over smaller time frames.

References

[1] F. Reines and C. Cowan. The Reines-Cowan experiments: Detecting the Poltergeist. *Los Alamos Sci.*, 25:4–27, 1997.

[2] S. M. Bilenky. Neutrino in Standard Model and Beyond. *Physics of Particles and Nuclei*, 46(4):475–496, 2015.

[3] Y. Fukuda, T. Hayakawa, E. Ichihara, K. Inoue, K. Ishihara, H. Ishino, Y. Itow, T. Kajita, J. Kameda, S. Kasuga, and et al. Evidence for Oscillation of Atmospheric Neutrinos. *Physical Review Letters*, 81(8):1562–1567, Aug 1998.

[4] K. Eguchi, S. Enomoto, K. Furuno, J. Goldman, H. Hanada, H. Ikeda, K. Ikeda, K. Inoue, K. Ishihara, W. Itoh, and et al. First Results from KamLAND: Evidence for Reactor Antineutrino Disappearance. *Physical Review Letters*, 90(2), Jan 2003.

[5] A. Bellerive, J.R. Klein, A.B. McDonald, A.J. Noble, and A.W.P. Poon. The Sudbury Neutrino Observatory. *Nuclear Physics B*, 908:30–51, Jul 2016.

[6] K.A. Olive. Review of Particle Physics. *Chinese Physics C*, 40(10):100001, oct 2016.

[7] R. N. Mohapatra, S Antusch, K S Babu, G Barenboim, M-C Chen, A de Gouvêa, P de Holanda, B Dutta, Y Grossman, A Joshipura, and et al. Theory of neutrinos: a white paper. *Reports on Progress in Physics*, 70(11):1757–1867, Oct 2007.

[8] K. S. Babu and V. S. Mathur. Radiatively Induced Seesaw Mechanism for Neutrino Masses. *Physical Review D*, 38:3550, 1988.

[9] Murray Gell-Mann, Pierre Ramond, and Richard Slansky. *Complex Spinors and Unified Theories*, pages 266–272.

[10] Tsutomu Yanagida. Horizontal Symmetry and Masses of Neutrinos. *Progress of Theoretical Physics*, 64(3):1103–1105, 09 1980.

[11] M. Goeppert-Mayer. Double Beta-Disintegration. *Physical Review*, 48:512–516, Sep 1935.

[12] Steven Herrin. Double Beta Decay in Xenon-136: Measuring the Neutrino-Emitting Mode and Searching for Majoron-Emitting Modes. Master's thesis, Stanford U., Phys. Dept., 2013.

[13] A. S. Barabash. Experiment Double Beta Decay: Historical Review of 75 Years of Research. *Physics of Atomic Nuclei*, 74(4):603–613, Apr 2011.

[14] R. Arnold, C. Augier, A.M. Bakalyarov, J.D. Baker, A.S. Barabash, A. Basharina-Freshville, S. Blondel, S. Blot, M. Bongrand, V. Brudanin, and et al. Measurement of the Double-beta Decay Half-life and Search for the Neutrinoless Double-beta Decay of ^{48}Ca with the NEMO-3 Detector. *Physical Review D*, 93(11), Jun 2016.

[15] C. Alduino, K. Alfonso, D. R. Artusa, F. T. Avignone, O. Azzolini, T. I. Banks, G. Bari, J. W. Beeman, F. Bellini, A. Bersani, and et al. Measurement of the Two-Neutrino Double-Beta Decay Half-life of ^{130}Te with the CUORE-0 Experiment. *The European Physical Journal C*, 77(1), Jan 2017.

[16] E. Aprile et al. Observation of Two-Neutrino Double Electron Capture in ^{124}Xe with XENON1T. *Nature*, 568(7753):532–535, 2019.

[17] A. Gando et al. Search for Majorana Neutrinos Near the Inverted Mass Hierarchy Region with KamLAND-Zen. *Physical Review Letters*, 117:082503, Aug 2016.

[18] M. Agostini, A. M. Bakalyarov, M. Balata, I. Barabanov, L. Baudis, C. Bauer, E. Bellotti, S. Belogurov, A. Bettini, L. Bezrukov, and et al. Probing Majorana Neutrinos with Double-β Decay. *Science*, 365(6460):1445–1448, Sep 2019.

[19] Petr Vogel. Nuclear Structure and Double Beta Decay. *Journal of Physics G: Nuclear and Particle Physics*, 39(12):124002, Nov 2012.

[20] J. Kotila and F. Iachello. Phase-space Factors for Double-β Decay. *Physical Review C*, 85(3), Mar 2012.

[21] Michelle J. Dolinski, Alan W.P. Poon, and Werner Rodejohann. Neutrinoless Double-Beta Decay: Status and Prospects. *Annual Review of Nuclear and Particle Science*, 69(1):219–251, 2019.

[22] P.F. de Salas, D.V. Forero, C.A. Ternes, M. Tórtola, and J.W.F. Valle. Status of Neutrino Oscillations 2018: 3σ Hint for Normal Mass Ordering and Improved CP Sensitivity. *Physics Letters B*, 782:633–640, Jul 2018.

[23] M. G. Aartsen et al. Determining Neutrino Oscillation Parameters from Atmospheric Muon Neutrino Disappearance with Three Years of IceCube DeepCore Data. *Physical Review D*, 91:072004, Apr 2015.

[24] S. Adrián-Martínez et al. Measurement of Atmospheric Neutrino Oscillations with the ANTARES Neutrino Telescope. *Physics Letters B*, 714(2):224 – 230, 2012.

[25] F. P. An et al. Measurement of Electron Antineutrino Oscillation Based on 1230 Days of Operation of the Daya Bay Experiment. *Physical Review D*, 95:072006, Apr 2017.

[26] J. Hosaka et al. Solar Neutrino Measurements in Super-Kamiokande-I. *Physical Review D*, 73:112001, Jun 2006.

[27] B. Aharmim et al. Low-Energy-Threshold Analysis of the Phase I and Phase II Data Sets of the Sudbury Neutrino Observatory. *Physical Review C*, 81:055504, May 2010.

[28] Bruce T. Cleveland, Timothy Daily, Jr. Raymond Davis, James R. Distel, Kenneth Lande, C. K. Lee, Paul S. Wildenhain, and Jack Ullman. Measurement of the Solar Electron Neutrino Flux with the Homestake Chlorine Detector. *The Astrophysical Journal*, 496(1):505–526, Mar 1998.

[29] S. Adrián-Martínez et al. Letter of intent for KM3NeT 2.0. *Journal of Physics G: Nuclear and Particle Physics*, 43, 01 2016.

[30] Oliviero Cremonesi. Neutrinoless Double Beta Decay. *Journal of Physics: Conference Series*, 718:022006, May 2016.

[31] N. Ackerman, B. Aharmim, M. Auger, D. J. Auty, P. S. Barbeau, K. Barry, L. Bartoszek, E. Beauchamp, V. Belov, C. Benitez-Medina, and et al. Observation of Two-Neutrino Double-Beta Decay in ^{136}Xe with the EXO-200 Detector. *Physical Review Letters*, 107(21), Nov 2011.

[32] Liang Yang. Status and Prospects for the EXO-200 and nEXO Experiments. *Journal of Physics: Conference Series*, 888:012032, Sep 2017.

[33] S. Al Kharusi et al. nEXO Pre-Conceptual Design Report. *arXiv:1805.11142*, May 2018.

[34] G. Anton et al. Search for Neutrinoless Double-Beta Decay with the Complete EXO-200 Dataset. *Physical Review Letters*, 123(16), Oct 2019.

[35] J.B. Albert et al. Cosmogenic Backgrounds to $0\nu\beta\beta$ in EXO-200. *Journal of Cosmology and Astroparticle Physics*, 2016(04):029–029, Apr 2016.

[36] M. Auger et al. The EXO-200 Detector, part I: Detector Design and Construction. *Journal of Instrumentation*, 7(05):P05010–P05010, May 2012.

[37] J. B. Albert et al. Improved Measurement of the $2\nu\beta\beta$ Half-life of ^{136}Xe with the EXO-200 Detector. *Physical Review C*, 89:015502, Jan 2014.

[38] J. B. Albert et al. Measurement of the Drift Velocity and Transverse Diffusion of Electrons in Liquid Xenon with the EXO-200 Detector. *Physical Review C*, 95(2), Feb 2017.

[39] M. Redshaw, E. Wingfield, J. McDaniel, and E. G. Myers. Mass and double-beta-decay Q value of Xe-136. *Physical Review Letters*, 98:053003, 2007.

[40] E. Conti, R. DeVoe, G. Gratta, T. Koffas, S. Waldman, J. Wodin, D. Akimov, G. Bower, M. Breidenbach, R. Conley, and et al. Correlated Fluctuations Between Luminescence and Ionization in Liquid Xenon. *Physical Review B*, 68(5), Aug 2003.

[41] Oliviero Cremonesi. Neutrinoless Double Beta Decay: Present and Future. *Nuclear Physics B - Proceedings Supplements*, 118:287–296, 2003.

[42] J. B. Albert et al. Search for Neutrinoless Double-Beta Decay with the Upgraded EXO-200 Detector. *Physical Review Letters*, 120(7), Feb 2018.

[43] M. Jewell et al. Characterization of an Ionization Readout Tile for nEXO. *Journal of Instrumentation*, 13(01):P01006–P01006, Jan 2018.

[44] G. Gallina et al. Characterization of the Hamamatsu VUV4 MPPCs for nEXO. *Nuclear Instruments and Methods in Physics Research Section A*, 940:371–379, Oct 2019.

[45] R. Neilson et al. Characterization of large area APDs for the EXO-200 detector. *Nuclear Instruments and Methods in Physics Research Section A*, 608(1):68–75, Sep 2009.

[46] Keiko Fujii et al. High-accuracy Measurement of the Emission Spectrum of Liquid Xenon in the Vacuum Ultraviolet Region. *Nuclear Instruments and Methods in Physics Research Section A*, 795:293 – 297, 2015.

[47] I. Ostrovskiy et al. Characterization of Silicon Photomultipliers for nEXO. *IEEE Transactions on Nuclear Science*, 62(4):1825–1836, Aug 2015.

[48] J. B. Albert et al. Sensitivity and Discovery Potential of the Proposed nEXO Experiment to Neutrinoless Double-β Decay. *Physical Review C*, 97:065503, Jun 2018.

[49] Nuria López Vaquero, Tomás R. Rodríguez, and J. Luis Egido. Shape and Pairing Fluctuation Effects on Neutrinoless Double Beta Decay Nuclear Matrix Elements. *Physical Review Letters*, 111(14), Sep 2013.

[50] M. T. Mustonen and J. Engel. Large-scale Calculations of the Double-β Decay of ^{76}Ge, ^{130}Te, ^{136}Xe, and ^{150}Nd in the Deformed Self-consistent Skyrme Quasiparticle Random-phase Approximation. *Physical Review C*, 87(6), Jun 2013.

[51] C. Chambers et al. Imaging Individual Barium Atoms in Solid Xenon for Barium Tagging in nEXO. *Nature*, 569(7755):203–207, 2019.

[52] B. Mong et al. Spectroscopy of Ba and Ba^{+} Deposits in Solid Xenon for Barium Tagging in nEXO. *Physical Review A*, 91(2), Feb 2015.

[53] G. Signorelli and S. Dussoni. Possible Usage of Cherenkov Photons to Reduce the Background in a ^{136}Xe Neutrino-less Double-beta Decay Experiment. *Nuclear Instruments and Methods in Physics Research Section A*, 824:658 – 660, 2016. Frontier Detectors for Frontier Physics: Proceedings of the 13th Pisa Meeting on Advanced Detectors.

[54] I. Giomataris. A Background Free Double Beta Decay Experiment. *Journal of Physics: Conference Series*, 309:012010, Aug 2011.

[55] Heidi Becker and A.H. Johnston. Dark Current Degradation of Near Infrared Avalanche Photodiodes from Proton Irradiation. *Nuclear Science, IEEE Transactions on*, 51:3572 – 3578, 01 2005.

[56] W. R. Leo. Techniques for Nuclear and Particle Physics Experiments: A How to Approach. *Berlin, Germany: Springer (1987) 368 p*, 1987.

[57] Hamamatsu Photonics. What is an SiPM and how Does it Work? [Online; accessed: 10. Nov. 2019], https://hub.hamamatsu.com/jp/en/technical-note/how-sipm-works/index.html.

[58] A. Vacheret, G.J. Barker, M. Dziewiecki, P. Guzowski, M.D. Haigh, B. Hartfiel, A. Izmaylov, W. Johnston, M. Khabibullin, A. Khotjantsev, and et al. Characterization and Simulation of the Response of Multi-Pixel Photon Counters to Low Light Levels. *Nuclear Instruments and Methods in Physics Research Section A*, 656(1):69–83, Nov 2011.

[59] R. Mirzoyan, R. Kosyra, and H. G. Moser. Light Emission in Si Avalanches. *Nuclear Instruments and Methods in Physics Research A*, 610(1):98–100, October 2009.

[60] Chen Xu. *Study of the Silicon Photomultipliers and Their Applications in Positron Emission Tomography*. PhD thesis, U. Hamburg, Dept. Phys., 2014.

[61] Patrick Eckert, Hans-Christian Schultz-Coulon, Wei Shen, Rainer Stamen, and Alexander Tadday. Characterisation Studies of Silicon Photomultipliers. *Nuclear Instruments and Methods in Physics Research Section A*, 620(2-3):217–226, Aug 2010.

[62] Marco Ramilli, Alessia Allevi, Luca Nardo, Maria Bondani, and Massimo Caccia. Silicon Photomultipliers: Characterization and Applications. *Photodetector (Sanka Gateva Edt., InTech, Rijeka, Croatia)*, pages 77–100, 2012.

[63] V. Chaumat. SiPM PDE Measurement with Continuous and Pulsed Light. In *International Workshop on New Photon-detectors*, page 058, May 2013.

[64] A. Jamil et al. VUV-Sensitive Silicon Photomultipliers for Xenon Scintillation Light Detection in nEXO. *IEEE Transactions on Nuclear Science*, 65(11):2823–2833, Nov 2018.

[65] G. Gallina et al. Characterization of SiPM Avalanche Triggering Probabilities. *IEEE Transactions on Electron Devices*, 66(10):4228–4234, Oct 2019.

[66] E. Aprile, A. Curioni, K.L. Giboni, M. Kobayashi, U.G. Oberlack, and S. Zhang. Compton Imaging of MeV Gamma-rays with the Liquid Xenon Gamma-Ray Imaging Telescope (LXeGRIT). *Nuclear Instruments and Methods in Physics Research Section A*, 593(3):414–425, Aug 2008.

[67] E. Aprile et al. The XENON100 Dark Matter Experiment. *Astroparticle Physics*, 35(9):573–590, Apr 2012.

[68] A. M. Baldini, E. Baracchini, C. Bemporad, F. Berg, M. Biasotti, G. Boca, P. W. Cattaneo, G. Cavoto, F. Cei, M. Chiappini, and et al. The Design of the MEG II Experiment. *The European Physical Journal C*, 78(5), May 2018.

[69] W.M. Haynes. *CRC Handbook of Chemistry and Physics, 93rd Edition*. 100 Key Points. Taylor & Francis, 2012.

[70] Vitaly Chepel and Henrique Araújo. Liquid Noble Gas Detectors for low Energy Particle Physics. *Journal of Instrumentation*, 8(04):R04001, 2013.

[71] Theodore Lyman. Victor Schumann. *The Astrophysical Journal*, 39:1, 1914.

[72] K. Watanabe, Edward C. Y. Inn, and Murray Zelikoff. Absorption Coefficients of Oxygen in the Vacuum Ultraviolet. *The Journal of Chemical Physics*, 21(6):1026–1030, 1953.

[73] E. Aprile and T. Doke. Liquid Xenon Detectors for Particle Physics and Astrophysics. *Reviews of Modern Physics*, 82(3):2053–2097, Jul 2010.

[74] RL Platzman. Total Ionization in Gases by High-energy Particles: An Appraisal of Our Understanding. *The International Journal of Applied Radiation and Isotopes*, 10(2-3):116–127, 1961.

[75] Tadayoshi Doke, Akira Hitachi, Jun Kikuchi, Kimiaki Masuda, Hiroyuki Okada, and Eido Shibamura. Absolute Scintillation Yields in Liquid Argon and Xenon for Various Particles. *Japanese Journal of Applied Physics*, 41(3R):1538, 2002.

[76] T. Takahashi et al. Average Energy Expended Per Ion Pair in Liquid Xenon. *Physical Review A*, 12:1771–1775, Nov 1975.

[77] Brian Lenardo, Kareem Kazkaz, Aaron Manalaysay, Jeremy Mock, Matthew Szydagis, and Mani Tripathi. A Global Analysis of Light and Charge Yields in Liquid Xenon. *IEEE Transactions on Nuclear Science*, 62(6):3387–3396, Dec 2015.

[78] Chammaa O. and Morison C. Development of an Electroluminescent Light Source for the nEXO Collaboration. *McGill Undergraduate Reports*, May 2018.

[79] Kharusi S. and Nguyen T. Design and Development of a Xenon Gas Electroluminescent UV Light Source for nEXO. *McGill Undergraduate Reports*, Sep 2016.

[80] Belley A. Development of an Electroluminescent Light Source to Characterize SiPMs for the nEXO Collaboration. *McGill Undergraduate Reports*, Aug 2018.

[81] Nasedkin N. E. Development of an Electroluminescent Light Source for the nEXO Collaboration. *McGill Undergraduate Reports*, Jan 2017.

[82] H. Lange, R. Foest, J. Schafer, and K. Weltmann. Vacuum UV Radiation of a Plasma Jet Operated With Rare Gases at Atmospheric Pressure. *IEEE Transactions on Plasma Science*, 37(6):859–865, June 2009.

[83] T. Takahashi et al. Emission Spectra from Ar-Xe, Ar-Kr, Ar-N_2, Ar-CH_4, Ar-CO_2 and Xe-N_2 Gas Scintillation Proportional Counters. *Nuclear Instruments and Methods in Physics Research*, 205(3):591 – 596, 1983.

[84] E.D.C. Freitas, C.M.B. Monteiro, M. Ball, J.J. Gómez-Cadenas, J.A.M. Lopes, T. Lux, F. Sánchez, and J.M.F. dos Santos. Secondary Scintillation Yield in High-pressure

Xenon Gas for Neutrinoless Double Beta Decay ($0\nu\beta\beta$) Search. *Physics Letters B*, 684(4):205 – 210, 2010.

[85] Thorlabs - M265L3 265 nm, 10 mW (Min) Mounted LED, 350 mA. [Online; accessed 21. Jan. 2020], https://www.thorlabs.com/thorproduct.cfm?partnumber=M265L3.

[86] Compact 5W Xenon Flash Lamp Module L9455. [Online; accessed 26. Mar. 2020], https://www.hamamatsu.com/us/en/product/type/L9455/index.html.

[87] R. G. Wilson. Vacuum Thermionic Work Functions of Polycrystalline Be, Ti, Cr, Fe, Ni, Cu, Pt, and Type 304 Stainless Steel. *Journal of Applied Physics*, 37(6):2261–2267, May 1966.

[88] 10BPF10-265 265 nm UV Broadband filter. [Online; accessed 21. Mar. 2020], https://www.newport.com/p/10BPF10-265.

[89] Rohde & Schwarz GmbH & Co KG. R&S®NGE100 Power Supply User Manual. [Online; accessed 22. Mar. 2020], https://www.rohde-schwarz.com/ca/manual/r-s-nge100-power-supply-user-manual-manuals-gb-sg_230144-405444.html.

[90] CR-Z Line of CSP Instruments – Cremat Inc. [Online; accessed 15. Jan. 2020], https://www.cremat.com/home/cr-z-line-of-csp-instruments.

[91] PG Wilkinson. High-Resolution Absorption Spectra of Nitrogen in the Vacuum Ultraviolet. *The Astrophysical Journal*, 126:1, 1957.

[92] E. Hogenbirk, J. Aalbers, P.A. Breur, M.P. Decowski, K. van Teutem, and A.P. Colijn. Precision Measurements of the Scintillation Pulse Shape for Low-Energy Recoils in Liquid Xenon. *Journal of Instrumentation*, 13(05):P05016–P05016, May 2018.

[93] CF 2.75″ Spherical Cube Vacuum Chamber. [Online; accessed 26. Nov. 2019], https://www.kimballphysics.com/mcf275-sphcube-c6.

[94] Newport Optical Materials Properties. [Online; accessed 10. Nov. 2019], https://www.newport.com/n/optical-materials.

[95] K. Woodruff et al. Radio Frequency and DC High Voltage Breakdown of High Pressure Helium, Argon, and Xenon. *arXiv:1909.05860*, 2019.

[96] L. Rogers et al. High Voltage Insulation and Gas Absorption of Polymers in High Pressure Argon and Xenon Gases. *Journal of Instrumentation*, 13(10):P10002–P10002, Oct 2018.

[97] MC1 - SAES Pure Gas - PDF Catalogs | Technical Documentation | Brochure, Mar 2020. [Online; accessed 22. Mar. 2020], https://pdf.directindustry.com/pdf/saes-pure-gas/mc1/175735-657107.html.

[98] Omega Engineering PX309-015A5V Pressure Transducer. [Online; accessed 28. Mar. 2020], https://www.omega.ca/en/sensors-and-sensing-equipment/pressure-and-strain/pressure-transducers/px309/p/PX309-015A5V.

[99] MKS722B14TCD2FA Baratron Pressure Transducer. [Online; accessed 28. Mar. 2020], https://www.mksinst.com/p/722B14TCD2FA.

[100] What is a Pressure Transducer - Omega Engineering. [Online; accessed 28. Mar. 2020], https://www.omega.co.uk/prodinfo/pressure-transducers.html.

[101] J. Sankey. Spinmob - Python Data Acquisition and Analysis Package. [Online; accessed 25. Mar. 2020], https://github.com/Spinmob/spinmob/wiki.

[102] Charles A. Bishop. 7 - Mass Spectrometers, Helium Leak Detectors, and Residual Gas Analyzers. *Vacuum Deposition onto Webs, Films and Foils (Second Edition)*, pages 125–131, Jan 2011.

[103] Stanford Research Systems RGA Software. [Online; accessed 8. Jan. 2020], https://www.thinksrs.com/downloads/soft.html.

[104] How to Use a Turbo Pump | Montana Instruments. [Online; accessed 9. Jan. 2020], https://www.montanainstruments.com/help/How-to-Use-a-Turbo-Pump.

[105] Amplicon Liveline Ltd. Keysight 33500B series | Signal generators, Apr 2020. [Online; accessed 27. Apr. 2020], https://www.amplicon.com/products/keysight-33500b.

[106] ENI 325LA RF Power Amplifier, Apr 2020. [Online; accessed 27. Apr. 2020], https://www.bellnw.com/manufacturer/ENI/325LA.htm.

[107] Hamamatsu Photomultiplier Tube R6834. [Online; accessed 27. Mar. 2020], https://www.hamamatsu.com/us/en/product/type/R6834/index.html.

[108] DT5730 Digitizer - CAEN - Tools for Discovery, Mar 2020. [Online; accessed 29. Mar. 2020], https://www.caen.it/products/dt5730.

[109] ROOT a Data analysis Framework, Jan 2020. [Online; accessed 22. Jan. 2020], https://root.cern.ch.

[110] Uproot. ROOT I/O in Pure Python and Numpy. [Online; accessed 22. Jan. 2020], https://github.com/scikit-hep/uproot.

[111] E. Aprile, K. L. Giboni, P. Majewski, Kaixuan Ni, and M. Yamashita. Proportional Light in a Dual-phase Xenon Chamber. *IEEE Transactions on Nuclear Science*, 51(5):1986–1990, 2004.

[112] A. I. Bolozdynya. Two-phase Emission Detectors and Their Applications. *Nuclear Instruments and Methods in Physics Research Section A*, 422(1-3):314–320, 1999.

[113] Eli. Grushka. Characterization of Exponentially Modified Gaussian Peaks in Chromatography. *Analytical Chemistry*, 44(11):1733–1738, 1972. PMID: 22324584.

[114] Sören Jetter, Dan Dwyer, Jiang Wen-Qi, Liu Da-Wei, Wang Yi-Fang, Zhimin Wang, and Wen Liang-Jian. PMT Waveform Modeling at the Daya Bay Experiment. *Chinese Physics C - CHIN PHYS C*, 36:733–741, 08 2012.

[115] Jun Cao and Kam-Biu Luk. An Overview of the Daya Bay Reactor Neutrino Experiment. *Nuclear Physics B*, 908:62–73, Jul 2016.

[116] E. L. Patrick, M. L. Andrews, and A. Garscadden. Electron Drift Velocities in Xenon and Xenon-Nitrogen Gas Mixtures. *Applied Physics Letters*, 59(25):3239–3240, 1991.

[117] J. C. Bowe. Drift Velocity of Electrons in Nitrogen, Helium, Neon, Argon, Krypton, and Xenon. *Physical Review*, 117:1411–1415, Mar 1960.

[118] 172FNB - 172 nm Narrowband VUV Filter. [Online; accessed 26. Feb. 2020], https://www.esourceoptics.com/172fnblink.html.